FATIGUE BEHAVIOUR OF HIC DAMAGED LINE PIPE STEEL

BY

RAKAN ABDULLAH AL-SHAMMARY

A Thesis Presented to the

DEANSHIP OF GRADUATE STUDIES

KING FAHD UNIVERSITY OF PETROLEUM & MINERALS

DHAHRAN, SAUDI ARABIA

In Partial Fulfillment of the
Requirements for the Degree of

MASTER OF SCIENCE

In

MECHANICAL ENGINEERING

MAY 2005

KING FAHD UNIVERSITY OF PETROLEUM & MINERALS

DHAHRAN 31261, SAUDI ARABIA

DEANSHIP OF GRADUATE STUDIES

This thesis, written by Rakan A. Al-Shammary under the direction of his thesis advisor and approved by his thesis committee, has been presented to and accepted by the Dean of Graduate Studies, in partial fulfillment of the requirements for the degree of **MASTER OF SCIENCE IN MECHANICAL ENGINEERING**.

Thesis Committee

Dr. Zafarullah Khan (Chairman)

Dr. Zuhair M. Gasem, (Member)

Dr. Nesar Merah (Member)

Dr. Amro M. Al-Qutub,
Chairman of M.E. Department

Dr. Salam A. Zummo,
Dean of Graduate Studies

16/6/09
Date

Dedicated

to

My Parents, Brothers, Sisters, Wife & our beloved Children

whose care and prayers were candles to illuminate the way

ACKNOWLEDGEMENTS

All praise and glory be to Allah Almighty the Lord of the great throne. Thanks to Allah for providing me with the strength and patience needed to complete this work, and for making it a success. Peace and blessings of Allah be upon Prophet Mohammed and his family.

Acknowledgements are due to King Fahd University of Petroleum and Minerals for the support in carrying out this research. I acknowledge and appreciate the support of my thesis advisor, Dr. Zafarullah Khan , throughout my research. Acknowledgements are also due to my thesis committee members, Dr. Nesar Merah and Dr. Zuhair Gasem, for their constructive guidance and support.

Special appreciation is due to my family for their support throughout the graduate program.

Acknowledgements are also due to Saudi Aramco for providing me with the support and facilities needed to perform the experimental work for this research. I appreciate the support provided by Ali Al-Kawai, Abbas Al-Turaifi, Abdul-Hameed Al-Jarudi and Sami Al-Sabhan. The help of Ali Al-

Kawai in performing the microscopic examination and SEM work was valuable.

The technical support and help provided by Engr. Mr. Zainulabdeen in conducting experimental work in AMSL is acknowledged. The constant support provided by him in preparing the experimental set-ups for this study is highly appreciated.

Acknowledgement is due to National Pipe Company (NPC) for providing the pipeline plates needed to prepare the testing samples for this research.

TABLE OF CONTENTS

LIST OF TABLES

LIST OF FIGURES

THESIS ABSTRACT

Name: Rakan A. Al-Shammary

Title: FATIGUE BEHAVIOUR OF HIC DAMAGED LINE PIPE STEEL

Major Field: MECHANICAL ENGINEERING

Date of Degree: May 2005

The fatigue behavior of hydrogen damaged pipeline steels is essential to provide useful and necessary background information for performing any Fitness-For-Service study on pipelines in the oil industry. Corrosion of steel in wet sour environment produces atomic hydrogen which is absorbed by the steel. Hydrogen atoms accumulate at non-metallic inclusions and other metallic defects such as grain boundaries. At inclusions hydrogen atoms combine to form molecular hydrogen inside the steel. As the concentration of hydrogen increases, the pressure builds up to produce microscopic blisters. Hydrogen-induced cracking (HIC) occurs when short blisters at varying depths within the steel link together to form a series of steps which may reach the surface and cause the metal to fail.

The present study investigates the influence of hydrogen damage on the fatigue behavior of line pipe steel. The specimens used for the experimental work are designed in compliance with ASTM-E-466-96 "Conducting Force Controlled Constant Amplitude Axial Fatigue Tests of Metallic Materials". A standard test method was used to simulate the service environment of hydrogen absorption from aqueous sulfide corrosion. The hydrogen charged samples were then fatigue tested. Metallography and fractography examinations of failed samples were performed for fracture surface analyses to determine the relationship of the fracture mode to the microstructure, and evaluate the materials' response to mechanical and chemical environments. Samples prepared transverse to the rolling direction of the steel and exposed to HIC were found to have a better fatigue life than HIC exposed samples that were prepared along the rolling direction of the steel.

MASTER OF SCIENCE DEGREE

King Fahd University of Petroleum and Minerals, Dhahran
May 2005

ملخص الرسالة

الإسم: راكان عبدالله الشمري

عنوان الرساله: سلوك الإجهاد لفولاذ الأنابيب المتضرر من التصدعات المستحثه بالهيدروجين

التخصص: الهندسه الميكانيكيه

تاريخ التخرج: مايو 2005

إن سلوك الإجهاد لفولاذ الأنابيب المتضرر بالهيدروجين عامل أساسي لتقديم معلومات خلفيه لإنجاز دراسة ملائمة الخدمة على الأنابيب في مجال صناعة البترول. إن صدى الحديد الصلب في بيئة حمضيه مبلله بالماء ينتج ذرات الهيدروجين التي يتم امتصاصها بالفولاذ. تتجمع ذرات الهيدروجين في الشوائب الغير معدنية وفي العيوب المعدنية الأخرى كحدود البلورات المعدنية. في الشوائب تتحد ذرات الهيدروجين لتكون جزيئات الهيدروجين. كلما أزداد تركيز الهيدروجين تزايد الضغط لينتج تفقعات دقيقه في الفولاذ. يحدث التصدع المستحث بالهيدروجين عندما تتصل التفقعات القصبره مع بعضها في أعماق مختلفة في الفولاذ لتكون تدرجات متتالية التي فد تصل إلى السطح وتسبب فشل المعدن.

الدراسة الحالية تبحث تأثير ضرر الهيدروجين على سلوك الإجهاد في فولاذ الأنابيب. العينات المستخدمة في أعمال التجارب مصممه لمواصفات "تطبيق تجارب إجهاد محورية بقوة تحكم ومدى ثابت". تم استخدام طريقة تجارب قياسية لتحاكي بيئة الخدمة التي يتم بها امتصاص الهيدروجين من صدى الكبريتيد المائي. يتم بعد ذلك تجربة اختبار إجهادي للعينات المحشوة بالهيدروجين. ثم بعد ذلك إجراء فحوصات المعدن مجهريا وفحص سطح التصدع للعينات الفاشلة لتحديد العلاقة بين التصدع والبنية ألمجهريه للمعدن، ولتقييم استجابة المعدن للبيئات الميكانيكية والكيميائية.

درجة الماجستير في العلوم
جامعة الملك فهد للبترول والمعادن
الظهران، المملكة العربية السعودية

Chapter 1

1. INTRODUCTION

1.1 Hydrogen-Induced Cracking in Line Pipe Steel

1.1.1 Hydrogen-Induced Cracking (HIC)

In oxygen-free environments such as wet sour gas or sour crude oil, hydrogen is formed at corroding metal surfaces [1]. Natural gas from the oil wells contains H_2S and CO_2, but their concentrations vary widely from field to field. A gas stream that contains H_2S and water, as a separate liquid phase, is considered to be a wet sour stream. Studies have shown that H_2S has a poisoning effect on the hydrogen evolution reaction. With the presence of H_2S, the concentration of hydrogen diffusing into steels is increased sharply [2]. H_2S prevents recombination of hydrogen atoms at the steel surface, which enhances permeation of hydrogen into steel. Industry guidelines show that HIC may occur if the hydrogen sulfide concentration exceeds 50 ppm in the water phase. This level of H_2S concentration can provide enough hydrogen charging into susceptible steel to cause HIC.

In wet sour service, the occurrence of corrosion will generate hydrogen at the surface of the steel. As atomic hydrogen enters the material by cathodic charging, a large hydrogen supersaturation can be produced. Permanent microstructural damage occurs when this non-equilibrium dissolved hydrogen recombines to form molecular hydrogen and precipitates as hydrogen gas at internal defects such as pre-existent voids, inclusions and second-phase particle-matrix interfaces. Hydrogen transfer to the defects' location can occur by both diffusion and dislocation transport. When the concentration of hydrogen in metal reaches a critical level, cracking can occur.

The binding energy of atomic hydrogen to a defect is high enough to cause the arrival rate of hydrogen at a defect to be greater than its leaving rate. Thus, the concentration rate of atomic hydrogen at a defect increases, which results in the formation of molecular hydrogen. The pressure build-up due to gaseous hydrogen promotes the growth of pre-existent or newly formed microvoids or microcracks.

The main cracks involved in the HIC damage and blistering were observed to nucleate preferentially at the inter-phase boundaries between the manganese sulfide inclusions and the ferrite matrix. These cracks are normally parallel to the surface and do not break the free surface for relaxation of the stress exerted

by the gaseous hydrogen. Instead, the release of stress, caused by the precipitated molecular hydrogen in gaseous state, occurs by a mechanism involving the formation of stepwise secondary cracks. Stepwise cracks nucleate at micro-structural discontinuities such as grain boundaries, pearlite colony boundaries and non-metallic inclusion-matrix inter-phase boundaries. [3]

1.1.2 HIC in Oil Pipeline Steels

HIC is a common problem in line pipe steels used for sour oil or gas transportation. Pipelines are also used for mining sour wells, and they are sometimes required as injection line pipes intended for effective exploitation of wells. The corrosive attack by a wet H_2S environment produces atomic hydrogen, which enters steel under stress and causes various detrimental effects.

Previous studies reported that environments containing hydrogen sulfide cause embrittlement cracking in hard steels, while they cause blistering in soft steels [4]. Carbon steels of yield strength ranging from 47.3 ksi to 64.9 ksi fail at comparatively low stress levels. It was reported that failure of soft steels is of blistering nature, while, heat-treated hard steels exhibit fractures typical of hydrogen-induced intergranular cracking.

Several factors influence steel's resistance to hydrogen-induced internal blistering in wet environments containing hydrogen sulfide. These factors include microalloying which influences the corrosion of steel and hydrogen evolution, non-metallic inclusions as blister nuclei, segregation of phosphorus to accelerate blister crack extension, metallographic structure and second phases.

Insoluble nitrides in steel act as a trap site for atomic hydrogen which reduces the diffusible hydrogen in the steel. Thus, insoluble nitrides prevent the concentration of atomic hydrogen around elongated inclusions, resulting in the prevention of HIC. [4]

1.2 Fatigue in Line Pipe Steel

1.2.1 Fatigue Failures

Mechanical fatigue occurs as a result of cyclic stressing of components in service. The S-N curve illustrates the number of cycles to failure "N" at a given stress "S". Steel exhibits an endurance limit which is the maximum stress below which an infinite number of cycles can be withstood without failure. At higher stresses, fatigue failure can be expected after a given number of cycles.

Fatigue cracks normally initiate at small defects at or slightly below the surface of the component. Defects act as stress raisers that would intensify the load. Poor welds, corrosion pits and sharply machined corners concentrate stresses and work as initiation sites. Propagation of a fatigue crack occurs at an increasing rate as cycling continues.

Fatigue fracture surfaces have a brittle appearance on a macroscopic scale. Fatigue cracks propagate transgranularly with little or no deformation. The cracks typically exhibit a flat region where fatigue cracking initiates and propagates, and a final fracture region where failure occurs by overload when the remaining area of the part is reduced to the point where it can no longer support the applied load.

Beach marks are surface features of fatigue fractures, which radiate out in a clamshell appearance from the crack initiation site. Beach marks are visible to the naked eye or a low-power microscope and they generally mark significant load variations.

The fatigue crack origin can often be located by drawing lines at right angles to the tangents of the beach marks. Except for the case where geometrical

constraints interfere, the lines drawn in this manner will converge near the crack origin. The fracture surface may also contain radial marks that converge back to the origin.

1.2.2 Fatigue in Oil Pipeline Steels

Piping used in the oil industry has experienced fatigue failures due to vibration or surge cycles caused by flow of oil. Examples include drain lines, pump discharge piping, elbows, electric resistance welded (ERW) pipes, etc. It has been noted that cracking initiates due to persistent vibration at stress concentration sites such as the toe of fillet welds, sharp transition elbows and corrosion pits. An ERW pipe may fail by a combination of fatigue and environment due to higher impurity and inclusion levels (micro-segregation) along a seam-like indication. Imperfections may be formed during the original steel manufacture.

Characteristics of the fatigue fracture in pipelines include flat fracture surfaces with no significant metal deformation observed. Chevron marks indicate cleavage and rapid fracture, and they point toward the fracture origin.

1.3 Objectives of Present Study

Fitness-For-Service (FFS) is used in Saudi Aramco to evaluate plant equipment such as pressure vessels and piping in hydrogen service applications. Knowledge of the fracture mechanics and fatigue behavior of hydrogen-damaged steel is essential for performing any Fitness-For-Service study.

Several studies have been performed in the past to investigate hydrogen-induced blister cracking of line-pipe steels in sour environments which included the effects of microstructure, inclusions, hydrogen sulfide concentration, operating parameters, etc. Other studies investigated mechanical properties and fatigue fracture characteristics of pipeline steel.

Piping in the oil industry, used in sour service where H_2S is present, has experienced fatigue failures due to vibration induced by regular operation. The present study examines the characteristics of pipeline steel samples exposed to hydrogen damage and then tested for fatigue. The fatigue testing results from exposed samples are compared to those obtained from unexposed samples. The present study provides a better understanding of the influence of hydrogen damage on the fatigue behavior of pipeline steel.

Chapter 2

2. LITERATURE REVIEW

Miyoshi et al [5] investigated the hydrogen-induced cracking (HIC) of as-rolled steels. HIC susceptibility increased with the elongation of the sulfide inclusions by rolling at a lower temperature. The addition of a small amount of copper significantly reduced the amount of hydrogen absorption.

Biefer [6] investigated the stepwise cracking (SWC) of line-pipe steels in sour environments in correlation with the effects of the environmental, metallurgical and stress variables. Rigsbee [3] examined the hydrogen-induced cracking and stepwise cracking of spheroidized and pearlitic microstructures of low-alloy medium carbon steel in the absence of external stress.

Iyer et al [2] observed the enhanced permeation of hydrogen that occurred in the presence of hydrogen sulfide during cathodic hydrogen charging of steel. The steady-state hydrogen permeation current density was greatly enhanced in the presence of hydrogen sulfide. The hydrogen absorption and adsorption rate constants were obtained as a function of membrane thickness.

Merrick [7] discussed the different types of hydrogen damage mechanisms that can be expected with carbon and ferritic alloy steels in wet hydrogen sulfide. Liou et al [8] examined the effects of niobium, copper, chromium, molybdenum and titanium in high-strength low-alloy steel on hydrogen induced cracking (HIC).

Poepperling and Sussek [9] evaluated the effects of metallurgical and testing variables on the hydrogen-induced corrosion behavior of structural and pipeline steels. The highest hydrogen permeation rates were measured on pipelines steels with high dislocation density.

Merrick and Buller [10] discussed the prevention of cracking in H_2S environments for pressure vessels made of older steel. Stress relief after fabrication reduces SOHIC probability but does not guarantee resistance. Cladding vessels with Type 304 stainless steel will provide resistance.

Sumitomo Metal Industries Ltd. [11] examined sour gas pipes with cracks along the spiral weld bead. Service cracks were found to be caused by hydrogen embrittlement due to hydrogen absorption from the wet hydrogen sulfide environment during corrosion.

Wilhelm and Abyarathna [12] studied the inhibition of hydrogen absorption by steels in refinery environments containing wet hydrogen sulfide, ammonia and cyanide. Hydrogen absorption and corrosion rates were found to be dependent on H_2S and NH_3 concentration, in the pH region where HS^- was the dominant protonic species.

Kimura et al [13] studied the environmental factors that affect the hydrogen permeation in line pipe steel. Factors influencing hydrogen permeation include partial pressure of H_2S and CO_2, temperature, cations and the solution pH. Luppo and Garccia [14] investigated the effect of the microstructure on the trapping and diffusion of hydrogen in a low-carbon steel. The quantity of desorbed hydrogen is at the maximum with martensite, and it decreases with the increasing tempering temperature.

Petrie and Moore [15] discussed the suitability of existing pipelines, originally built for sweet and/or dry service, which are converted into wet sour multiphase service. Timmins [16] described different types of hydrogen blisters and gave some guidelines for detecting such damage mechanisms in sour-gas service.

Flavenot [17] discussed the methodology for fatigue life prediction of mechanical structures. The paper discussed two methods for fatigue life estimation. The first method uses the damage laws for predicting the crack initiation life. The second method is a simulation of the loading history on the loading machine. Important parameters for these methods are the loading history, material behavior and geometry of structure.

Solin and Hayrynen [18] described laboratory tests for simulation of realistic service conditions. The experimental methods account for crack growth tests in air and aqueous environments under constant amplitude and spectrum loading. Structural testing and corrosion fatigue are also discussed.

Ahn et al [19] studied the corrosion fatigue of HSLA steel by using a single pitted specimen. Mazumdar [20] presented a model for high cycle fatigue based on crack initiation. The crack initiation parameters include the material's grain size and Burger's vector, in addition to its propensity to cracking characterized by crack spacing or density.

Lenets [21] studied the behavior of fatigue cracks under compressive cycling in laboratory air, mineral oil and 3.5% NaCl on circumferentially notched cylindrical specimens of aluminum-based alloy and stainless steel. Gramberg

[22] surveyed the causes and mechanisms of hydrogen-induced damage. Internal mechanisms originate in the melt supersaturated with hydrogen such as weld cracking, flake formation and fish eyes. External mechanisms occur in a material exposed to a hydrogen-containing environment, such as hydrogen embrittlement of steel and hydrogen-induced cracking.

Rios and Navarro [23] discussed the microstructural fracture mechanics principles to develop a model of crack growth in long-life fatigue. The microstructural modeling considers the material to be polycrystalline with uniform grain size D, and a crack system divided into three zones: the crack, the plastic zone and the microstructural barrier zone.

Xiao [24] presented the continuum damage mechanics model for high cycle fatigue based on the general thermodynamic framework. Wang [25] investigated the relationship between the fatigue limit and the mechanical strength of metals. The critical stress to initiate and propagate a fatigue crack in the interior of a specimen was shown by the resistance to mini-plastic deformation. Karp [26] developed a mathematical model for fatigue crack propagation under the influence of residual stress. The model predicts the fatigue crack propagation by the interaction of microstructure, mechanism and mechanics.

Gjonaj and Cukalla [27] studied the effect of chemical composition and microstructure on the fatigue strength and fatigue crack growth rates of chromium and nickel alloy steel. They concluded that chromium and nickel do not have an influence at the midrange of growth rate where the Paris equation is applied, but these elements do have an effect on the fatigue limit. Carbon influences both the fatigue limit and the crack propagation. The higher the carbon content, the higher the range of change of m constant; where m = *f* (Tr).

Riemelmoser and Pippan [28] discussed the mechanical behavior of small fatigue cracks for low, medium and high strength material. The von Mises stress contour showed a strong influence of crack size on the plastic zone, especially for plastically weak materials. Soboyejo and Soboyejo [29] demonstrated the applicability of the Paris law to cover the zones of low stress-intensity factor range (ΔK) and high intensity factor range (ΔK) in reliability-based engineering design against fatigue.

Wild et al [30] investigated line-pipe steels exposed to hydrogen sulfide with a scanning electron microscope. Hydrogen blisters initiated at the elongated manganese sulfide inclusions. Columbium carbonitride precipitates and glassy silicate inclusions can also act as initiation sites for cracking. Qualitative results indicated a threshold fugacity, between10^4 and 10^5 atmospheres, below

which no cracking will initiate. Propagation of blisters occurs by hydrogen-assisted fracture of the matrix surrounding the initiating inclusion, while step-wise cracking propagates by hydrogen-assisted fracture between interconnecting planes.

Gao et al [31] showed that short periods of overloading have a noticeable influence on the life of the environmental hydrogen-induced cracking. Experimental work confirmed that the overloading applied during the early or middle stage of the service period increases the life of the hydrogen-induced fracture; but the overloading applied during the late stages of the service period shortens the life of the hydrogen-induced fracture. The influence of overloading on the life of hydrogen-induced fractures is attributed to the balance between the retarding and accelerating factors. The retarding factors for hydrogen-induced fracture include plasticity-induced closure, residual compressive stresses and dislocation shielding; while the accelerating factors include growth and micro-crack formation. When the effect of the retarding factors is greater than the accelerating factors, the hydrogen-induced fracture life increases, but when these factors are reversed the life decreases.

Yoshino [32] examined the hydrogen uptake of steel in an acidic H_2S solution to investigate the influence of microstructure and chemical composition. The

hydrogen uptake is affected significantly by carbide precipitation. Hydrogen entry was enhanced by the secondary precipitation hardening process such as Mo_2C and $(Fe,Cr)_7C_3$ carbides. The amount of hydrogen absorbed is increased with the precipitation of fine carbide particles due to the formation of sites where hydrogen is trapped at the carbide interface. Steels containing chromium showed a greater tendency to hydrogen absorption, which indicated that $(Fe,Cr)_7C_3$ carbide has a larger binding energy with hydrogen than Mo_2C carbide. Cementite absorbed large amounts of hydrogen in an upper bainite structure, but it had only a minimal effect in the tempered martensite structure. Hydrogen absorption increased with up to 17% Cr in steel due to the effect of the $(Fe,Cr)_7C_3$ carbide precipitation.

Tuttle and Kane studied step-wise cracking in pipelines. Although it is not a widespread problem, the occurring failures have generated widespread interest in the susceptibility of line pipe steels to this type of mechanism. Qualitative and quantitative evaluation methods including photographs of cross sections and calculations of crack sensitivity ratio (CSR), Crack Length Ratio (CLR) and Crack Thickness Ratio (CTR) were also described.

Taira et al [34] conducted extensive analyses to explore the effects of metallurgical factors on the resistance of line pipe steels to the damage

mechanism hydrogen-induced cracking (HIC) and sulfide-stress cracking (SSC). Investigation showed that inclusion shape control and extensive desulfurization are essential in eliminating potential HIC formation sites.

Although in certain steels the formation of a passive film or some type of corrosion product controls corrosion and prevents HIC, these measures are unreliable because they do not apply in severe environments such as the NACE solution. Hard band structures containing bainite or martensite are susceptible to hydrogen embrittlement and are also likely sites for HIC. Therefore restricting the hardness of the segregation zone to below 300 HV is essential for preventing HIC propagation. The low temperature transformation of microstructure depends on the hardenability of the steel, while the hardness of the low-temperature transformation microstructure depends on the carbon content. Therefore reducing the carbon content to below 0.02 % and the manganese content to below 1.0 % improves the HIC resistance significantly. Homogenization of the microstructure and complete elimination of inclusions improved stress-corrosion cracking (SCC) resistance in line pipe steels.

Jack [35] discussed the use of HIC resistant steels in sour refinery environments. Industry experience revealed that the use of post-weld heat treatment (PWHT) with HIC resistant steel is not effective in reducing the wet H_2S cracking risk.

Field data showed no benefit of PWHT in reducing minor cracking and only a slight benefit of PWHT in reducing significant cracking which exceeds the vessel's corrosion allowance. Therefore PWHT is not a very effective solution for wet H_2S cracking. On the other hand, PWHT proved to be very effective for preventing other environmental cracking mechanisms, such as amine carbonate or caustic SCC. Chevron has used in six US refineries more than 50 pressure vessels made of HIC resistant steel. Dramatic instances of cracking in wet H_2S environments have been reported. These incidents challenged the validity of using special HIC-resistant steels to mitigate wet H_2S cracking. [35]

Dauskardt [36] studied the effects of pre-existing grain boundary microvoid distribution on fracture toughness and fatigue crack growth in low-alloy steel. Prior exposure of the steel to gaseous hydrogen atmospheres at high temperatures and pressures causes microvoid damage. This mechanism occurs when the carbon within the steel reacts with ingressed hydrogen to nucleate methane bubbles along prior austenite grain boundaries. The intrinsic fracture resistance of the microstructure is lowered by microvoids, which lowers the resulting tortuous crack paths and extrinsically retards the crack growth at low stress intensities by lowering the local crack tip driving-force "crack tip shielding". Effects of shielding are minimized at high stress intensities. The presence of small microvoid clusters promotes coalescence through the easier

onset of plastic strain localization, which degrades the intrinsic toughness due to changes in ductility by means of a stress-modified critical strain model. Therefore the crack growth toughness and crack initiation are severely degraded. Fatigue behavior was dominated by extrinsic shielding mechanisms. Therefore sub-critical crack growth by fatigue is relatively unaffected. Fatigue is modeled in terms of two-dimensional models of crack deflection and roughness-induced crack closure.

Vera et al [37] investigated the sulfide-stress cracking susceptibility of high-strength steels used for oil grade tubulars (OCTG) with the hydrogen concentration inside the metal. Experimental results show that sulfide-stress cracking susceptibility is related to steady-state subsurface hydrogen concentration at different temperatures and pH values. A threshold subsurface hydrogen concentration can be identified to describe the sulfide-stress cracking susceptibility of OCTG grades of carbon steel. The diffusion coefficient of hydrogen increases with high temperatures, which reduces the hydrogen concentration inside the steel for the same hydrogen flux, which reduces the SSC susceptibility.

Heldt and Kaesche [38] studied the effect of absorbed hydrogen in a dry environment on the microstructure in the vicinity of near-threshold fatigue

cracks in low-alloy steel. The environmental influences in the near-threshold region on the crack propagation rates are of more significance than in the Paris regime. Experimental results showed a significant acceleration of crack propagation in the near-threshold regime in dry hydrogen compared to testing in an ultra-high vacuum (UHV) environment.

Chapter 3

3. EXPERIMENTAL PROCEDURE

3.1 Preparation of Test Samples

3.1.1 Material

The samples used for testing were prepared from three different types of pipeline plates with a thickness of 13 mm. The pipeline material types were API 5L Grade X42 (non-sour resistant), Grade X60 (non-sour resistant) and Grade X-60 (sour resistant). The evaluated chemical composition of the pipeline plates is illustrated in table 3.1. The mechanical properties provided in the vendors mill test certificate for the selected pipeline material grades are illustrated in table 3.2.

Table 3-1: Chemical Composition

Material Type	Fe	C	Si	Mn	S	Cr	Ni	Nb
Grade X42 (non-sour resistant)	bal.*	0.11	.18	1.14	.003	.003	.01	.012
Grade X60 (non-sour resistant)	bal.	.076	.19	1.37	.001	.01	.01	.05
Grade X-60 (sour resistant)	bal.	.06	.28	1.14	.0006	.06	.19	.055

bal = balance

Table 3-2: Mechanical Properties of the samples

Grade	Fatigue Samples	Sample marking	Tensile strength (MPa)	Yield strength (MPa)
X-42 non-sour resistant	L	A	485	375
X-42 non-sour resistant	T	B	485	375
X-60 non-sour resistant	L	C	625	534
X-60 sour resistant	T	D	554	479
X-60 sour resistant	L	E	554	479
X-60 non-sour resistant	T	F	625	534

L: Samples were prepared longitudinal along the rolling direction.

T: Samples were prepared transverse to the rolling direction.

3.1.2 SAMPLE DESIGN

The samples of the study program were designed in compliance with ASTM-E-466-96 "Conducting Force Controlled Constant Amplitude Axial Fatigue Tests of Metallic Materials". This standard is limited to the performance of axial force controlled fatigue tests subject to constant amplitude, andperiodic forcing function in air at room temperature.

The design of the specimen was based on the consideration of the capacity of the equipment, so as to ensure that the failure would occur in the test section.

The specimen gripping method provided the acceptable ratio of test section to grip section.

Standard ASTM-E-466-96 mandates that, for cylindrical samples, the radius of curvature should be more than eight times the minimum diameter of the test section, to minimize the theoretical stress concentration factor, K_t. To ensure test section failure, the grip cross-sectional area should be at least 1.5 times, but if possible preferably four times, the test section area.

The plate thickness, which the specimens of the study were prepared from, was 13 mm. Therefore the grip cross-sectional diameter was limited to 12.5 mm after machining. To obtain an optimal radius of curvature, the minimum diameter of the test section of 6 mm was selected with a test section length of 50 mm. The length of the grip section was 50 mm on each side of the samples.

Figure 3.1 presents a schematic of the cylindrical specimen used in the study. Figure 3.2 is a photograph of a sample ready for fatigue testing.

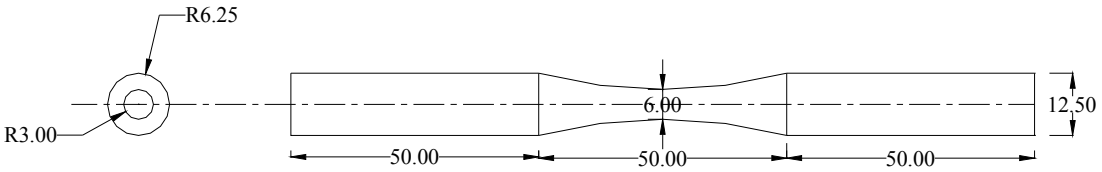

Figure 3.1: Geometry of test sample. All dimensions are in millimeter

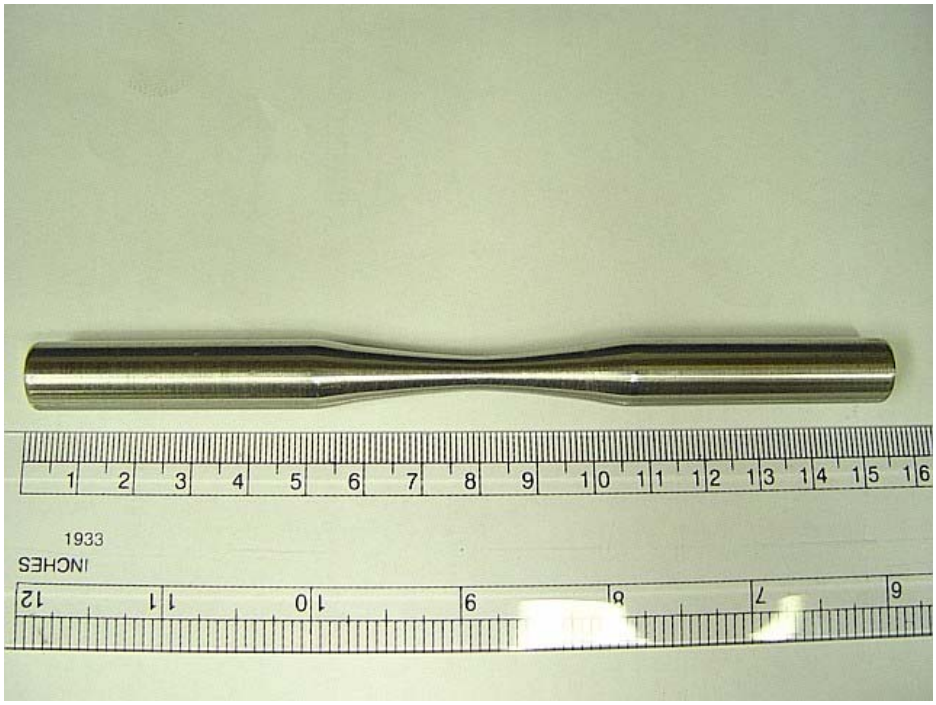

Figure 3.2: Photograph of a fatigue test sample

3.2 HIC Exposure

3.2.1 Exposure Method

The standard test method of NACE TM0284-2003 "Evaluation of Pipeline and Pressure Vessel Steels for Resistance to Hydrogen-Induced Cracking" was used to simulate the service environment of hydrogen absorption from aqueous sulfide corrosion.

NACE TM0284-2003 requires the use of either one of following two test solutions to expose unstressed samples:

1. Solution A:

The solution consists of sodium chloride (NaCl) and acetic acid (CH_3COOH) saturated with H_2S at ambient temperature and pressure. The reagents for this solution are nitrogen gas for purging, H_2S gas, CH_3COOH, NaCl, and distilled or deionized water.

2. Solution B:

The solution is primarily synthetic seawater saturated with H_2S at ambient temperature and pressure. The preparation of synthetic seawater is in compliance with ASTM D-1141 (Standard Practice for the Preparation of Substitute Ocean Water), Stock solutions No. 1 and No. 2 (without heavy metal ions).

Solution A was used for the HIC exposure test of the samples used in this experimental work, because it is characterized by industry as the harshest test type for HIC exposure.

3.2.2 EXPOSURE SET-UP

Figure 3.3 is a schematic illustration of the experimental set-up for HIC exposure tests. The cylindrical test samples were arranged in the desiccators as shown in Figures 3.4 - 3.6. The jar was then sealed and placed into the

container,as in Figure 3.7. The jar was then de-aerated by using nitrogen purging for one hour.

Solution A was prepared by using 5% sodium chloride, 0.5% acetic acid and distilled water at a pH of 2.7. The solution was then transferred into the jar by using nitrogen pressure. The exposure test temperature was adjusted at 25 °C. The exposure was carried out at the atmospheric pressure.

The H_2S gas was then circulated through the solution at a rate of 200 mL/minute for the first 60 minutes. Then the H_2S flow rate was reduced to maintain a positive pressure for the rest of the test. The H_2S concentration in the solution was a minimum of 2,300 ppm according to the iodometric titration measurement. The duration for exposure to a simulated environment of solution A of NACE TM0284-2003 was 96 hours for all the exposed samples as specified by the standard.

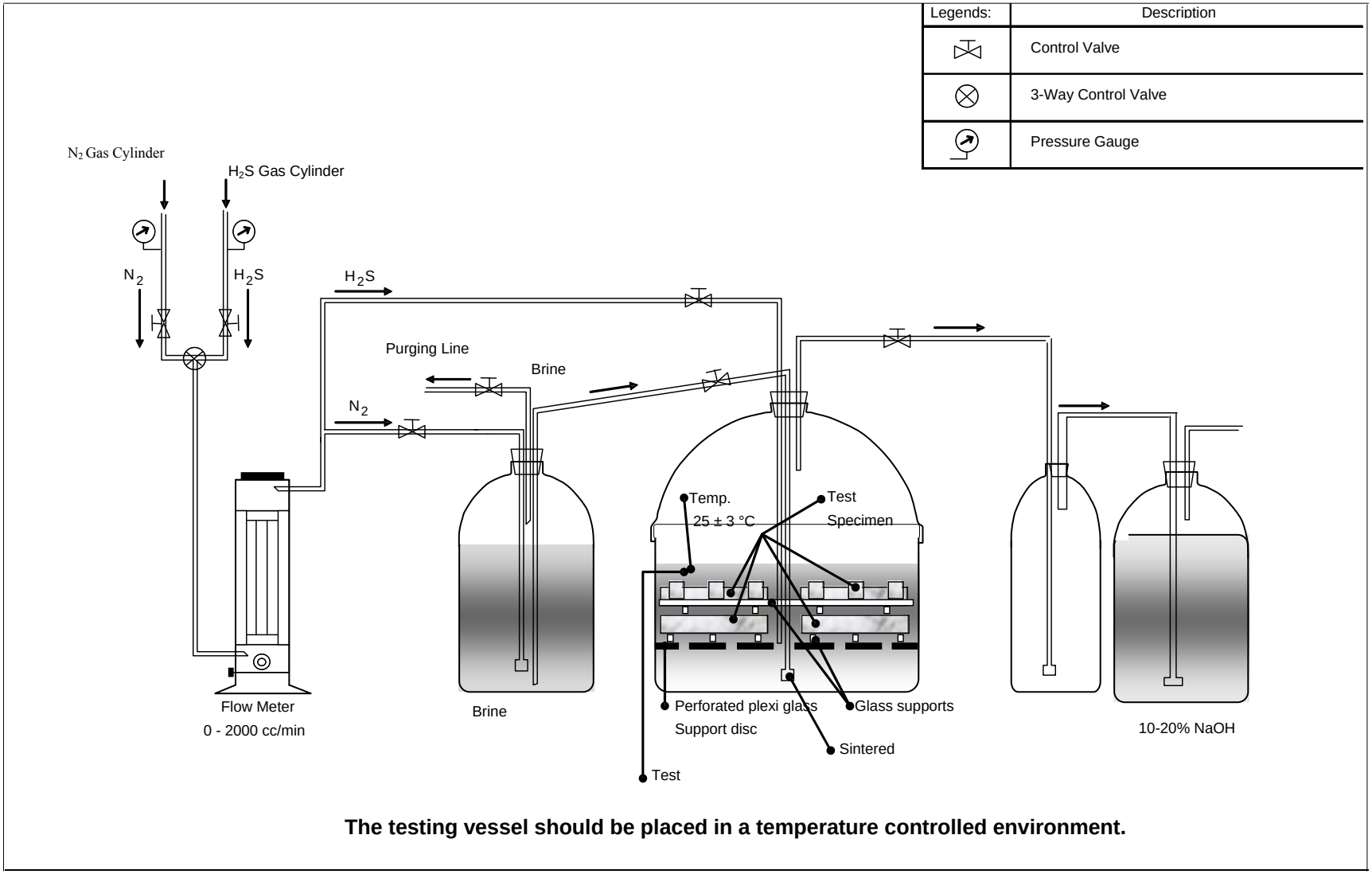

Figure 3.3: Schematic of the experimental set-up for the HIC exposure test.

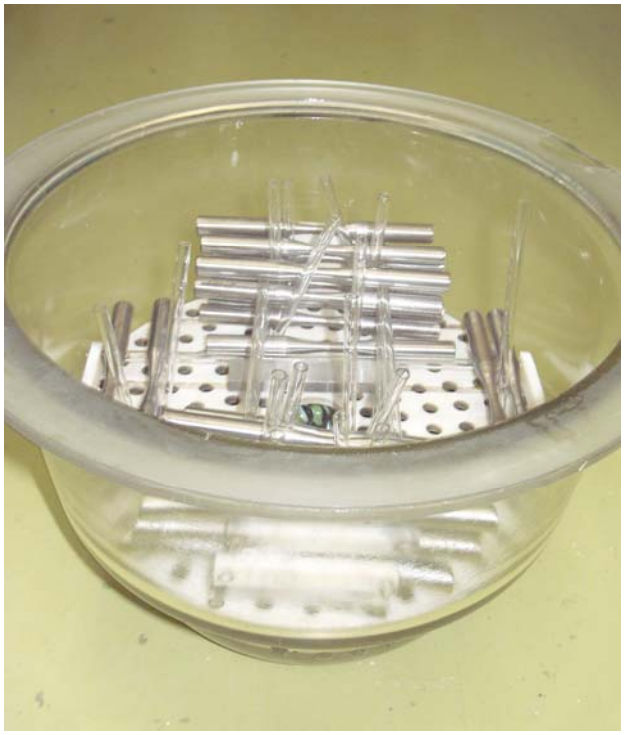

Figure 3.4: Photograph showing the samples arranged in the desiccators, (side view)

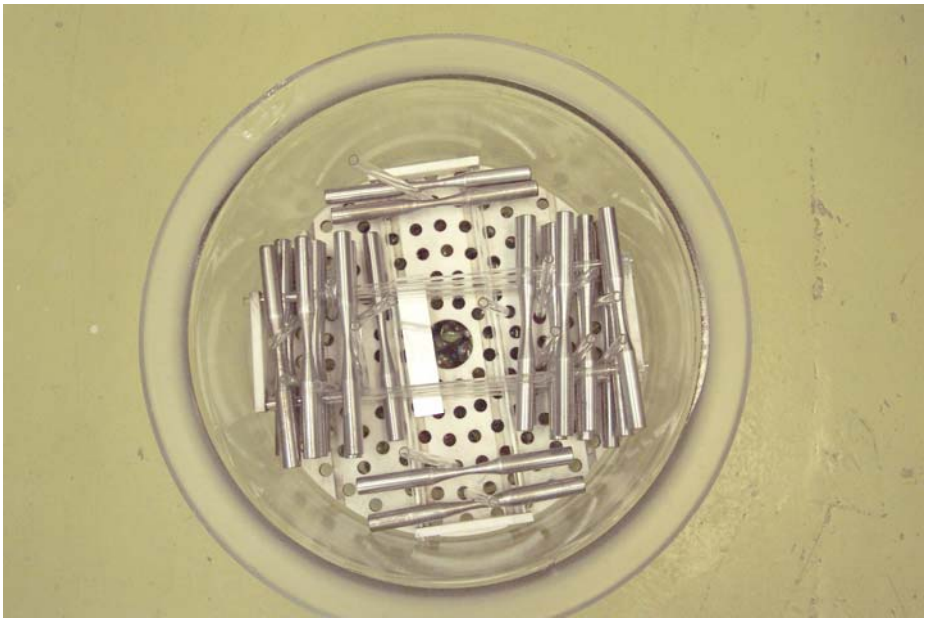

Figure 3.5: Photograph showing the samples arranged in the desiccators, (top view.)

Figure 3.6: Photograph showing the jar after being sealed with inlet and outlet nozzles.

Figure 3.7: Photograph showing the jar placed into the temperature control container for hydrogen exposure

3.3 Fatigue Testing

3.3.1 Test Machine

The Instron 8801 material testing system was used to obtain tensile and fatigue data, as shown in Figures 3.8 and 3.9. The system is a closed loop servo-hydraulic, dynamic, single-axis fatigue testing system. The machine was equipped with a hydraulically actuated self-aligning gripping system. To ensure the vertical alignment of the specimen specially machined metal inserts were used during the tests. Any preloading induced during clamping was adjusted to zero prior to testing by balancing the load cell after clamping.

All tensile tests were carried out by using specialized software called Series IX, and the fatigue tests were carried out by using Wave Maker software, which provided complete machine control, data acquisition, data reduction and analysis capability. Fatigue tests conducted through Wave Maker followed the tasks; initially a ramp to mean load level and then a sinusoidal loading with a frequency of 20 Hz at a stress ratio, R = 0.1, $R = \frac{\sigma_{\min}}{\sigma_{\max}}$. The maximum cyclic stress ranged approximately from 75% to 95% of the tensile strength of the material.

Tensile tests were carried out under position control. The software logged the position and the corresponding load of the test, with a constant position increment until fracture occurred. The elastic modulus was obtained by getting the load and position data throughout the tensile tests. The final stress value just before the fracture was selected as the tensile strength, and the final actuator position gave the $\in_f$.

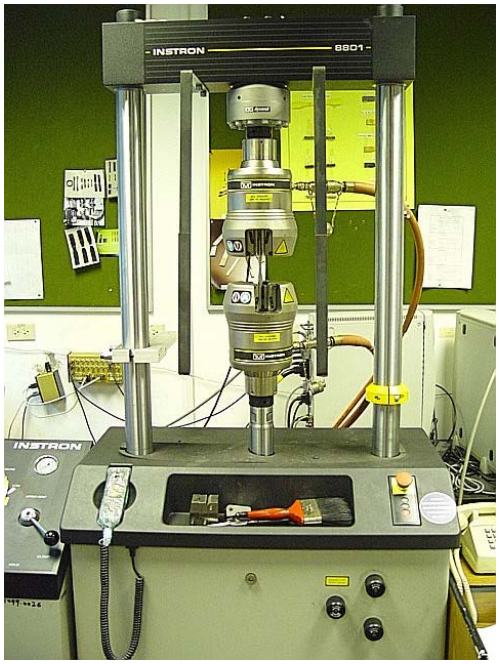

Figure 3.8: Instron fatigue testing machine model 8801.

Figure 3.9:Close-up view of a sample inside the clamps.

3.4 Material Characterization

3.4.1 Microstructural Study

The microstructure is dependent on the composition and processing, and many metals and alloys can exhibit a number of different structures at the same nominal composition. Microsections of the test samples were examined by using light microscopy to study the microstructural features. Such examinations were performed to evaluate the microstructure and detect any laminations, banding and anomalies that may have occurred from inadequate material quality, fabrication or heat treatment deficiencies. The strength and

toughness of a material during fracture can be drastically different according to the microstructure.

The relationship of hydrogen-induced cracks to microstructural anomalies was assessed in comparison with the fatigue life of each type of line pipe steel at different cyclic loading values.

The grain size is an important factor, as a finer grain structure provides higher strength and ductility, while most other strengthening mechanisms result in decreased toughness. Strengthening by finer grain size was achieved in part by the increase in the amount of grain-boundary regions as the grain size is reduced. Grain boundaries are stronger than individual grains.

Also of considerable importance in commercial quality materials, and especially those having a large volume fraction of second phases and/or inclusions, is the banding of compositional segregations and grain fibering in wrought forms. Banding gradients and grain fibering in wrought metals results in nonuniform distribution of inclusions and chemical segregations. In some alloys, chemical segregation can result in banding of microconstituents and greater anisotropy. Examples include bands of pearlite in annealed or hot-rolled steels and ferrite stringers in austenitic stainless steels.

3.4.2 Fractographic Study

Fractography is an essential tool in the study to provide understanding of fracture surfaces in three dimensions. By using the scanning electron microscope (SEM), it also presents descriptive information regarding the micromechanisms of the fracture processes.

Models have been developed to explain the mechanisms of fatigue fracture. They use correlations between fatigue striations, load cycles, striation spacing, and loading conditions. Definite experimental evidence regarding initiation mechanisms of fatigue fracture has also been acquired from electron fractography studies.

Fractography was used in the study to examine the features and important characteristics of the fracture surfaces of specimens to determine the relationship of the fracture mode to the microstructure, and to evaluate the materials' response to mechanical and chemical environments.

Chapter 4

4. TENSILE AND FATIGUE TEST RESULTS

Cylindrical fatigue samples were prepared as per ASTM E-466-96. Simulated HIC exposure was performed for 96 hours as per method NACE TM0284-2003 solution A. The samples were then tensile and fatigue-tested.

Samples that were exposed to the HIC simulated environment were identified with a prime after the letter.. Tensile testing was performed respectively on samples exposed and unexposed to the HIC environment. Tables 4.1 and 4.2 present the tensile data results for samples both exposed and unexposed. Tensile testing curves are illustrated in Figures 4.1-4.12.

Samples exposed and unexposed to the HIC environment were then fatigue-tested. Tables 4.3, 4.5, 4.7, 4.9, 4.11 and 4,13 present the test results organized by samples (A, B, C, D, E and F) in the as-received condition, unexposed to the HIC simulated environment. Tables 4.4, 4.6, 4.8, 4.10, 4.12 and 4.14 provide the fatigue test results for samples (A', B', C', D', E' and F') after being exposed to the HIC simulated environment.

Figure 4.13 illustrates the σ_a -N curves of both (A) samples in the as-received condition and the (A') samples that were exposed to the HIC simulated environment. Samples A and A' were machined longitudinally to the rolling direction of Grade B X-42 non-sour resistant steel. As shown in the graph, the reduction in σ_a between the two σ_a-N curves, at 10^5 number of cycles is 10.1%; while the reduction in the fatigue life at a σ_a of 210 MPa is by almost an order of magnitude of 9. At a low stress values, the reduction in σ_a averaged 5.6%, at 10^6 cycles; while the reduction in the fatigue life was by an order of magnitude of 6 at σ_a of 175 MPa,.

It is observed that as the load value for testing is reduced, the difference between the two σ_a -N curves in the number of cycles to failure is also reduced. The reduction in difference between the two σ_a -N curves with the reduction of stress is attributed to material degradation by the embrittlement of the steel due to the effects of hydrogen charging.

The graphs of the σ_a -N curves for B and B' samples were plotted in Figure 4.14. The B and B' type samples were made transverse to the rolling direction of Grade B X-42 non-sour resistant carbon steel. The reduction in the fatigue

strength at 10^5 cycles averaged 5.9%; while the reduction in the fatigue life at σ_a of 210 MPa was by an order of magnitude of 5. The reduction in fatigue strength at 2.5 X 10^6 cycles averaged 2.7%; while the reduction in fatigue life at σ_a of 175 MPa was by an order of magnitude of 2.

It is observed that the difference between the two σ_a -N curves (unexposed B samples and HIC exposed B' samples) is less than the difference between the two σ_a -N curves of A-A' samples. Samples A and A' were manufactured longitudinal to the rolling direction; while Samples B and B' were manufactured transverse to the rolling direction.

Banding and sulfide stringers are formed longitudinal to the rolling direction. HIC cracks are developed along banding and sulfide stringers. The reduction in difference between the two σ_a -N curves of B-B' samples in comparison to A-A' samples is attributed to the formation of HIC cracks along the rolling direction.

Figure 4.15 presents the σ_a -N curves for C-C' samples (unexposed and exposed to HIC environment). The material type of (C-C') samples is Grade B X-60 non-sour resistant carbon steel made longitudinal to the rolling

direction. The reduction in fatigue strength at 10^5 cycles averaged 2%; while the reduction in the fatigue life at σ_a of 250 MPa was an order of magnitude of 2. The difference between the σ_a -N curves at low stress values is relatively similar to the difference at high stress values.

Figure 4.16 Presents the σ_a -N curves of HIC environment unexposed and exposed (D-D') samples. The material type of D and D' samples is Grade B X-60 sour resistant prepared transverse to the rolling direction. The reduction in fatigue strength at 1.5 X 10^5 cycles averaged 2%; while the reduction in fatigue life at σ_a of 230 MPa was an order of magnitude of 1. At a low stress amplitude value, no significant effect of HIC exposure was noted on the fatigue resistance.

The σ_a -N curves of hydrogen charged and un charged (E-E') samples are presented in Figure 4.17. E and E' Type samples are made of Grade B X-60 sour resistant machined longitudinal to the rolling direction. The two S-N curves of hydrogen charged and un-charged (E-E') samples were relatively similar. This is expected since the material is HIC resistant.

Figure 4.18 illustrates the σ_a -N curves of both hydrogen charged and un-charged (F-F') samples. F and F' samples were machined from Grade B X-60 non-sour resistant steel transverse to the rolling direction. "C" samples were machined longitudinal to the rolling direction of the same steel. The reduction in fatigue strength at 1.5 X 10^5 cycles averaged 2%; while the reduction in fatigue life at σ_a of 250 MPa was an order of magnitude of 1. It is observed that, as the load value for testing is reduced, the difference between the two σ_a -N curves in fatigue resistance becomes insignificant. The change in difference between the two σ_a -N curves with the reduction of stress is attributed to the hydrogen embrittlement of the steel.

The σ_a -N curve for A samples was plotted in comparison to B samples in the unexposed condition, Figure 4.19. The graph showed that "B" samples, that are prepared transverse to the rolling direction of Grade B X-42 non-sour resistant steel, have relatively a similar fatigue life to "A" samples that are prepared from longitudinal sections of the same steel plate.

Figure 4.20 presents the σ_a -N curves of A' and B' specimens after being exposed to HIC. The graph shows that the fatigue life of B' samples is slightly better than A' samples. The slight change in fatigue life is attributed to the

presence of elongated inclusions and sulfide stringers along the rolling direction of the steel, which is related to the sample geometry and acts as trap-site for atomic hydrogen while exposed to hydrogen charging.

The σ_a -N curves of C samples were plotted in comparison with F samples for the unexposed condition. Figure 4.21 shows that F samples have a slightly better fatigue life than C samples. This change of fatigue life is attributed to the change of mechanical properties of the material with direction.

F' samples, exposed to HIC, that are transverse to the rolling direction of Grade B X-60 non-sour resistant steel, were compared to HIC exposed C' samples, that are prepared from longitudinal sections of the same steel plate. The S-N curves are plotted in Figure 4.22. The graph shows that F' samples have a better fatigue life than C' samples. The finding of Figure 4.10 is compatible with the results of Figures 4.19, 4.20 and 4.21.

TENSILE TEST RESULTS

Table 4-1: Tensile data results for samples unexposed to HIC environment

Specimen label	Yield stress (MPa)	Yield Stress Average (MPa)	Maximum Stress (MPa)	Max. Stress Average (MPa)	Tensile strain at Break (%)	Tensile Strain Average (%)	Modulus (MPa)	E, Average (MPa)
A-uncharged	350	350.50	472	476.60	13.2	13.75	16059	16795
	351		481.2		14.3		17531	
B-uncharged	348	357.50	477.5	472.75	13.6	13.60	16188	16131
	367		468		13.6		16073	
C-uncharged	493	491.00	601.26	596.30	13.04	13.24	16539	17857
	489		591.34		13.44		19174	
D-uncharged	486	478.00	565	558.50	13.04	13.57	22097	21954
	470		552		14.1		21811	
E-uncharged	453	441.50	558	550.50	12.9	13.55	17519	18808
	430		543		14.2		20096	
F-uncharged	544	537.00	645	640.50	10.6	10.20	21462	19249
	530		636		9.8		17036	

Table 4-2: Tensile data results for samples exposed to HIC environment

Specimen label	Yield stress (MPa)	Yield Stress Average (MPa)	Maximum stress (MPa)	Max. stress average (MPa)	Tensile strain at Break (%)	Tensile Strain Average (%)	Modulus (MPa)	E, Average (MPa)
A-Charged	397	384.00	513	506.19	10.65	10.27	20131.3277	18667
	371		499		990		17202.08871	
B-Charged	364	379.75	480	486.44	10.28	10.47	19951.14964	19704
	395.5		493		10.66		19457.58977	
C-Charged	527	513.50	623	625.77	10.26	9.99	21805.0349	21566
	500		629		9.72		21326.08176	
D-Charged	498	507.50	583	584.34	12.27	12.63	22392.78971	22454
	517		585		13.00		22516.13392	
E-Charged	466	460.50	572	579.08	12.47	12.39	21715.1991	21980
	455		586		12.31		22245.05081	
F-Charged	557	566.50	663	669.50	10.09	8.93	23527.47226	24169
	576		675		7.77		24811.17481	

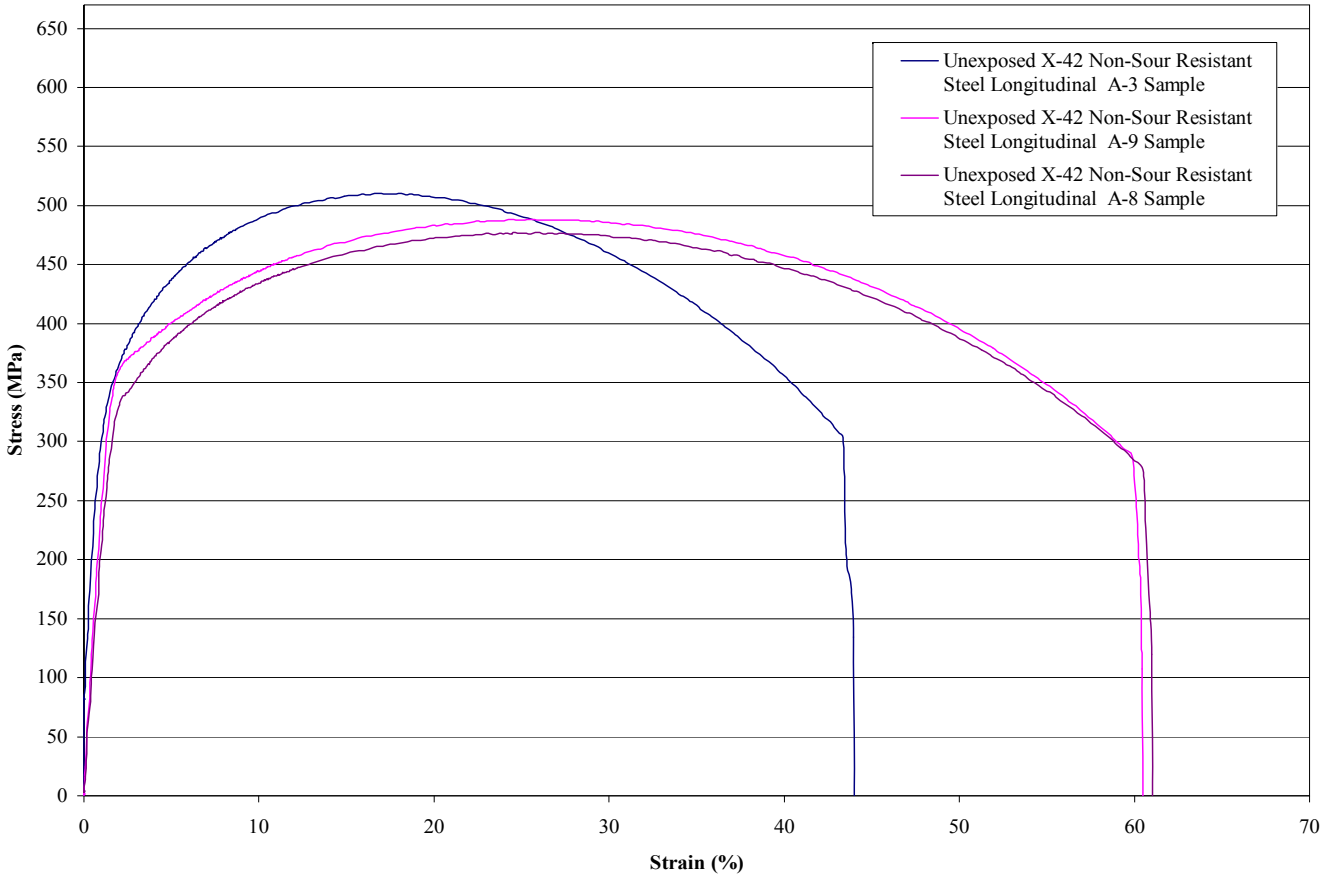

Figure 4.1: Tensile testing curve for type (A) samples unexposed to HIC.

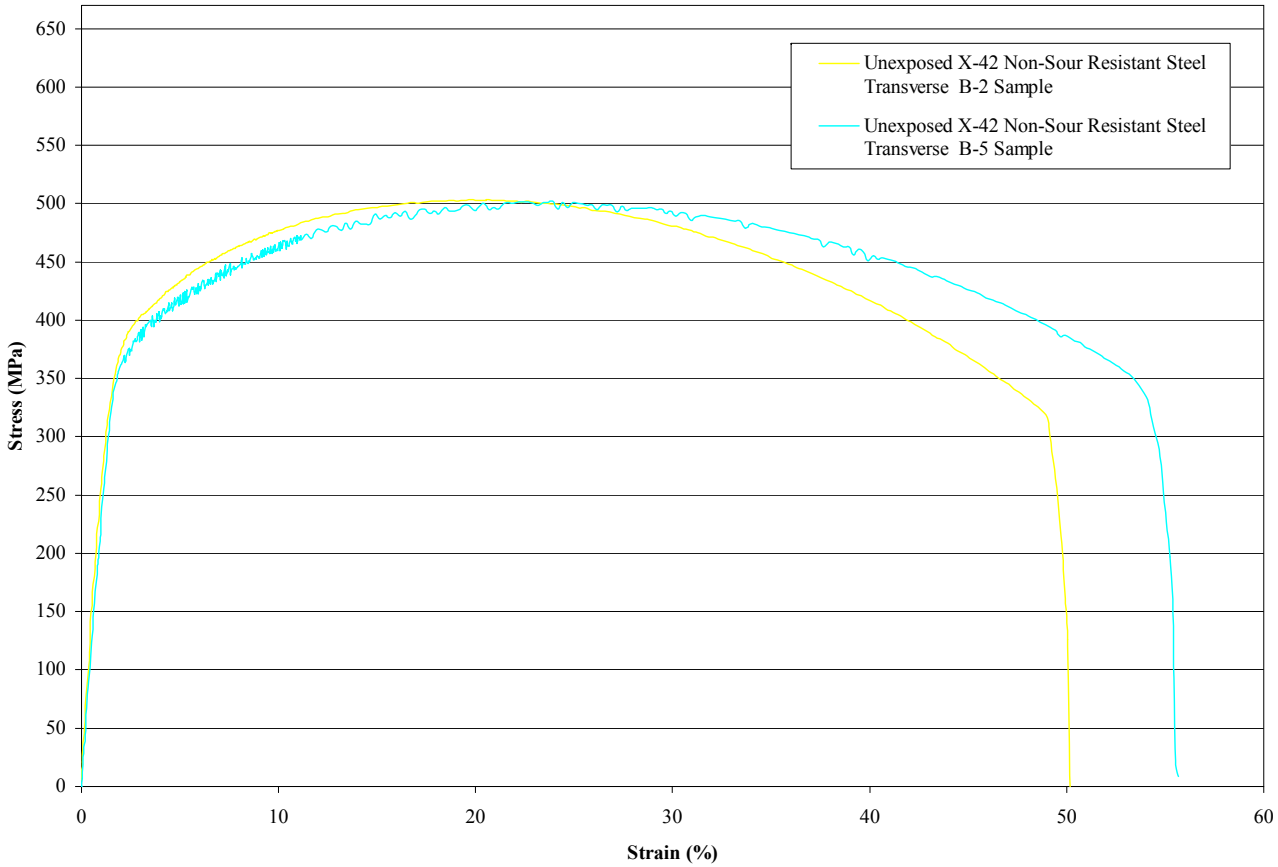

Figure 4.2: Tensile testing curve for type (B) samples unexposed to HIC

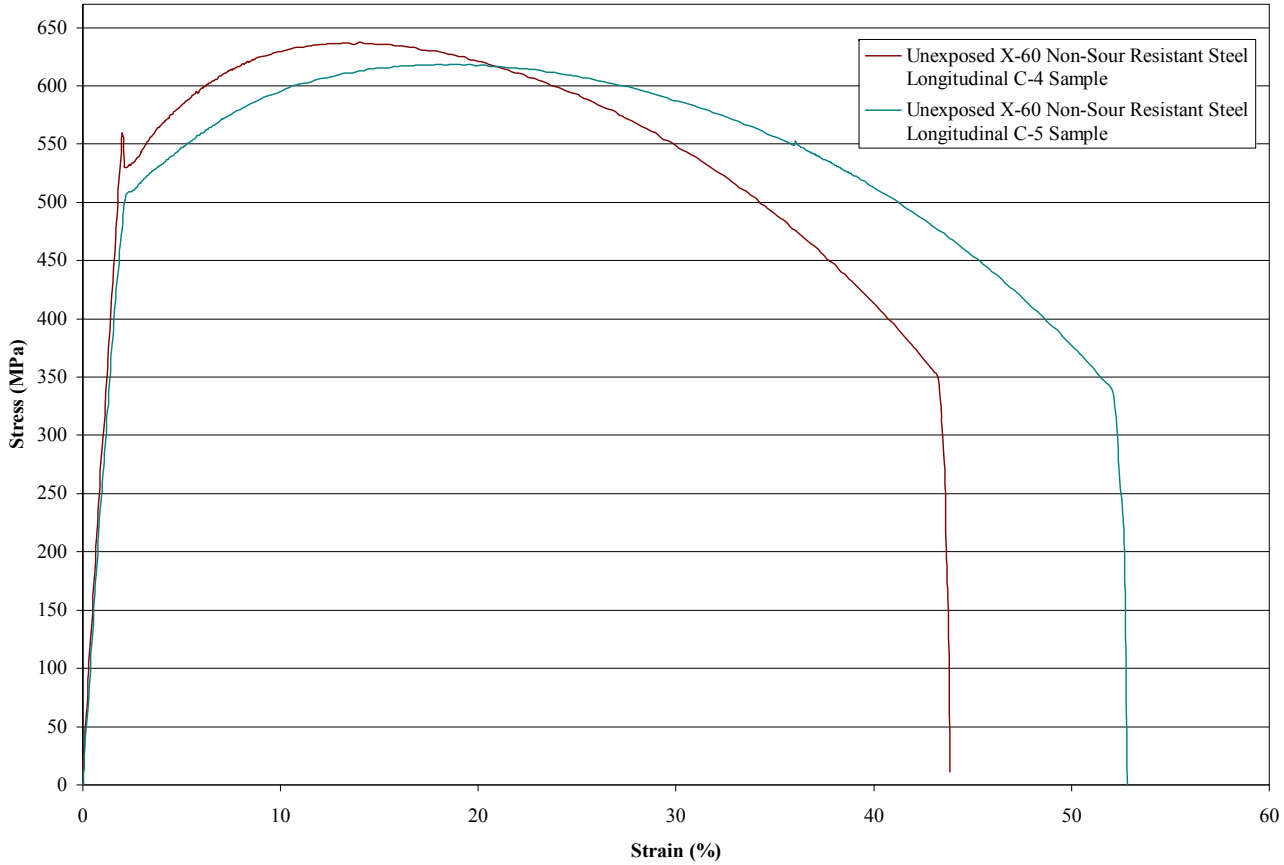

Figure 4.3: Tensile testing curve for type (C) samples unexposed to HIC.

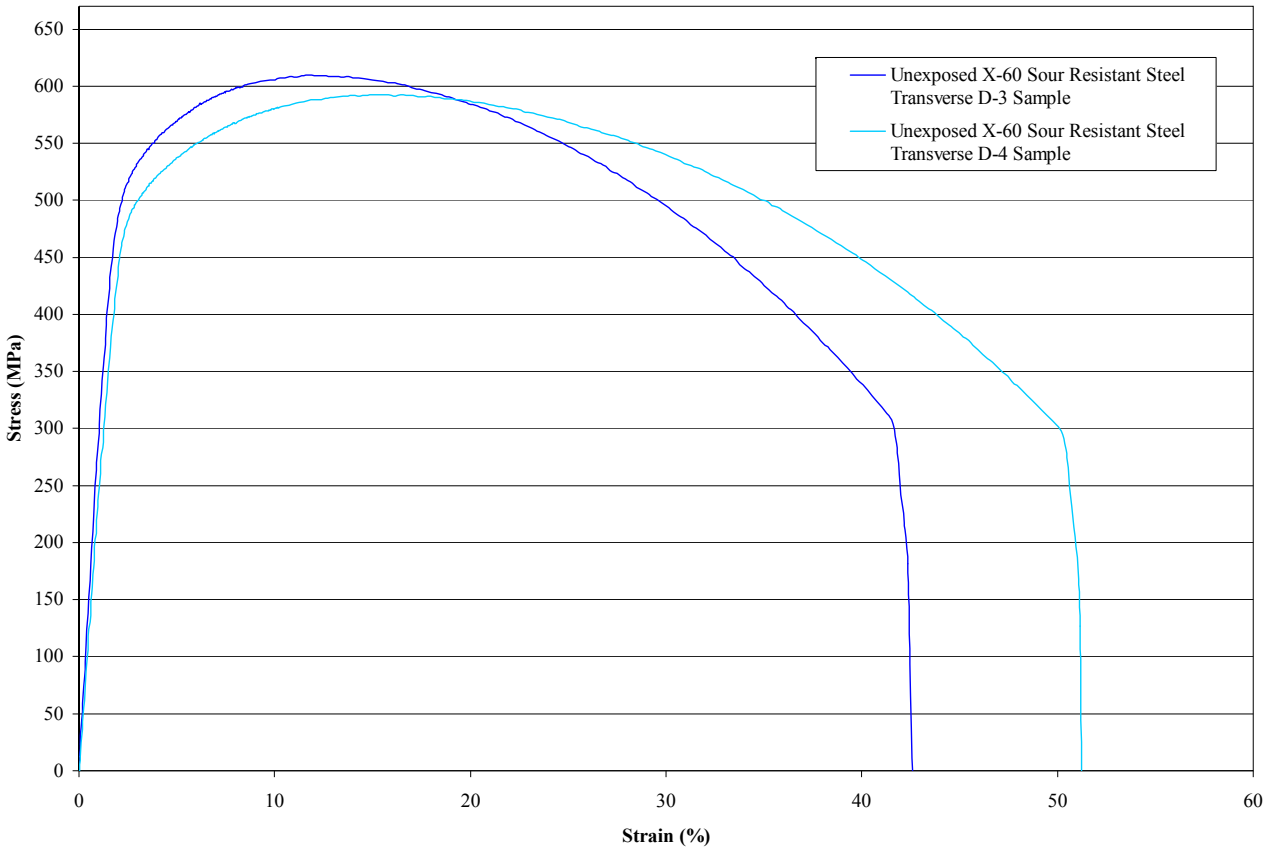

Figure 4.4: Tensile testing curve for type (D) samples unexposed to HIC

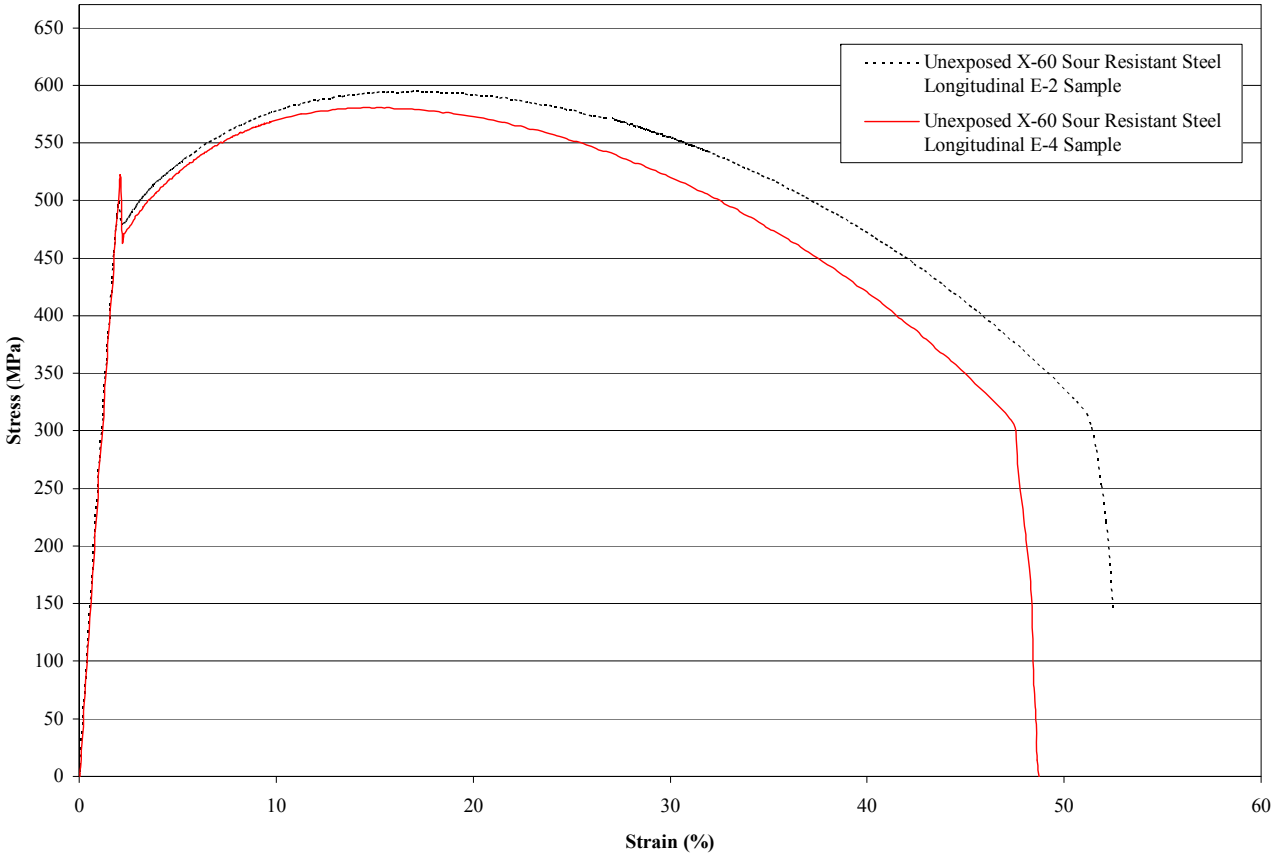

Figure 4.5: Tensile testing curve for type (E) samples unexposed to HIC

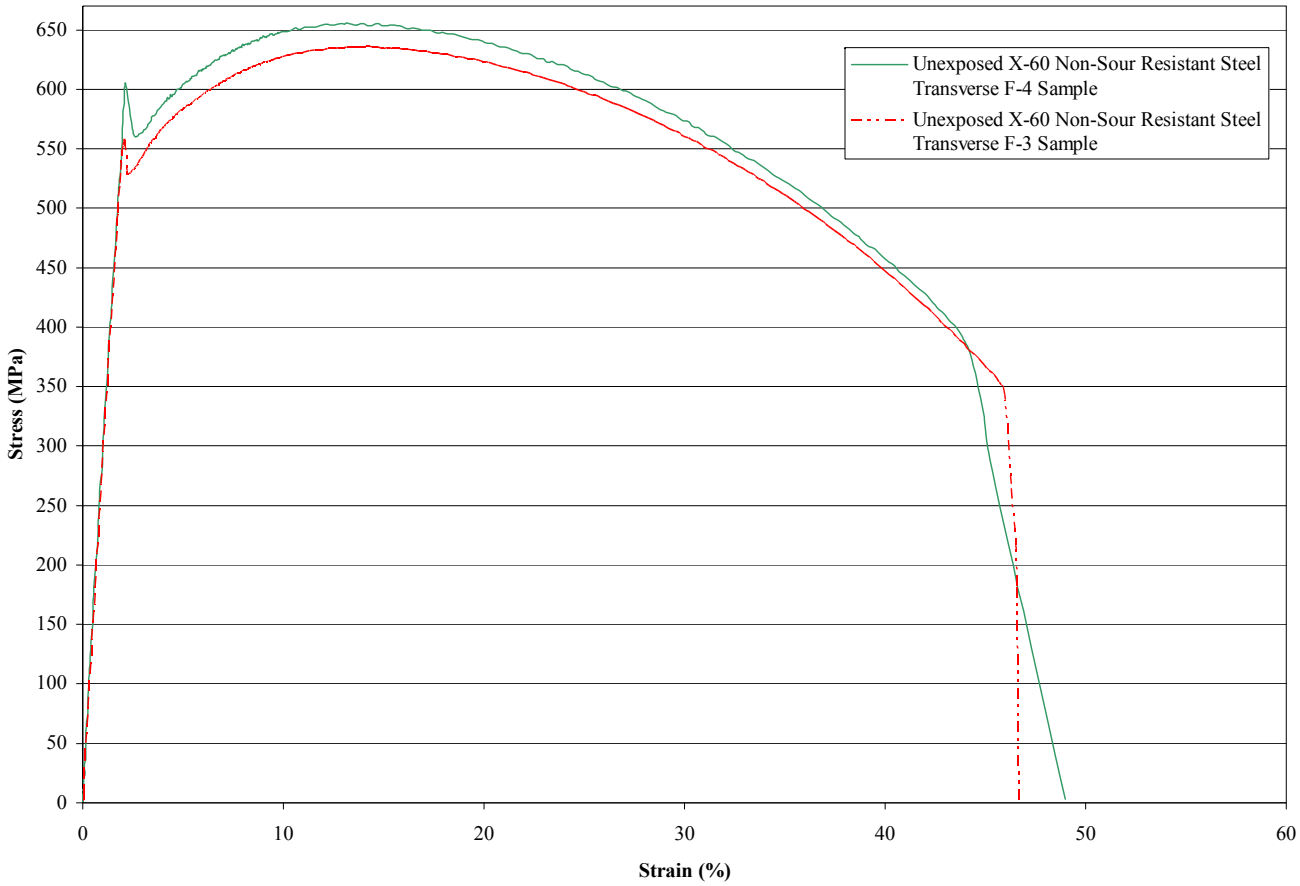

Figure 4.6: Tensile testing curve for type (F) samples unexposed to HIC

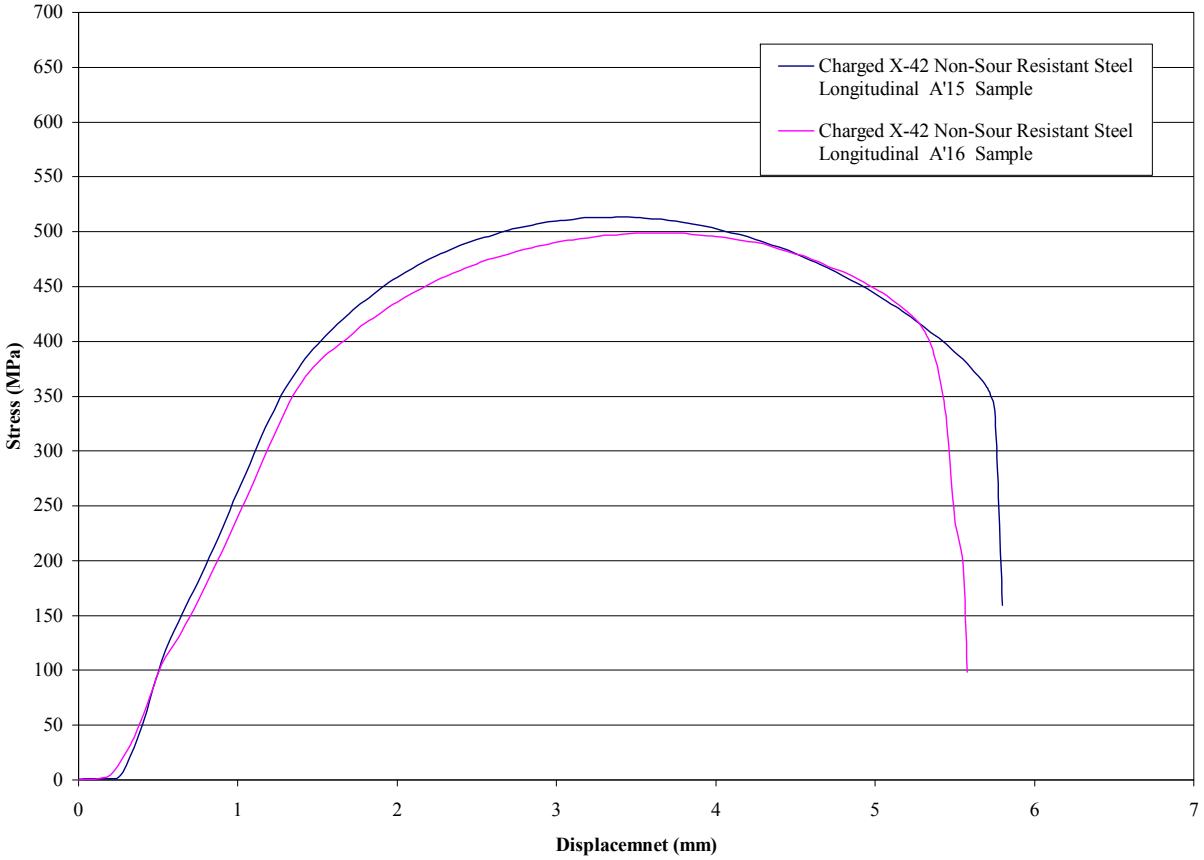

Figure 4.7: Tensile testing curve for type (A') samples exposed to HIC

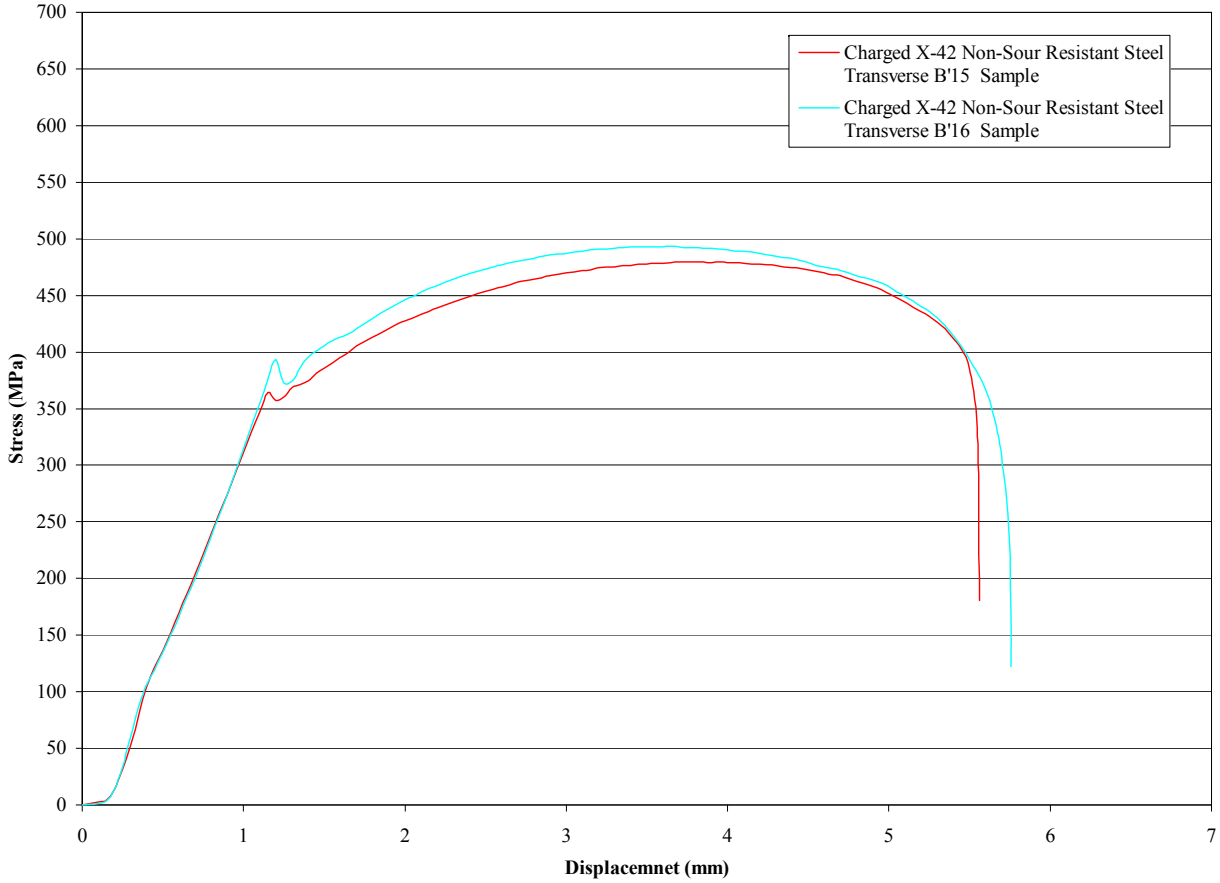

Figure 4.8: Tensile testing curve for type (B') samples exposed to HIC

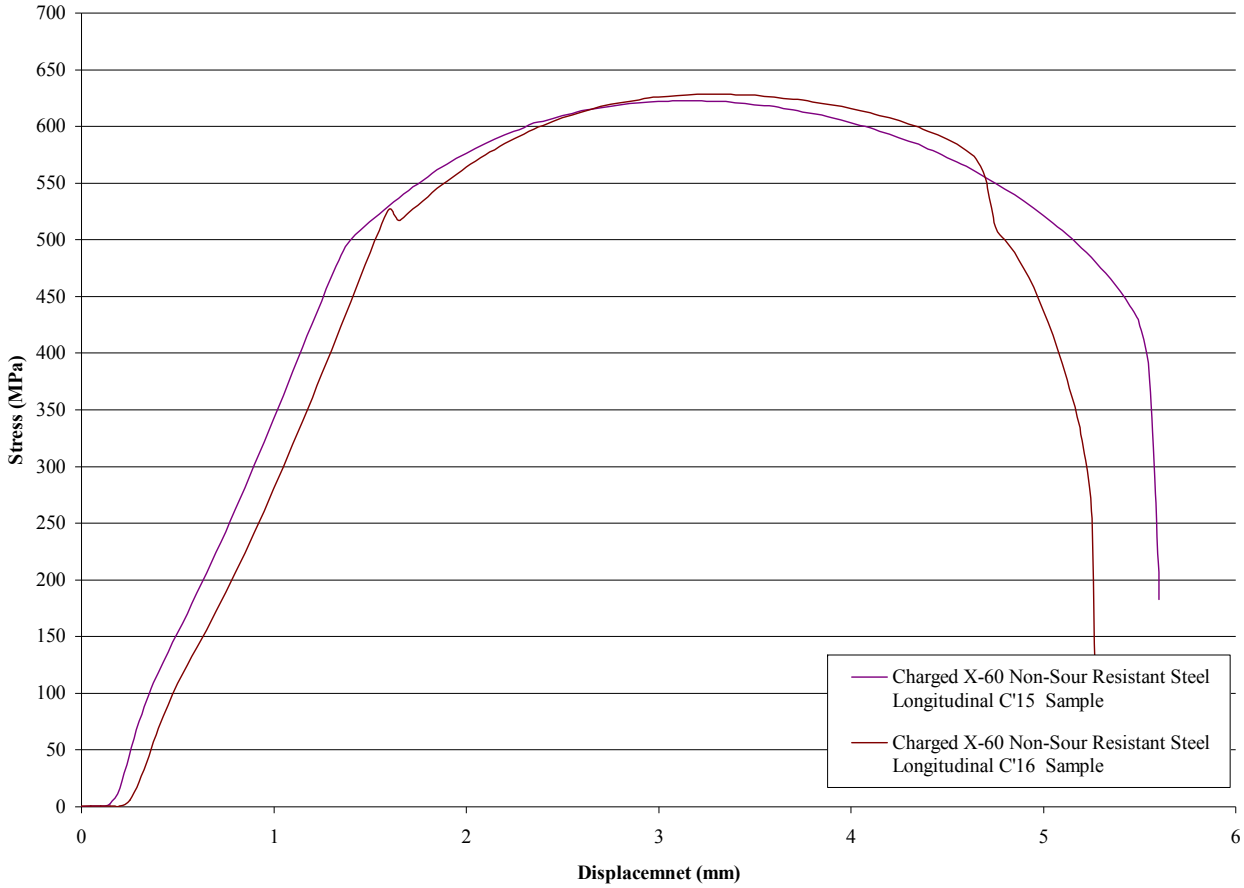

Figure 4.9: Tensile testing curve for type (C') samples exposed to HIC

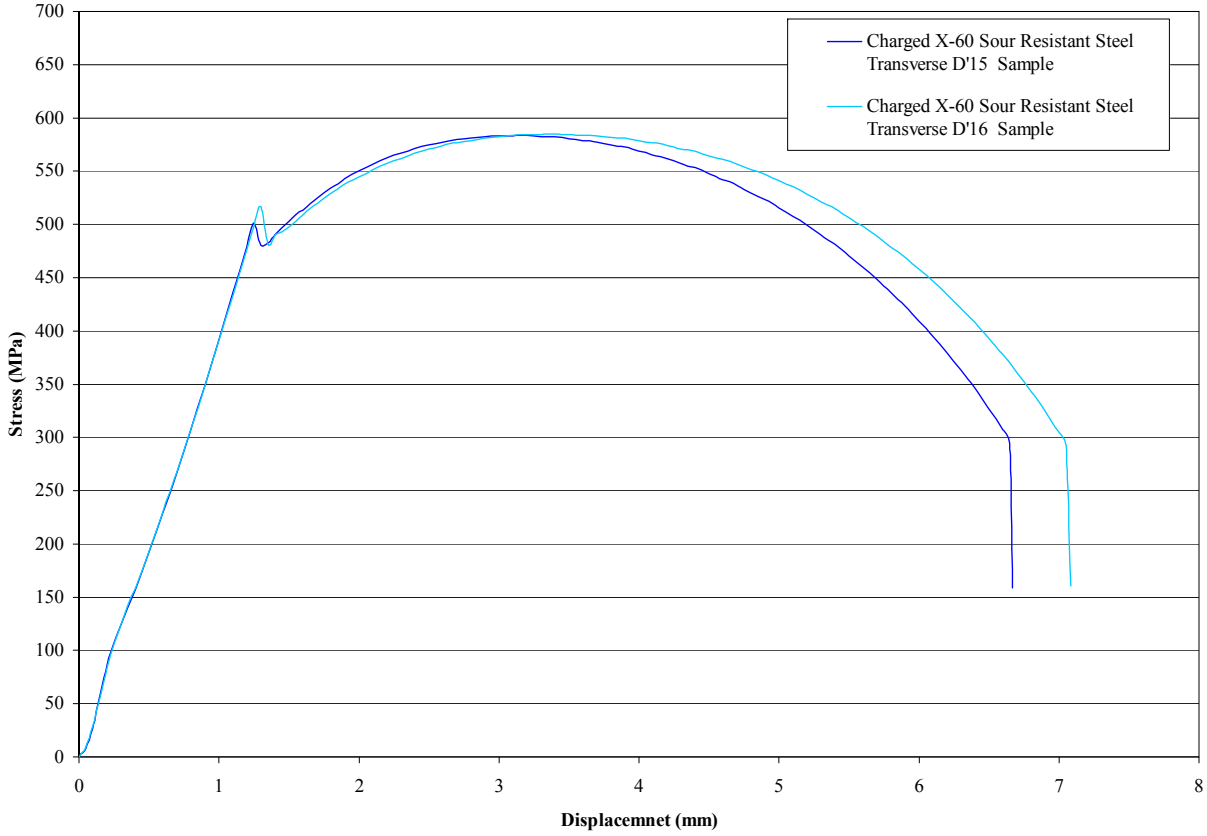

Figure 4.10: Tensile testing curve for type (D') samples exposed to HIC

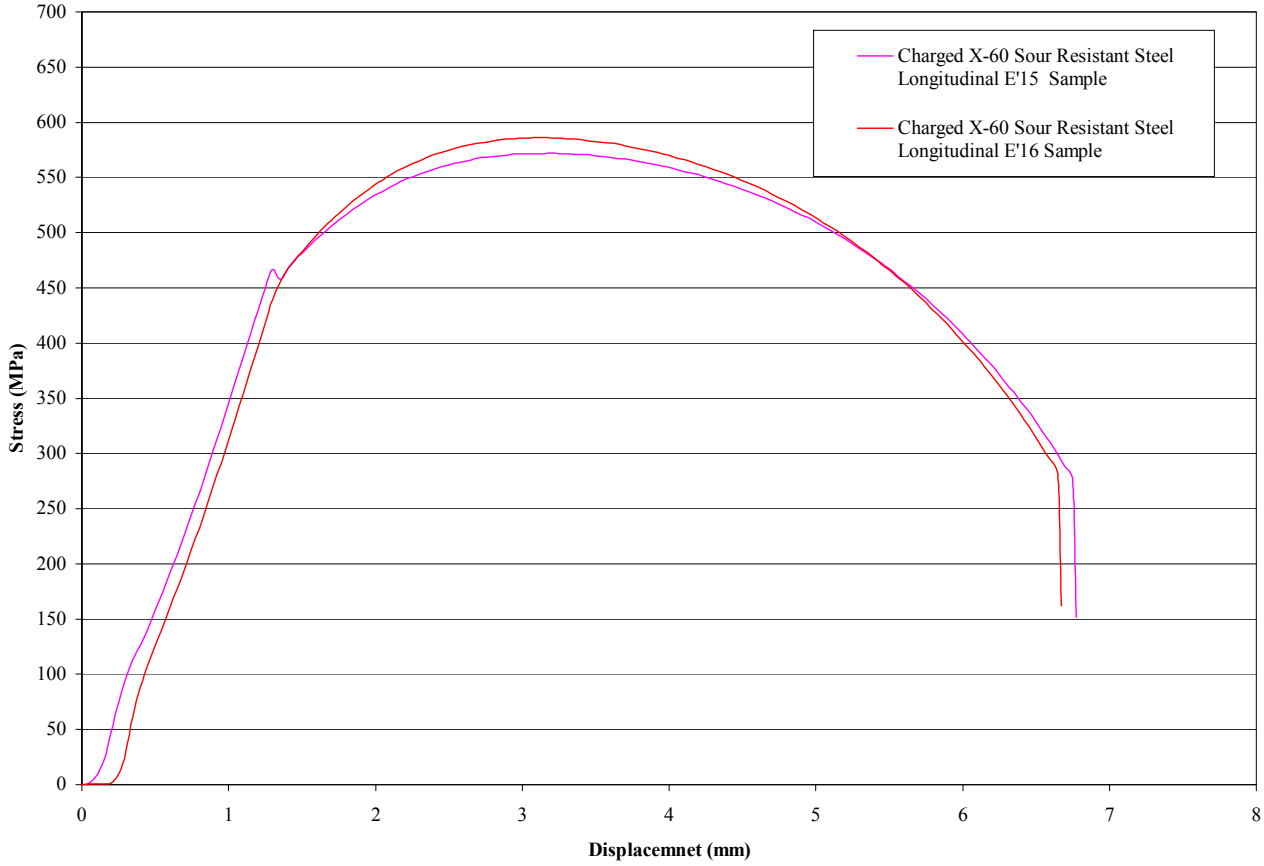

Figure 4.11: Tensile testing curve for type (E') samples exposed to HIC

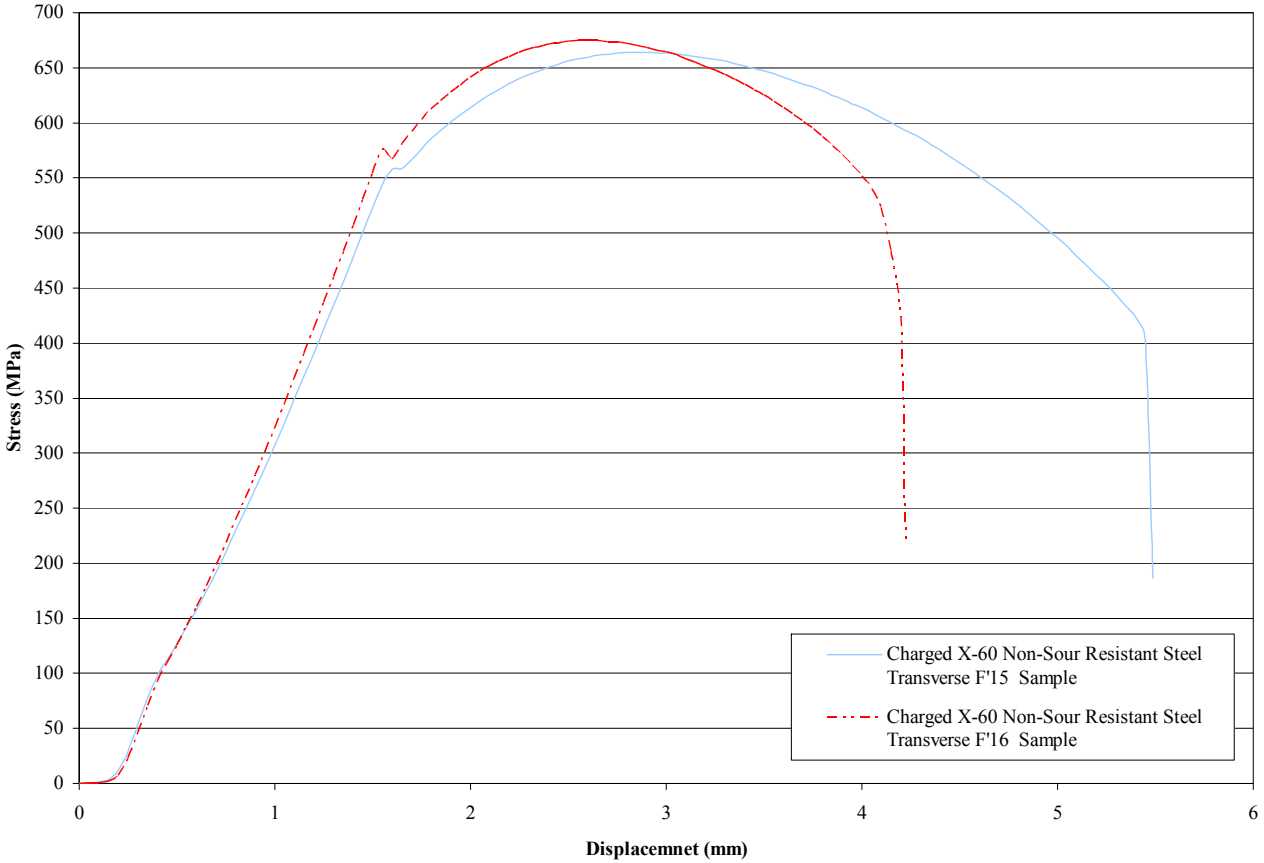

Figure 4.12: Tensile testing curve for type (F') samples exposed to HIC

Table 4-3: Fatique test results of unexposed (A) samples

Sample	Max Load (KN)	Min. Load (KN)	Area (mm^2)	σ_a (MPa)	Life (cycles)	Comment
A10 (85% 485)	12.20	1.22	29.59	185.5	612558	Failed
A11 (80% 485)	11.82	1.18	30.47	174.6	796133	Failed
A13 (90% 485)	13.13	1.31	30.08	196.4	192342	Failed
A16 (75%)	9.94	0.99	27.33	163.7	2000000	Run out
A17 (85%)	11.88	1.19	28.83	185.5	623074	Failed
A18 (85%)	11.88	1.19	28.83	185.5	679808	Failed
A19 (95%)	12.72	1.27	27.60	207.3	114099	Failed
A20 (96%)	12.85	1.29	27.60	209.5	131188	Failed

Table 4-04: Fatigue test results of HIC exposed (A') samples

Sample	Max Load (KN)	Min. Load (KN)	Area (mm^2)	σ_a (MPa)	Life (cycles)	Comment
A'15(75 % 485)	10.28	1.03	28.26	163.7	1323298	Failed
A'4 (80% 485)	11.48	1.15	29.59	174.6	314370	Failed
A'2 (85% 485)	11.65	1.17	28.26	185.5	166524	Failed
A'6 (85% 485)	11.65	1.17	28.26	185.5	135264	Failed
A'5 (90% 485)	12.92	1.29	29.59	196.4	85374	Failed
A'14 (95% 485)	11.83	1.18	25.68	207.3	22659	Failed
A'21 (85%)	11.27	1.13	27.33	185.5	187531	Failed

Table 4-05: Fatigue test results of unexposed (B) samples

Sample	Max Load (KN)	Min. Load (KN)	Area (mm^2)	σ_a (MPa)	Life (cycles)	Comment
B12 (78 %)	11.00	1.10	29.21	169.4	2000000	Run out
B8 (83%)	11.96	1.20	29.79	180.7	809050	Failed
B7 (88%)	12.83	1.28	30.08	192	412849	Failed
B6 (93%)	12.26	1.23	27.14	203.3	348981	Failed
B16 (90%)	12.75	1.28	29.21	196.4	331148	Failed
B17 (90%)	12.29	1.23	28.17	196.4	342594	Failed
B18 (90%)	12.21	1.22	27.98	196.4	307263	Failed
B19 (96%)	13.03	1.30	27.98	209.5	80976	Failed

Table 4-6: Fatigue test results of HIC exposed (B') samples

Sample	Max Load (KN)	Min. Load (KN)	Area (mm^2)	σ_a (MPa)	Life (cycles)	Comment
B'11 (75 % 485)	10.94	1.09	30.08	163.7	2500000	Run out
B'3 (80 % 485)	12.32	1.23	31.75	174.6	641233	Failed
B'1 (85 % 485)	11.65	1.17	28.26	185.5	380061	Failed
B'15 (90 % 485)	13.60	1.36	31.16	196.4	312654	Failed
B'4 (96 % 485)	13.16	1.32	28.26	209.5	56382	Failed
B'21 (85%)	11.46	1.15	27.79	185.5	192499	Failed
B'22 (85%)	11.42	1.14	27.70	185.5	222979	Failed

Table 4-7: Fatigue test results of unexposed (C) samples

Sample	Max Load (KN)	Min. Load (KN)	σ_a (MPa)	Area (mm^2)	Life (cycles)	Comment
C7 (75%)	12.78	1.28	211.9	27.14	2000000	Runout
C15 (80%)	14.10	1.41	226.1	28.07	362123	Failed
C11 (85%)	14.74	1.47	240.2	27.60	173073	Failed
C8 (90%)	15.87	1.59	253.1	28.07	136211	Failed
C17 (90%)	15.63	1.56	253.1	27.79	136588	Failed
C18 (90%)	15.53	1.55	253.1	27.60	172849	Failed
C19 (95%)	19.69	1.97	267.2	33.17	36073	Failed

Table 4-8: Fatigue test results of HIC exposed (C') samples

Sample	Max Load (KN)	Min. Load (KN)	Area (mm^2)	σ_a (MPa)	Life (cycles)	Comment
C'2(80 % 625)	12.71	1.27	25.42	225	1438444	Failed
C'1(85 % 625)	15.01	1.50	28.26	239.1	141852	Failed
C'10(90 % 625)	15.53	1.55	27.60	253.1	278297	Failed
C'3 (88 % 625)	16.11	1.61	27.14	247.5	77398	Failed
C'21 (75%)	12.91	1.29	27.42	211.9	364290	Failed
C'22(88%)	15.23	1.52	27.70	247.5	110235	Failed
C'23(88%)	15.29	1.53	27.79	247.5	130235	Failed

Table 4-9: Fatigue test results of unexposed (D) samples

Sample	Max Load (KN)	Min. Load (KN)	σ_a (MPa)	Area (mm^2)	Life (cycles)	Comment
D11 (81%)	13.65	1.36	202.8	30.27	2000000	Runout
D14 (92%)	13.91	1.39	229.9	27.23	299346	Failed
D13 (97%)	15.85	1.59	243.4	29.31	123598	Failed
D16 (80%)	12.45	1.24	199.6	28.07	2000000	Runout
D17 (92%)	14.10	1.41	229.9	27.60	365924	Failed
D18 (92%)	14.29	1.43	229.9	27.98	300254	Failed
D19 (92%)	14.10	1.41	229.9	27.60	414232	Failed

Table 4-10: Fatigue test results of HIC exposed (D') samples

Sample	Max Load (KN)	Min. Load (KN)	Area (mm^2)	σ_a (MPa)	Life (cycles)	Comment
D'5 (65 % 554.3)	10.18	1.02	28.26	162.2	2500000	Run out
D'6 (80% 554.34)	13.12	1.31	29.59	199.6	2500000	Run out
D'2 (85% 554.34)	15.01	1.50	31.85	212	1152352	Failed
D'10 (90% 554.3)	14.62	1.46	29.31	224.5	160341	Failed
D'9 (95% 554.34)	16.10	1.61	30.57	237	140152	Failed
D'8 (98% 554.34)	16.61	1.66	30.57	244.5	126651	Failed
D'21 (85% 554.3)	13.09	1.31	27.79	212	522652	Failed
D'22 (85% 554.3)	13.09	1.31	27.79	212	653626	Failed

Table 4-11: Fatigue test results of unexposed (E) samples

Sample	Max Load (KN)	Min. Load (KN)	Area (mm^2)	σ_a (MPa)	Life (cycles)	Comment
E13 (79%)	11.79	1.18	26.77	198.1	2000000	Runout
E11 (83%)	14.45	1.44	31.55	206	410253	Failed
E14 (90%)	14.10	1.41	28.26	224.5	142498	Failed
E15 (85%)	14.54	1.45	30.96	212	254092	Failed
E16 (85%)	13.23	1.32	28.07	212	478572	Failed
E17 (85%)	13.23	1.32	28.07	212	337248	Failed
E19 (98%)	15.10	1.51	27.79	244.5	65698	Failed

Table 4-12: Fatigue test results of HIC exposed (E') samples

Sample	Max Load (KN)	Min. Load (KN)	Area (mm^2)	σ_a (MPa)	Life (cycles)	Comment
E'6(80% 554.34)	12.41	1.24	27.98	199.6	2000000	Run out
E'1 (85 % 554.3)	13.32	1.33	28.26	212	542750	Failed
E'(90% 554.34)	14.29	1.43	28.64	224.5	197015	Failed
E'7 (95% 554.34)	15.94	1.59	30.27	237	131251	Failed
E'21 (85%)	13.09	1.31	27.79	212	518474	Failed
E'22 (85%)	12.88	1.29	27.33	212	483212	Failed
E'23 (95%)	14.39	1.44	27.33	237	130432	Failed

Table 4-13: Fatigue test results of unexposed (F) samples

Sample	Max Load (KN)	Min. Load (KN)	Area (mm^2)	σ_a (MPa)	Life (cycles)	Comment
F5 (85%)	15.43	1.54	29.21	237.6	253731	Failed
F7 (93%)	15.36	1.54	26.50	260.8	106926	Failed
F8 (88%)	15.37	1.54	28.07	246.3	153118	Failed
F13 (82%)	14.08	1.41	27.33	231.8	2000000	Run out
F16 (90%)	13.85	1.38	24.62	253.1	250596	Failed
F17 (90%)	16.43	1.64	29.21	253.1	251726	Failed
F18 (90%)	13.02	1.30	23.15	253.1	207256	Failed
F19 (95%)	14.10	1.41	23.75	267.2	90356	Failed

Table 4-14: Fatigue test results of HIC exposed (F') samples

Sample	Max Load (KN)	Min. Load (KN)	Area (mm^2)	σ_a (MPa)	Life (cycles)	Comment
F'14(80 % 625)	12.62	1.26	25.24	225	2500000	Run out
F'2 (85 % 625)	15.01	1.50	28.26	239.1	186505	Failed
F'10 (88 % 625)	13.90	1.39	24.71	247.5	220045	Failed
F'21 (88%)	14.52	1.45	26.41	247.5	263742	Failed
F'22 (88%)	14.83	1.48	26.96	247.5	211895	Failed
F'23 (90%)	14.65	1.46	26.04	253.1	121888	Failed

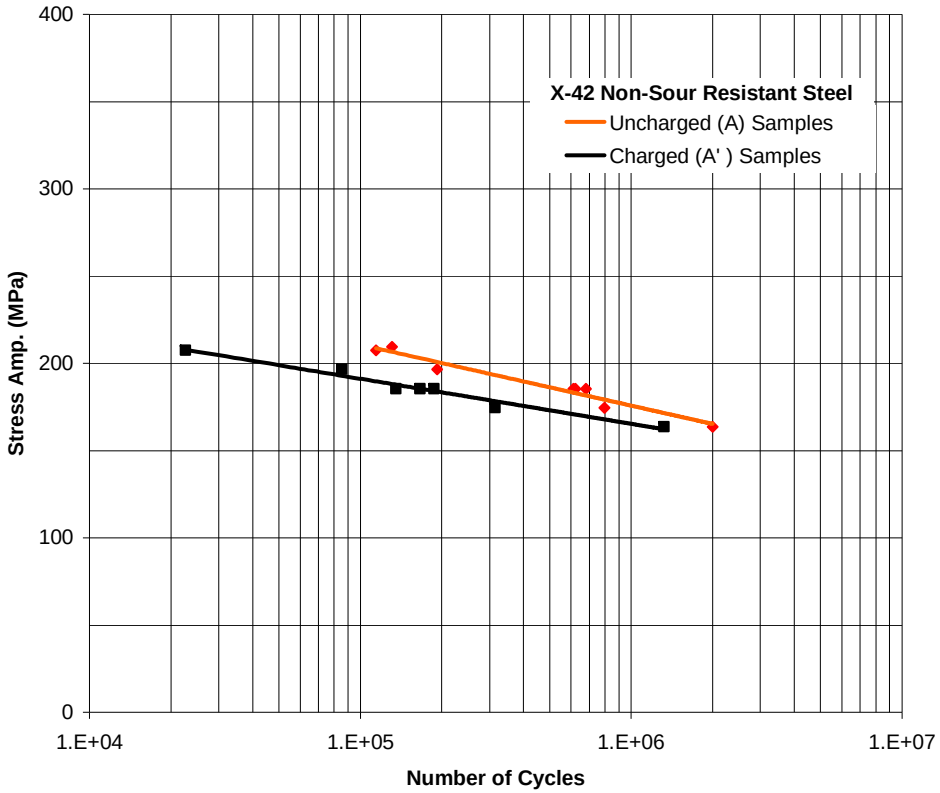

Figure 4.13: S-N Curves for (A) and (A') Samples

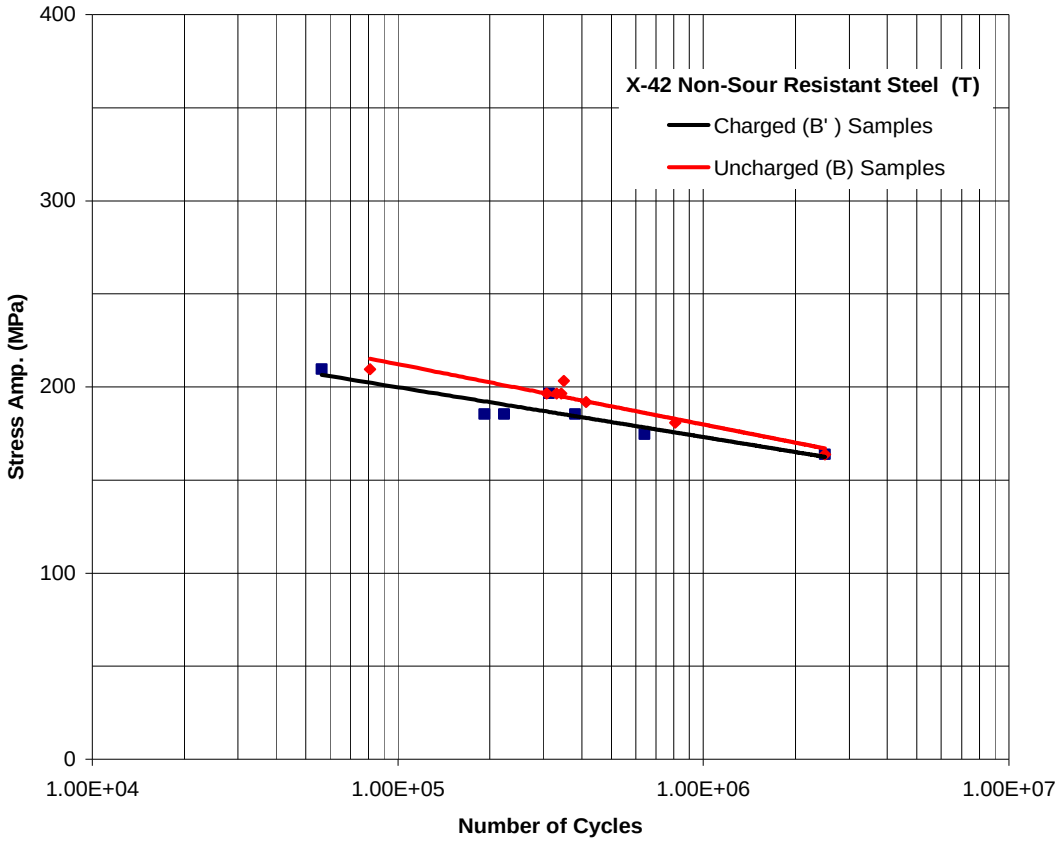

Figure 4.14: S-N Curves for (B) and (B') Samples

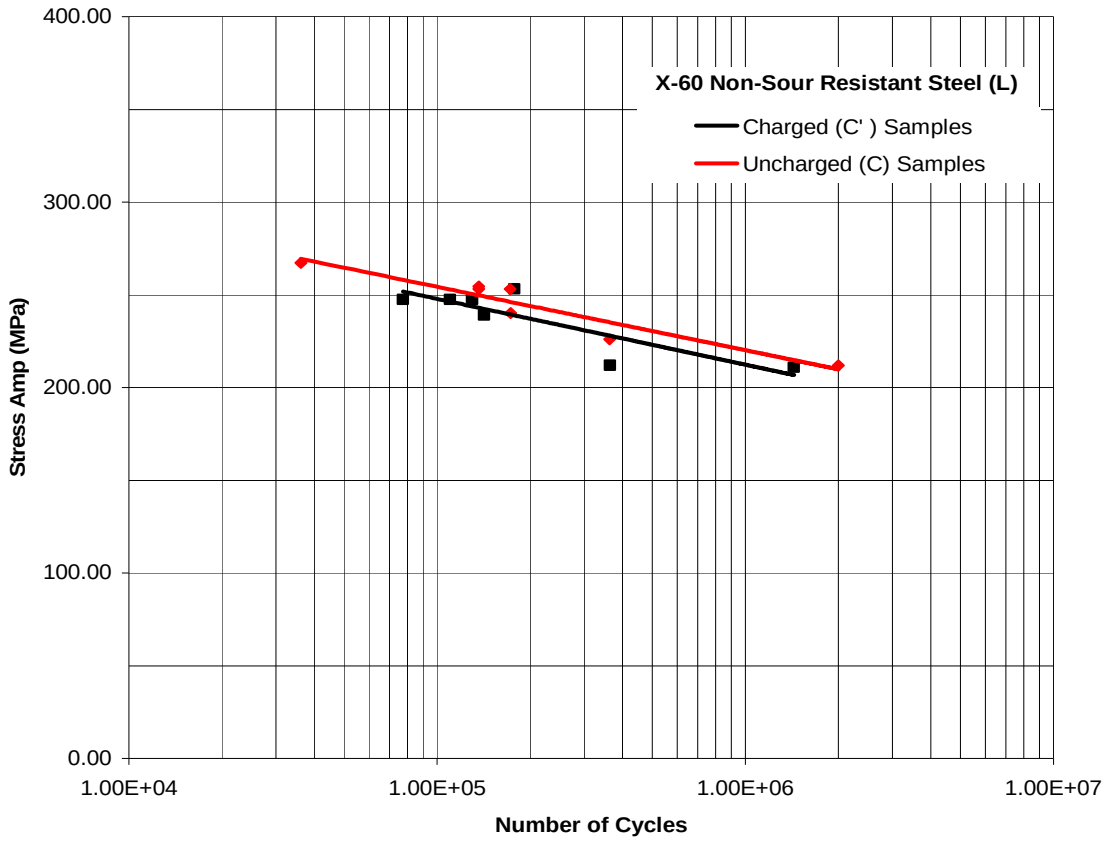

Figure 4.15: S-N Curves for (C) and (C') Samples

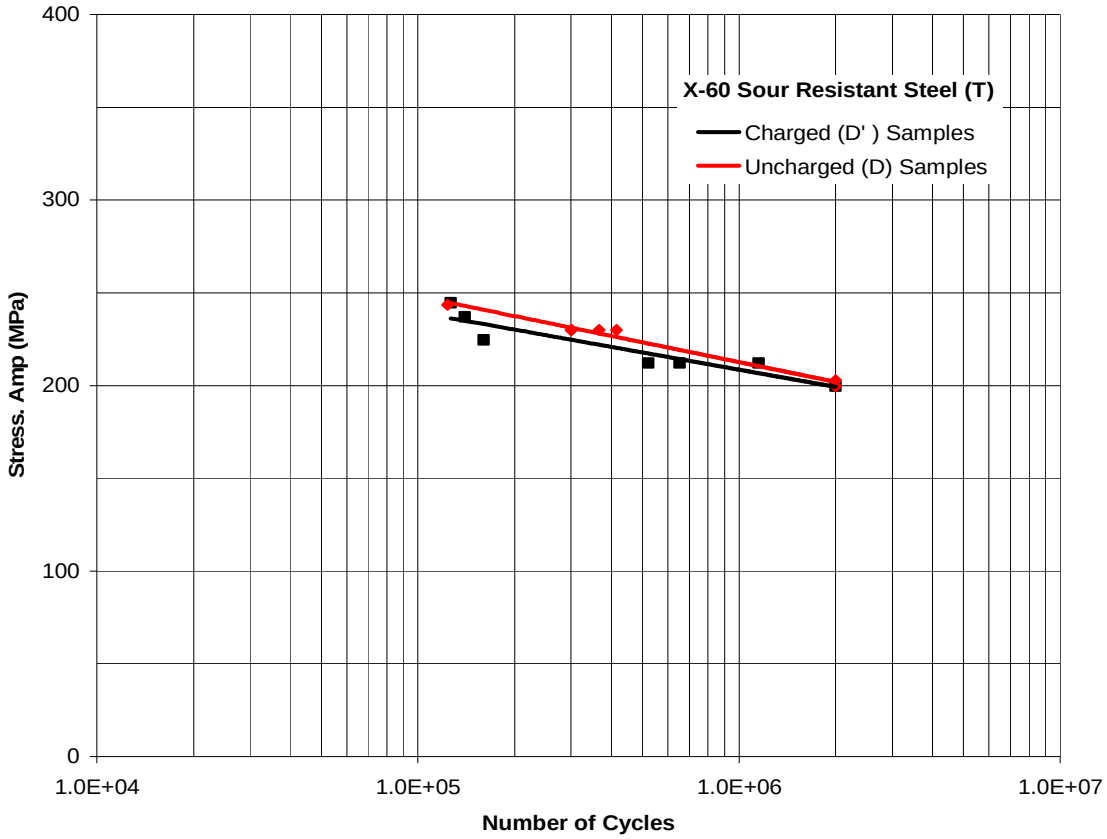

Figure 4.16: S-N Curves for (D) and (D') Samples

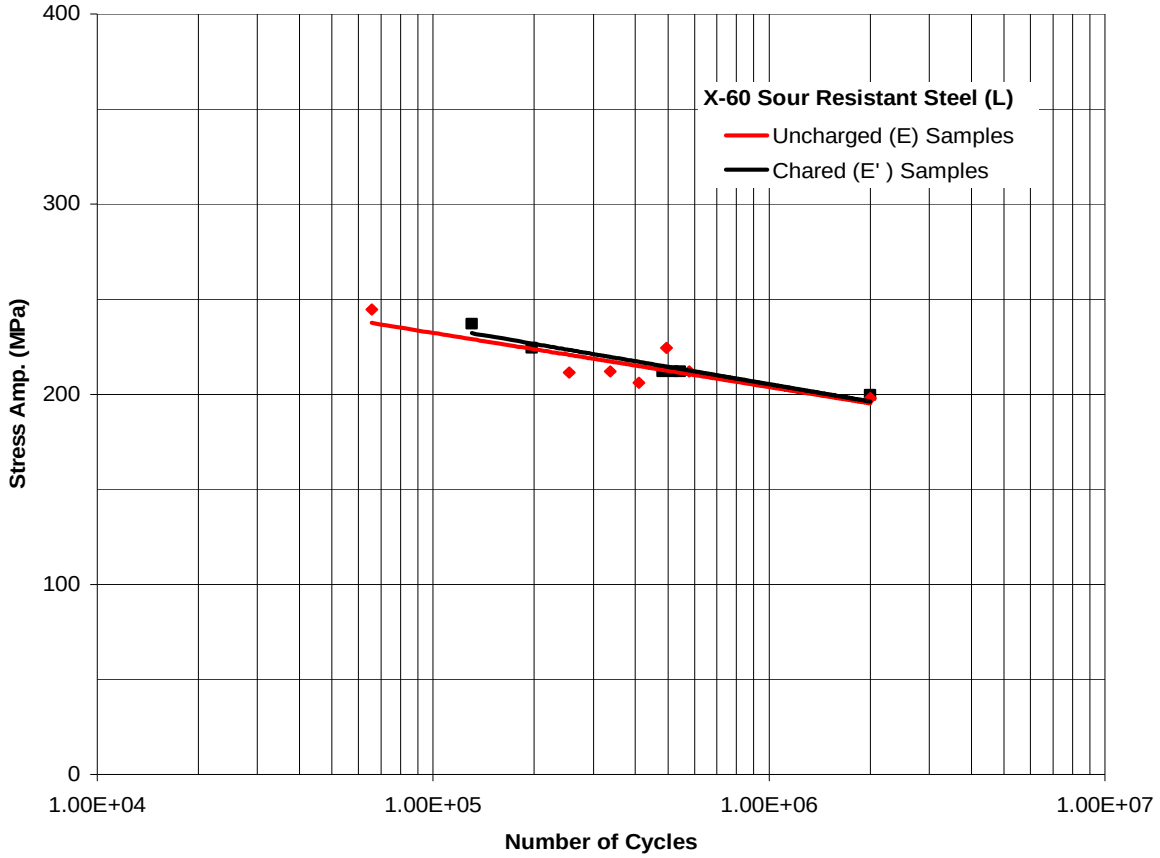

Figure 4.17: S-N Curves for (E) and (E') Samples

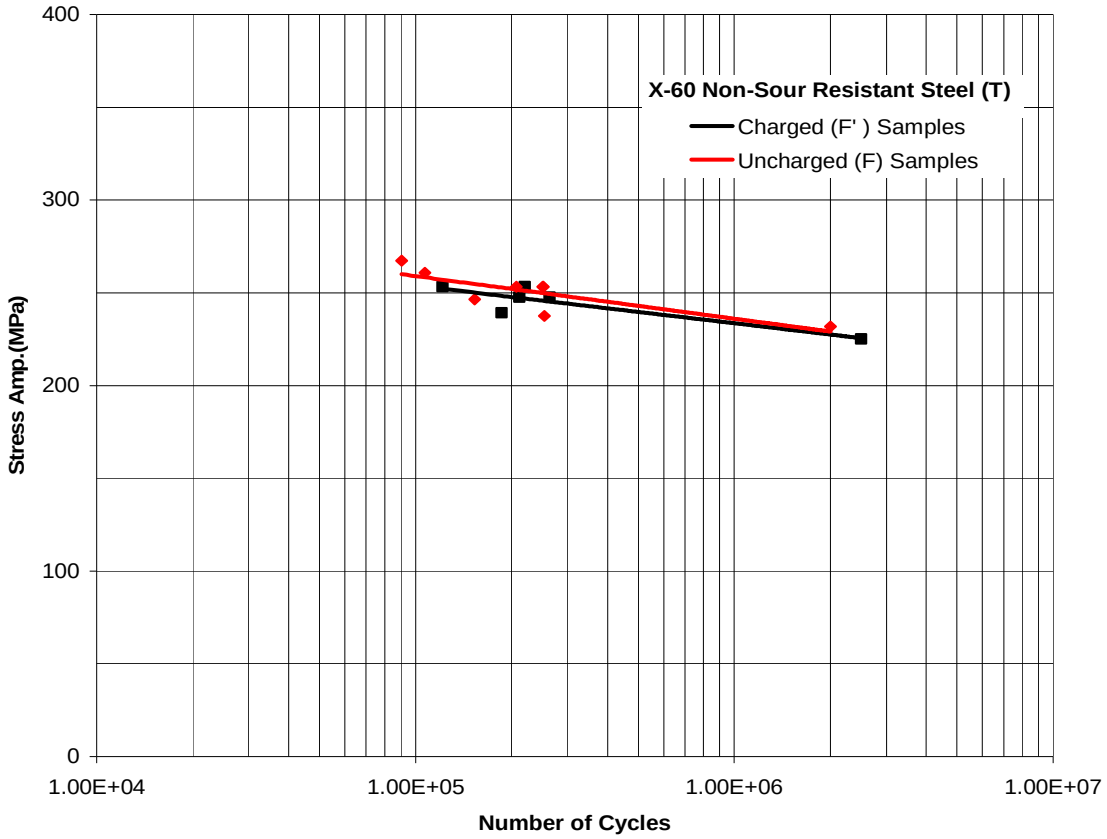

Figure 4.18: S-N Curves for (F) and (F') Samples

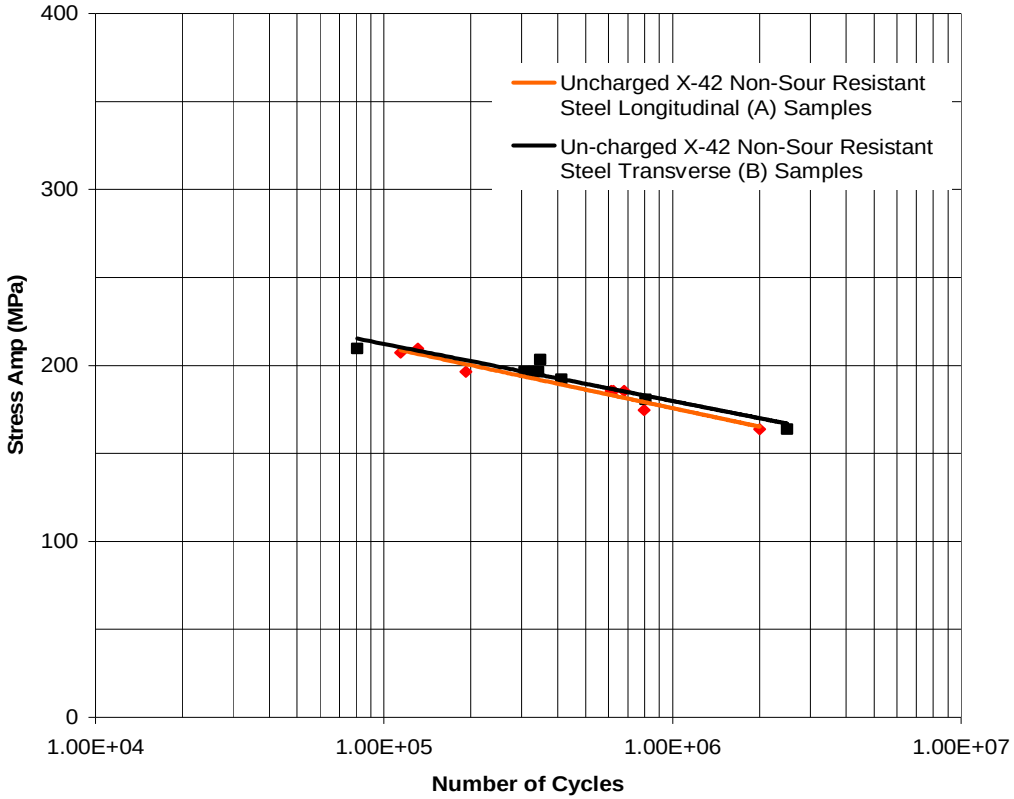

Figure 4.19: S-N Curve for (A) and (B) Uncharged Samples

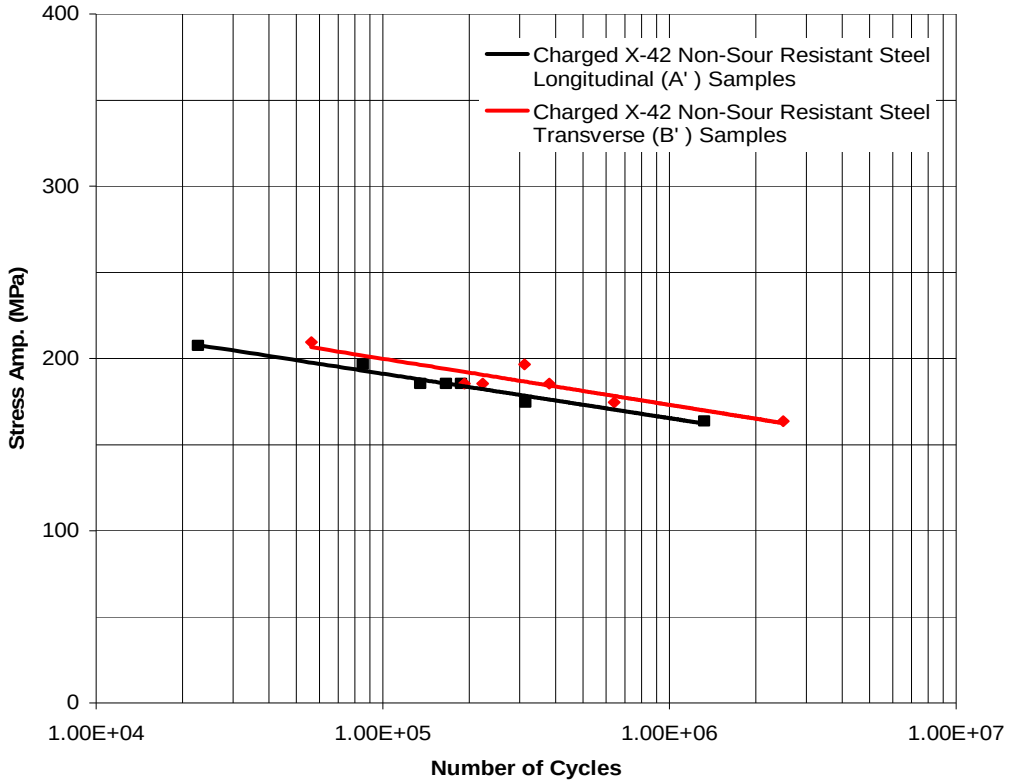

Figure 4.20: S-N Curves for (A') and (B') Charged Samples

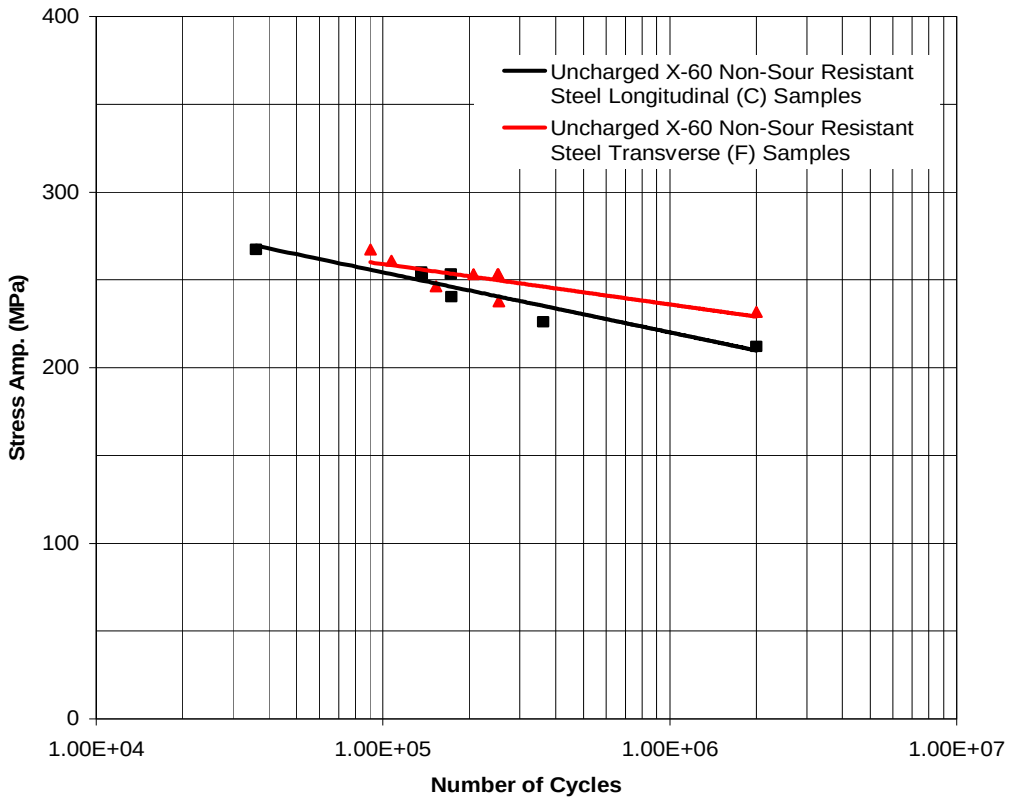

Figure 4.21: S-N Curves for (C) and (F) Uncharged Samples

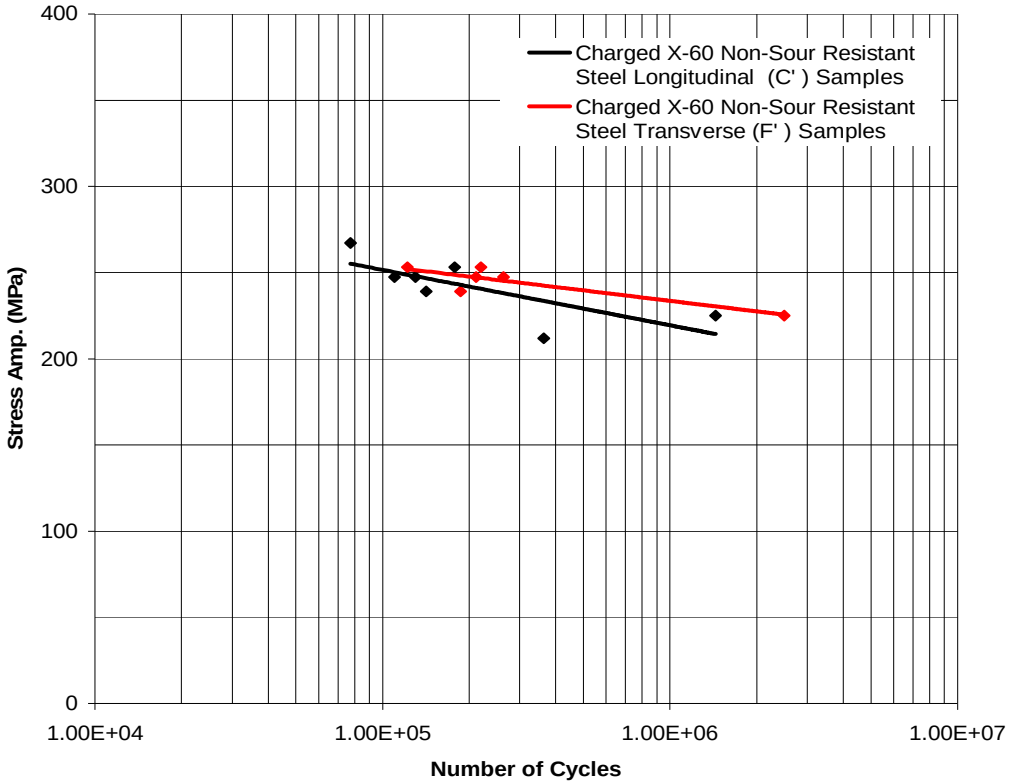

Figure 4.22: S-N Curves for (C') and (F') Charged Samples

Chapter 5

5. CALCULATION OF CRACK LENGTH AND THICKNESS RATIO

Cracks are measured on metallographic samples by using a microscope. Crack measurements are done longitudinally to calculate the crack length ratio (CLR) and through the width of the sample to calculate crack thickness ratio (CTR). Crack length ratio is determined by total crack length divided by the length of the sample. Crack thickness ratio is calculated by measuring the total extend of stepwise cracking divided by the width of the sample, as illustrated in Figures 5.1 and 5.2.

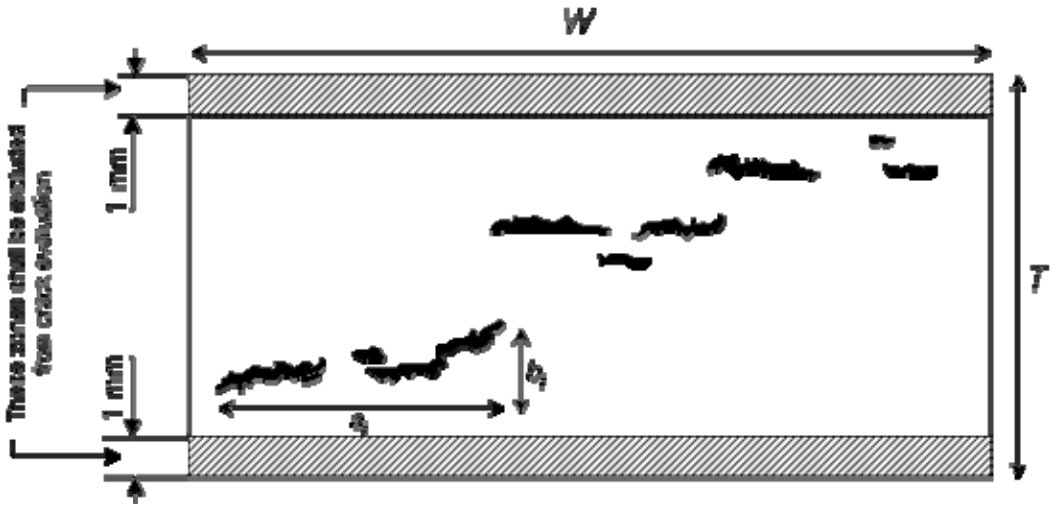

Figure 5.1: The CLR and CTR measurements in a metallographic section.

Length of stepwise crack: $\sum a_i$ Thickness of stepwise crack: $\sum b_i$

$$CLR = \frac{\sum_{i=1}^{n} a_i}{W} \times (100\%) \qquad CTR = \frac{\sum_{i=1}^{n} b_i}{T} \times (100\%)$$

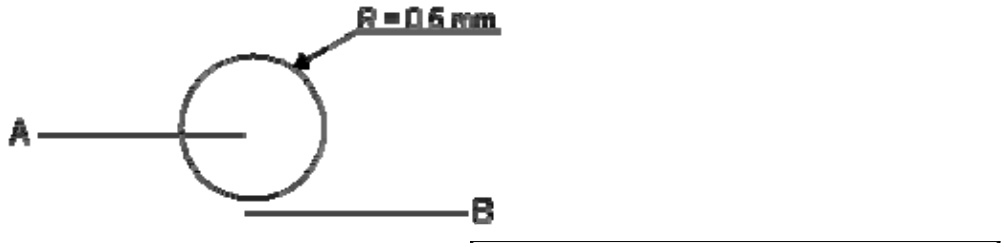

If cracks A and B are separated by more than 0.5 mm, then they are measured as two separate cracks.

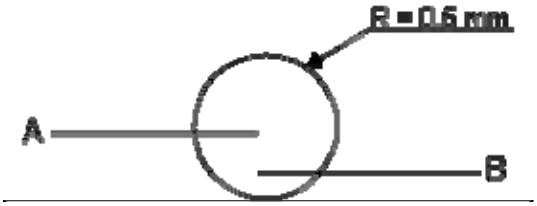

If the distance is less than 0.5 mm, then cracks A and B are considered as a single crack in the measurement.

Figure 5.2: Method for measuring and evaluating cracks on a metallograph

Table 5-1: Measurements of crack length ratio of specimen

Grade	Sample Direction	Sample No.	Expose to HIC test	Crack Length Ratio CLR %	Crack Thickness CT	Comments
X42 non sour	L	A2	No			un failed
		A4	Yes	19.9	0.144	
		A5	Yes	0	0	
		A6	Yes	23	0.24	
		A7	Yes			
		A12	Yes			
		A14	Yes			
X42 non sour	T	B1	Yes	6.9	0.003	
		B4	No	0	0	un failed
		B9	Yes			
		B10	Yes	8.0	1.8	
		B11	Yes			un failed
		B13	Yes	1.11	0.24	
		B15	Yes			
X60 non sour	L	C1	Yes	0	0	un failed
		C7	No	0	0	
		C2	Yes	19.5		
		C3	Yes	0.087	0.02	
		C4	Yes			un failed
		C6	Yes			
		C9	No			
		C10	Yes			
		C13	Yes			
X60 sour resistant	T	D1	No			un failed
		D2	Yes	0	0	
		D5	Yes			
		D5				un failed
		D6	Yes			un failed
		D7	Yes	0	0	
		D8	Yes	0	0	
		D10	Yes			
X60 sour resistant	L	E1	No	0	0	un failed
		E6	Yes			
		E7	Yes	0	0	
		E8	Yes	0	0	
		E9	Yes	0	0	
		E12	Yes	0	0	
X60 non sour	T	F1	No	0	0	un failed
		F2	Yes	0.31	0.06	
		F4	Yes			
		F6	Yes	1.93	0.4	
		F9	Yes	0	0	
		F11	Yes			
		F12	Yes			

Chapter 6

6. METALLOGRAPHIC AND FRACTOGRAPHIC EXAMINATION

Metallographic samples were prepared from longitudinal sections of fatigue-tested samples for microscopic examination. The crack length ratio (CLR) and crack thickness ratio (CTR) were measured for samples from the different types of materials for comparison purposes. Table 5.1 presents the measurements of the crack length ratio and the crack thickness of specimen.

As shown in Table 5.1 measurements revealed that the crack length ratio of A' samples that were prepared longitudinally to the rolling direction of grade X-42 non-sour resistant carbon steel were larger than the CLR of B' type samples that were prepared transverses to the rolling direction of the same steel.

Also C' samples that were prepared from sections longitudinal to the rolling direction of grade X-60 non-sour resistant carbon steel have a CLR larger than F' type samples that were prepared transversely to the rolling direction of the same steel. The difference in the CLR observed in table 5.1 shows that HIC cracking give preferentiality to propagating along the rolling direction of the steel. The preferentiality with direction in

HIC crack propagation is attributed to the presence of banding and lamination along the rolling direction of the steel.

The crack thickness ratio measurements did not reveal a significant difference between the samples. Samples type D' and E', that were prepared from sections longitudinal and transverse to the rolling direction of grade X-60 sour resistant carbon steel, did not develop HIC cracking.

Figure 6.1 is a photograph of a section that is taken from Grade X-42 non-sour resistant steel longitudinal to the rolling direction, and it shows HIC step-wise cracking.

Figure 6.2 is a photograph of sample A'4 at a magnification of 200X, nital etched. The microstructure of the etched sample revealed the presence of banding which acted as an initiation site for HIC cracking.

Figure 6.3 is a photograph of sample A'6 at a magnification of 16X and it shows stepwise cracking. Figure 6.4 is a micrograph of A'6 at a higher magnification (125X) and it shows that cracking initiated at banding and voids. Figure 6.5 shows microstructural directionality along the rolling direction of Grade X-42 non-sour resistant steel longitudinal sample type "A" unexposed to HIC environment at a magnification of 320X, nital etched.

A metallographic sample was prepared for sample B'4 which is prepared transversely to the rolling direction of X-42 non-sour resistant carbon steel. Figure 6.6 is a micrograph of B'4 exposed to HIC at a magnification of 200X. As shown in Figure 6.6, banding of the microstructure is insignificant. This insignificance is expected, since "B" type samples are prepared transversely to the rolling direction of the steel, while banding is formed longitudinally to the rolling direction of steel, as shown on type "A" samples.

Figure 6.7 presents a metallograph of a transverse section of sample A' 22, which is prepared along the rolling direction of Grade X-42 steel at a magnification of 16X, nital etched. The samples prepared along the rolling direction of the steel experienced severe HIC damage. This is compatible with the fatigue testing results, which showed that the samples prepared along the rolling direction had a lower fatigue strength than the samples prepared transversely to the rolling direction.

Figure 6.8 presents a photomicrograph of a transverse section of sample B' 22, which is prepared transversely to the rolling direction of Grade X-42 steel. No significant HIC damage was found in the sample. Figure 6.9 presents another transverse section that was taken five millimeters away from the sample in Figure 6.8. Figure 6.10 presents a sample taken 10 millimeters away from the sample in Figure 6.8. None of the samples of B'22 did exhibited HIC damage. These metallographic findings are compatible with the fatigue test results, which showed that the samples prepared transversely to the rolling direction have a better fatigue life than the samples prepared along the rolling direction.

Figure 6.11 is a metallographic section prepared from sample C'6 which was exposed to HIC and then tested for fatigue. "C" type samples are made of carbon steel grade X-60 non-sour resistant along the rolling direction. Figures 6.12 and 6.13 are higher-magnification photographs of sample C'6. The fracture surface started flat and then it propagated in a slant manner at an approximately 45° angle. The central HIC crack intercepted the fatigue fracture surface.

Figure 6.14 is a micrograph of C'6 at a magnification of 125X and it shows that HIC cracking initiated at banding and voids along the rolling direction. Examination of the fatigue fracture HIC crack area on the slant section under higher magnification revealed gross grain elongation and microstructural deformation, as shown in Figure 6.15. The microstructural deformation suggests that the slant section experienced yielding due to final fracture overloading. As shown in Figure 6.16, at a magnification of X320, along the banding, the microstructure of sample C'6 was un-deformed with HIC crack initiating away from the fracture.

The other half of the sample C'6 fracture surface was sectioned, cleaned by ultrasonic, and prepared for scanning electron microscope (SEM) examination. Figure 6.17 presents an SEM photograph taken near the crack origin at the flat surface of the fracture. The flat area of the fracture surface was brittle. SEM examination of the slant area of the fracture surface revealed the presence of ductile dimples, which indicates that failure took place by yielding due to final tensile overload, Figure 6.18.

SEM and metallographic findings for sample C'6 were in agreement regarding the nature of crack morphology. Metallographic examination of the flat area revealed a transgranular mode of cracking with undeformed microstructure; while SEM results revealed the presence of quasi-cleavage indicating a brittle type of failure. The microstructure of the slant area was stretched and elongated, due to overloading, which is in agreement with the dimples observed by the SEM examination.

Figures 6.19, 6.20 and 6.21 are photomicrographs of sample C'2 and they show lamination at the center of the sample. As indicated by the photographs, HIC cracking initiated at the lamination. There was no indication of HIC damage initiation away from the lamination center, as shown in Figure 6.22.

A metallographic section was prepared from sample D'8, which was exposed to HIC and then fatigue-tested, for microstructural examination. "D" type samples were prepared transversely to the rolling direction of grade X-60 sour resistant carbon steel. Figure 6.23 is a micrograph showing the microstructure of sample D'8 at a magnification of 500X, nital etched. The grains were relatively small in size, since the sample is transverse to the rolling direction. The grains were equiaxed without banding or directionality in the microstructure.

One of the fractured sections of sample E'1 was split longitudinally and mounted for metallographic examination. "E" samples were prepared longitudinally to the rolling

direction of grade X-60 sour resistant carbon steel. Figure 6.24 shows a metallograph of sample E'1 which was exposed to HIC and tested for fatigue. The fracture surface consists of a flat region and a slant area.

Figure 6.25 shows the microstructure of the flat fracture of sample E'1 at a magnification of 1000X, nital etched. The crack morphology is transgranular with un-deformed microstructure. The microstructure is clean and it contains no voids, lamination or banding.

Figure 6.26 presents the microstructure of the slant fracture of sample E'1 at a magnification of 1000X, nital etched. As shown in the micrograph, the microstructure experienced deformation and grossgrain elongation. The findings of the fracture surface distinguished regions of sample E'1 are similar to sample C'6, although both samples differ in their chemistry.

Examination of the fracture surface of sample C'1 by using the SEM revealed that near the beginning of the flat fracture indications exhibited brittle fracture while the slant fracture showed evidence of shear dimples due to final tensile overloading, Figures 6.27 and 6.28.

Although samples C'1, E'1 and C'6 were fatigue-tested at different load levels, the samples showed similar crack initiation and propagation behaviors by exhibiting two distinctive regions; (1) brittle flat fracture and (2) ductile slant fracture.

Crack length ratio measurements confirmed that HIC cracks prefer to propagate along the rolling direction of the steel due to the presence of voids, banding and lamination along the given direction. Metallographic examination of samples from different steel grades confirmed that HIC cracking initiated at banding and voids, which is in conformance with the findings concluded by the crack length ratio measurements.

SEM examination was also performed on the fracture surface of sample A'21 which was prepared from Grade X-42 non-sour resistant steel longitudinally to the rolling direction and exposed to HIC. Figure 6.29 presents a general SEM view of the fracture surface of A'21 at a magnification of 25X. The area marked with the letter A in Figure 6.29 was relatively flat, and it presents the initiation site for the fracture surface.

Figures 6.30, 6.31, 6.32 and 6.33 are higher magnifications of area A that was shown in Figure 6.29. Radial lines converged to the initiation site of the fracture surface, which is a microscopic blister. Secondary cracking was also observed on the initiation site of the fracture. Figure 6.34 presents the microscopic blister at the initiation site of the fracture surface, which was identified in Figure 6.30 at a magnification of 2000X. Fatigue striations were observed at the fracture initiation site, at a magnification of 7500X as shown in Figure 6.35.

Figures 6.36 and 6.37 are higher SEM magnifications (1000X and 1500X) of the secondary crack that was located on the initiation site of the fracture surface. Fine

fatigue striations were observed near the crack, as shown in Figure 6.38 at a magnification of 7500X.

Figure 6.39 presents an SEM micrograph at a magnification of 5000X near the crack tip of area A in Figure 6.29 and it shows fatigue striations.

Figure 6.40 is an SEM micrograph at a magnification of 1000X of area A in figure 6.29, and itshows a brittle type of fracture. Blisters were observed also between area B and C of Figure 6.29 as shown in Figure 6.41 at a magnification of 2000X. Generally area C of Figure 6.29 showed a mix zone of brittle fracture accompanied by shear dimples, as illustrated in Figure 6.42 at a magnification of 2000X. Areas D, E, and the rest of the fracture surface in Figure 6.29, showed shear dimples, indicative of overloading as illustrated in Figures 6.43 and 6.44.

Figure 6.45 is a general SEM view of the fracture surface of sample A17 at a magnification of 15X. Sample A17 was prepared from Grade X-42 non-sour resistant steel longitudinally to the rolling direction of the plate unexposed to HIC. The area marked A in Figure 6.45 shows a flat fracture surface, indicative of brittle failure. SEM examination of the fracture initiation site at higher magnification showed that radial lines converged to the fracture initiation site, as illustrated in Figures 6.46, 6.47, 6.48, 6.49, 6.50 and 6.51. The fracture initiated due to mechanical fatigue as shown in the fractographs. Figure 6.52 exhibits a brittle type of fracture at the initiation site with indications of quasi-cleavage. Examination of the brittle fracture at the initiation site of

area A in Figure 6.45 revealed the presence of fatigue striations, as shown in Figure 6.53 at a magnification of 7500X.

SEM examination of area B in Figure 6.44 revealed the beginning of a mix zone of both brittle fracture and shear dimples. Figure 6.54 presents a photograph of the mix zone of the brittle fracture with dimples, at a magnification of 2000X.

Under SEM examination, Area C of Figure 6.45 exhibited pure dimples due to overloading as shown in Figure 6.55 at a magnification of 2000X. In general there were no secondary cracks at the initiation site of the fracture surface of sample A17.

SEM examination of the fracture surfaces of samples A'21 and A17 clearly showed that exposure to HIC introduced secondary cracking and microscopic blisters that interacted with the fatigue cracks to accelerate the fracture. The fracture surface of A'21 initiated at a microscopic blister. Also samples exposed to HIC showed through thickness blisters that contributed to the fracture mechanism.

Chapter 7

7. DISCUSSION

7.1 Performance of Samples in NACE Solution

NACE TM0284-2003 solution A was used for hydrogen exposure which provides a very corrosive environment that has tremendous hydrogen charging ability at room temperature. Samples prepared longitudinally and transversely to the rolling direction of plates from API-5L Grade X-42 non-sour resistant, X-60 non-sour resistant and X-60 sour resistant carbon steel were exposed to hydrogen in accordance with NACE TM0284-A-2003.

The driving force for hydrogen blistering and stepwise cracking is the hydrogen migrating into the steel as a result of proton discharge at the surface during the following corrosion reaction:

$$Fe + H_2S \Leftrightarrow FeS + 2H^{O}$$

Hydrogen diffusion to inclusions in the matrix occurs because of the presence of residual stress at the inclusion/matrix interface caused by shrinkage and rolling. Also initial micro-cavities are present at the inclusion/matrix interface. Hydrogen atoms accumulate at low-strain-energy sites to form molecular hydrogen gas at high pressure.

The driving force for blistering and step-wise cracking is the pressure build-up to 10^5 atmospheres, caused by the formation of molecular hydrogen at trap sites.

In comparison, the effect of rolling direction on cracking was remarkable. The average CLR of the tested specimens varied significantly between the samples prepared along the rolling direction and the samples prepared transversely to the rolling direction. As shown in table 5.1, the CLR was reduced from 23% for an A' sample to 8% for a B' sample. Type "B" samples were prepared transversely to the rolling direction of Grade X-42 non-sour resistant carbon steel; while "A" samples were prepared along the rolling direction of the same steel.

The CLR was reduced from 19.5% for a C' sample to 1.93% for an F' sample. "C" samples were prepared longitudinally to the rolling direction of grade X-60 non-sour resistant carbon steel; while "F" samples were prepared transversely to the rolling direction of the same steel. The relationship between the variations in the CLR with the orientation of the rolling direction to the geometry of the sample suggested that HIC cracks prefer to propagate along the rolling direction of the steel, due to the presence of hydrogen trap sites, the elongated MnS inclusions, banding and lamination along the direction.

Samples type D' and E' did not develop HIC cracking, since they were prepared from sections longitudinal and transverse, respectively, to the rolling direction of grade X-60 sour resistant carbon steel. The designation of sour resistance is applied to conventional

steels that are fabricated in the normalized condition, but contain ≤ 0.002% sulfur and calcium addition.

7.2 Performance of Samples under Mechanical Fatigue Testing

As shown in Figure 4.13, the S-N curves of (A-A') samples in the HIC exposed and unexposed conditions showed that the unexposed samples have a better fatigue life than the exposed samples. The reduction in σ_a between the two σ_a-N curves, at 10^5 cycles with high stress amplitude, is around 10.1%; while the reduction in the fatigue life at a σ_a of 210 MPa is by an order of magnitude of 9. At a low stress value, the reduction in σ_a averaged 5.6%, at 10^6 cycles; while the reduction in the fatigue life was by a magnitude order of 6 at σ_a of 175 MPa. Samples A and A' were machined along the rolling direction of Grade B X-42 non-sour resistant steel. The difference between the two S-N curves in the number of cycles to failure is reduced as the load value for testing is reduced. The decrease in difference between the two S-N curves with the reduction of load value is credited to steel degradation by hydrogen embrittlement. The damage mechanism for the steel that is embrittled by hydrogen charging under the application of high load values consists of three factors; (1) Brittle fracture due to hydrogen embrittlement, (2) Fatigue, and (3) HIC cracks. As the load value is reduced for testing, the influence of hydrogen embrittlement is reduced, and therefore the primary factors affecting the fracture mechanisms are (1) Fatigue, and (2) Existing HIC cracks.

B and B' type samples were made transversely to the rolling direction of Grade B X-42 non-sour resistant carbon steel. The graphs of the S-N curves for (B-B') samples that were plotted in Figure 4.14 showed that samples unexposed to HIC have a better fatigue life than exposed samples. The reduction in fatigue strength at 10^5 cycles for high stress values averaged 5.9%; while the reduction in the fatigue life at σ_a of 210 MPa was by an order of magnitude of 5. For low stress values, at 2.5 X 10^6 cycles, the reduction in stress amplitude averaged 2.7%; while the reduction in fatigue life was approximately by an order of magnitude of 2 at σ_a (equals 175 MPa). At high load values, the factors influencing fracture for samples exposed to HIC are as follows: (1) hydrogen embitterment of steel, (2) fatigue, and (3) HIC cracks. As the load value for testing is reduced, the effect of embrittlement becomes insignificant, since it depends on stress and therefore the factors affecting the fracture become (1) fatigue and (2) HIC cracks. As shown in metallographic examination and table 5.1 of the crack length ratio, HIC cracks prefer to propagate along the rolling direction more than transverse in the direction. Therefore, the effects of HIC cracks transverse to the rolling direction as in samples type "B" are reduced. This explains the reduction in difference between the two S-N curves of HIC exposed and unexposed conditions in the number of cycles to failure as the load value for testing is reduced, as shown in Figure 4.14.

The difference between the two S-N curves (exposed to HIC and unexposed to hydrogen charging) of (B-B') samples was less than the difference between the two S-N curves of "A" samples. The reduction in difference between the two S-N curves of "B"

samples in comparison to “A” samples is attributed to the CLR value that is higher in samples type “A” than samples type “B”, which is relevant to the formation of HIC cracks along the rolling direction.

The S-N curves for “A” samples in comparison to “B” samples in the unexposed condition showed that “B” samples have a slightly better fatigue life than “A” samples, as shown in Figure 4.19. The difference in fatigue life is attributed to the grain size of samples and the presence of banding and sulfide stringers along the rolling direction of the steel. Metallographic examination showed that the grains of “B” samples are smaller than the grains of “A” samples. Smaller grain size gives more resistance to fatigue crack propagation. Therefore, the mechanical properties of the steel plate depend on direction.

The S-N curves of (A’) and (B’) specimen, after being exposed to HIC testing, showed that the fatigue life of (B’) samples is superior to (A’) samples, Figure 4.20. The difference in fatigue life is attributed to the difference in CLR of both sample types and to the change in grain sizes. The higher CLR in “A” samples indicates that the samples contain more step-wise cracks which provide a shorter fatigue life. Also the orientation of the specimen, when prepared in relation with the rolling direction and the diameter size, influenced the entrapment of atomic hydrogen inside the steel to form stepwise cracks.

The S-N curves of (C-C') samples (exposed and unexposed to HIC) showed that the unexposed specimen had a slightly better fatigue life than the exposed samples, Figure 4.15. The reduction in fatigue life with samples exposed to HIC is attributed to the formation of stepwise cracks and to hydrogen embrittlement of the steel. Samples C and C' were prepared longitudinally to the rolling direction of Grade B X-60 non-sour resistant carbon steel plate.

The S-N curves of both hydrogen-charged and un-charged (F-F') samples, that were prepared transversely to the rolling direction of Grade B X-60 non-sour resistant steel plate, showed that the fatigue life of unexposed samples is better than the life of exposed samples, Figure 4.18. The difference between the two S-N curves is quite low for (F-F') samples. This low difference is quite similar to the difference between the S-N curves of (C-C').

The S-N curve of "C" samples was compared with the S-N curve of "F" samples for the unexposed condition of both sample types, Figure 4.21. The graph shows that "F" samples, prepared transverse to the rolllying direction of Grade B X-60 non-sour resistance steel plate, have a better fatigue life than "C" samples prepared from longitudinal sections of the same steel plate. Metallographic examination showed that the grains of "F" samples were smaller than those of "C" samples. The smaller grain size suggests more resistance to crack propagation and hence a change of mechanical properties of the steel plate with direction.

F’ samples exposed to HIC were compared to C’ samples exposed to HIC, Figure 4.22. The graph of the S-N curves showed that F’ samples have a better fatigue life than C’ samples. This difference in fatigue life is because C’ samples have a higher CLR than F’ samples due to the tendency of stepwise cracking to form along the rolling direction of the steel. Also F’ samples have smaller grains size than C’ samples, which makes them more resistant to crack propagation. The findings of Figure 4.22 were compatible with the results of Figures 4.19, 4.20 and 4.21.

The S-N curves of HIC exposed and unexposed samples that were prepared from Grade B X-60 sour resistant steel plate did not reveal significant variation in fatigue life versus stress. The insignificant variation between the two S-N curves is because the steel is HIC resistant.

7.3 Microstructural and Fractographic Characteristics

Metallographic examination of hydrogen-exposed specimens showed that the HIC cracks are created parallel to the rolling direction of the steel plate without the effect of external applied stress. Carbide precipitation in steel has a significant effect on hydrogen uptake. The carbide interface has a large binding energy with hydrogen, and it acts as a trap site. Elongated MnS inclusions act as initiation sites for cracking. The nonmetallic inclusions are short, and they have different depths across the thickness of the steel, which causes the HIC to follow a stepwise cracking mode.

As shown in the metallographs of Grade X-60 HIC resistant steel, microstructure homogenization, elimination of inclusions and reduction of sulfur content improved HIC resistance in line pipe steels. Homogenization of microstructure can be achieved by reducing carbon content and by quenching and tempering.

Microscopic examination of the microstructures of samples, prepared longitudinally and transversely to the rolling direction of steel plates, showed that elongated inclusions are formed longitudinally to the rolling direction of steel plates as shown on "A" samples in comparison to "B" samples. Elongated inclusions were relatively less significant in samples prepared transversely to the rolling direction of the steel.

For most of the fatigue tested specimens, fatigue fracture started flat but then it propagated in a slant manner at an approximately 45° angle. Microscopic examination of the flat area revealed a transgranular mode of cracking with undeformed microstructure; while SEM results revealed the presence of cleavage indicating a brittle type of failure. The microstructure of the slant section revealed gross grain elongation and deformation. The microstructural deformation suggests that the slant section experienced yielding due to final fracture overloading. Away from the fracture, the microstructure was un-deformed. SEM examination of the fracture surface of the slant area revealed the presence of ductile dimples, which indicates that failure took place by yielding due to final tensile overload.

SEM examination of the fracture surfaces of samples exposed and unexposed to HIC, such as A'21 and A17, clearly showed that exposure to HIC introduced secondary

cracking and microscopic blisters that interacted with fatigue to accelerate the fracture. Samples unexposed to HIC envirnoment failed due to fatigue fracture.

The fracture surface of A'21 which was exposed to HIC initiated at a microscopic blister that acted as a stress raiser. Samples exposed to HIC showed through thickness blisters that contributed to fracture.

Chapter 8

8. CONCLUSIONS

1. Non HIC resistant steel samples were found to be very susceptible to HIC blistering and step-wise cracking in the standard NACE TM0284-A-96 solution at 25 ^{o}C.

2. Metallographic examination revealed that HIC cracks initiated at elongated inclusions, banding and impurities that acted as entrapments for atomic hydrogen to form molecular hydrogen inside the steel.

3. Non HIC resistant steel samples, in the HIC exposed and unexposed conditions, showed that the unexposed samples have better fatigue lives than the exposed samples.

4. From the crack length ratio, it was observed that HIC cracks prefer to propagate along the rolling direction of the steel rather than transversely to the rolling direction of the steel.

5. HIC exposed samples, that were prepared transversely to the rolling direction of both X-42 and X-60 non-sour resistant steel plates, were found to have a better fatigue life than HIC exposed samples that were prepared longitudinally to the rolling direction of the same steel plates. This difference in fatigue life is attributed to the samples being prepared longitudinally to the rolling direction of

the plates, which have a higher CLR than transverse samples due to the tendency of stepwise cracking to form along the rolling direction of the steel.

6. The S-N curves of transverse samples (exposed and non-exposed to HIC), of both X-42 and X-60 non-sour resistant steel plates, have less difference than the longitudinal samples. This is attributed to the CLR value which is higher in longitudinal samples than in transverse samples.
7. The fatigue life of HIC exposed samples that were prepared transversely to the rolling direction of both X-42 and X-60 non-sour resistant steel plates, was found to be superior to HIC exposed samples, prepared along the rolling direction of the same steel plates. This difference is attributed to the difference in CLR.
8. Metallographic examination confirmed that samples prepared along the rolling direction of the non-sour resistant steel experienced severe HIC damage; while samples prepared transversely to the rolling direction of the same steel plates had less HIC damage.

8.1 Future Work

The work done in this project aimed at studying the fatigue behavior of samples prepared longitudinally and transversely to the rolling direction of plates from API-5L Grade X-42 non-sour resistant, X-60 non-sour resistant and X-60 sour resistant carbon steel, when exposed to hydrogen in accordance with using NACE TM0284-A-2003. Future work may include the following:

1. In this project only hydrogen charging was used to simulate HIC damage, but in the actual service CO_2, oxygen and chloride are present in the natural gas streams in different concentrations. Other species such as CO_2, O_2 and Cl^- are not the sources of hydrogen, but their effects on HIC and fatigue life should be studied.
2. Pipelines are normally operated at different temperatures, depending on the hydrocarbon service that they are used for. The temperature influences the effect of hydrogen charging and entrapment in the steel, and hence it affects the HIC damage mechanism. The effect of temperature on HIC damage and fatigue life of pipelines should be investigated.

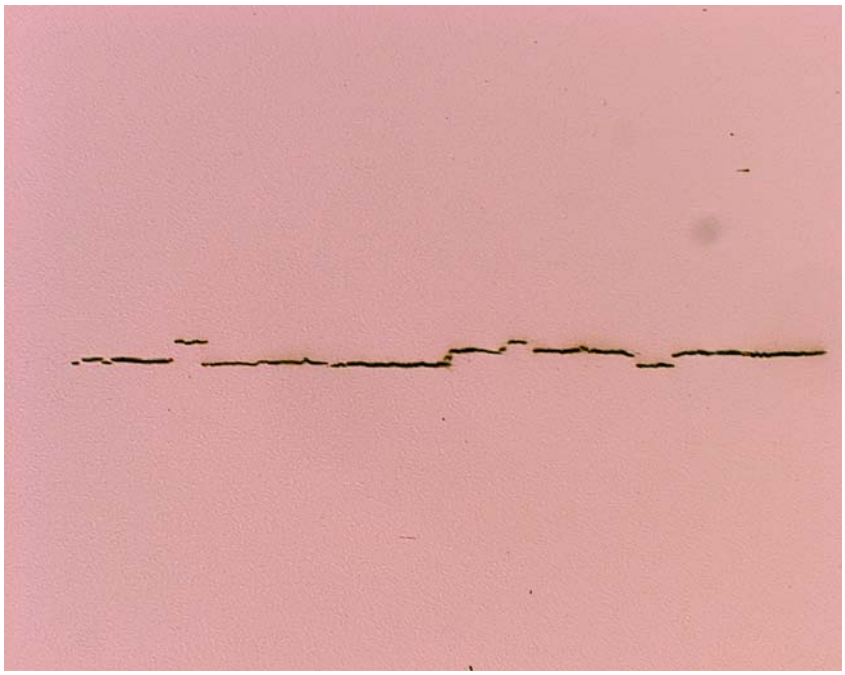

Figure 6.1: Optical microscope showing HIC crack on a metallographic section of Grade X-42 non-sour resistant steel along the rolling direction at 25X, unetched.

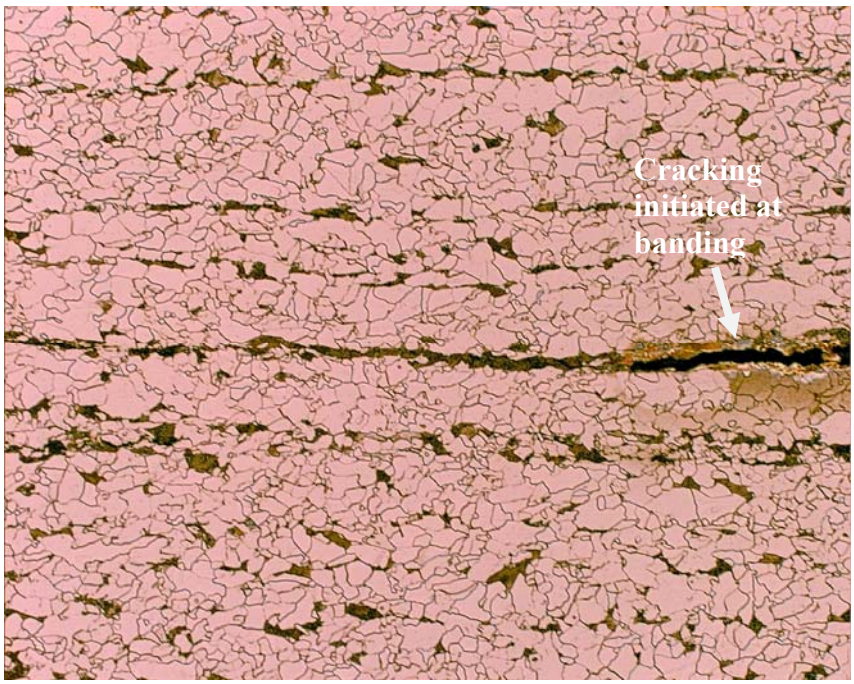

Figure 6.2: Microstructure of A'4 showing banding at 200X, nital etched. The micrograph shows HIC crack along banding.

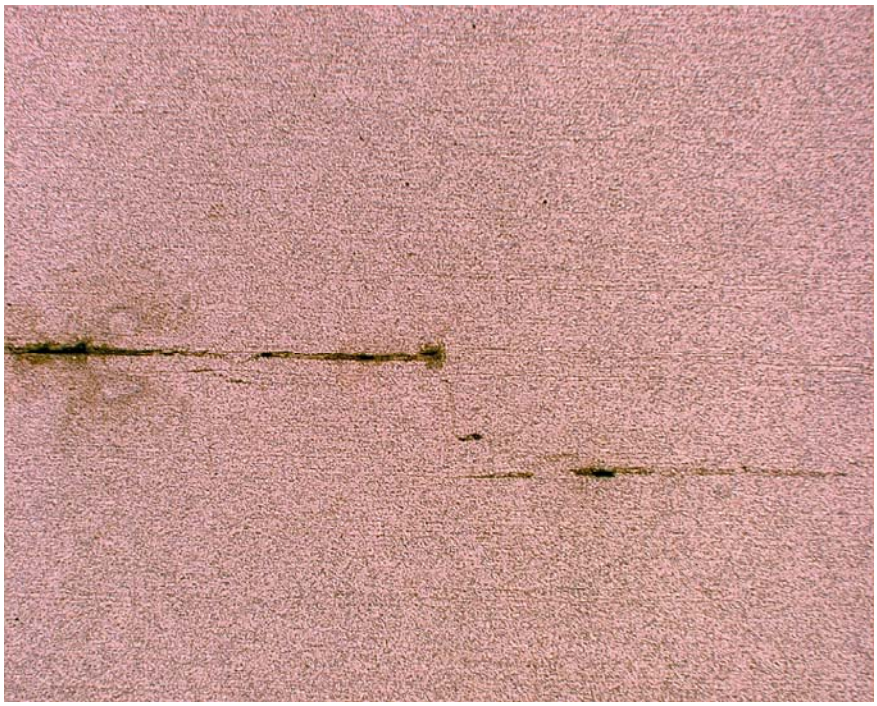

Figure 6.3: Metallographic section of sample A'6 showing step-wise cracking at 16X, nital etched.

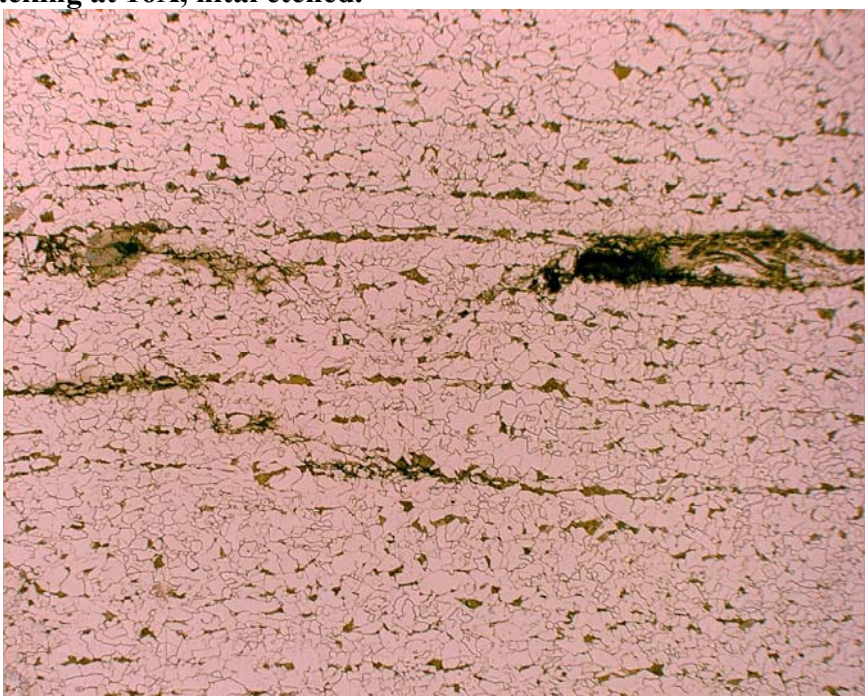

Figure 6.4: Micrograph of sample A'6 showing cracks initiating at voids and along the banding at a magnification of 125X, nital etched.

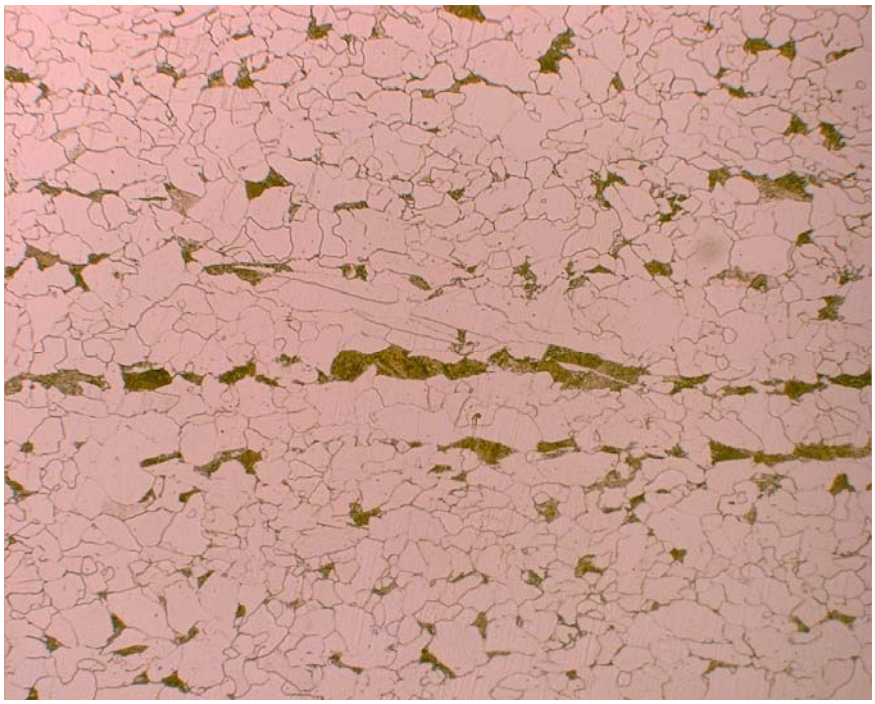

Figure 6.5: Microstructure of Grade X-42 steel type "A" sample unexposed to HIC environment with directionality along the rolling direction. 320X, nital etched.

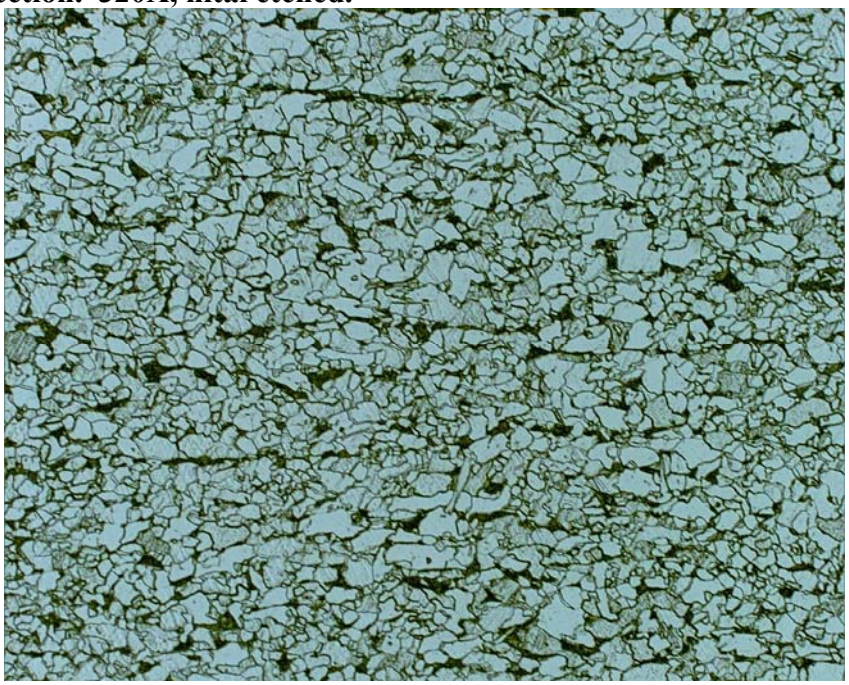

Figure 6.6: Micrograph of sample B'4, transverse to the rolling direction of Grade X-42 steel. 200X, nital etched.

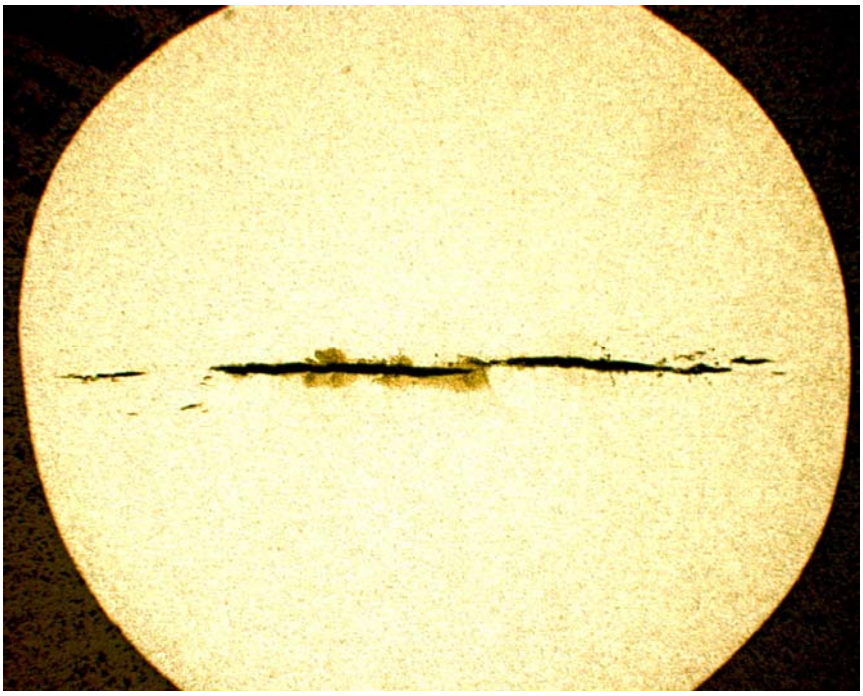

Figure 6.7: Transverse section of sample A' 22, which is along the rolling direction of Grade X-42 steel. 16X, nital etched.

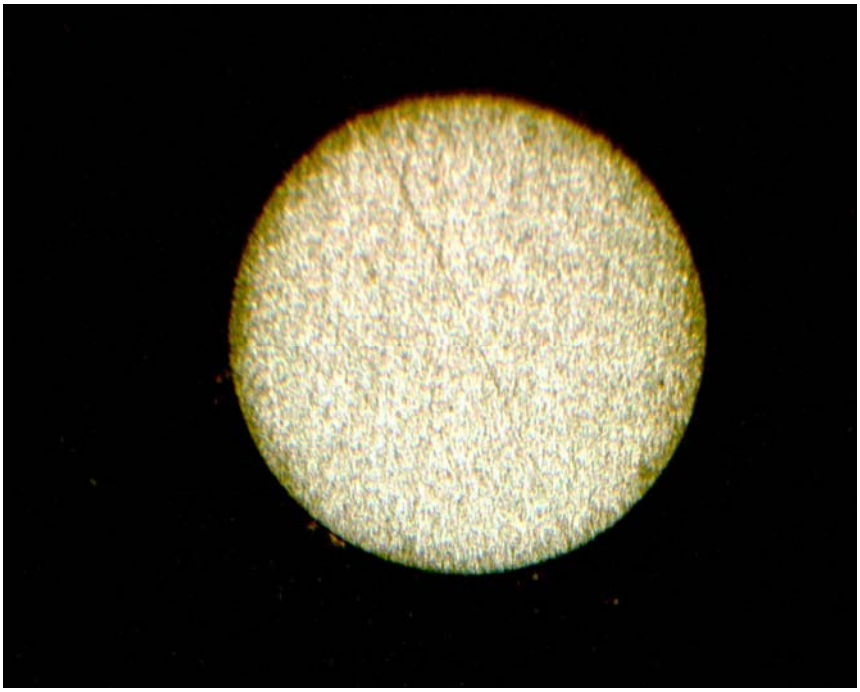

Figure 6.8: Transverse section of sample B' 22, transverse to the rolling direction of Grade X-42 steel.

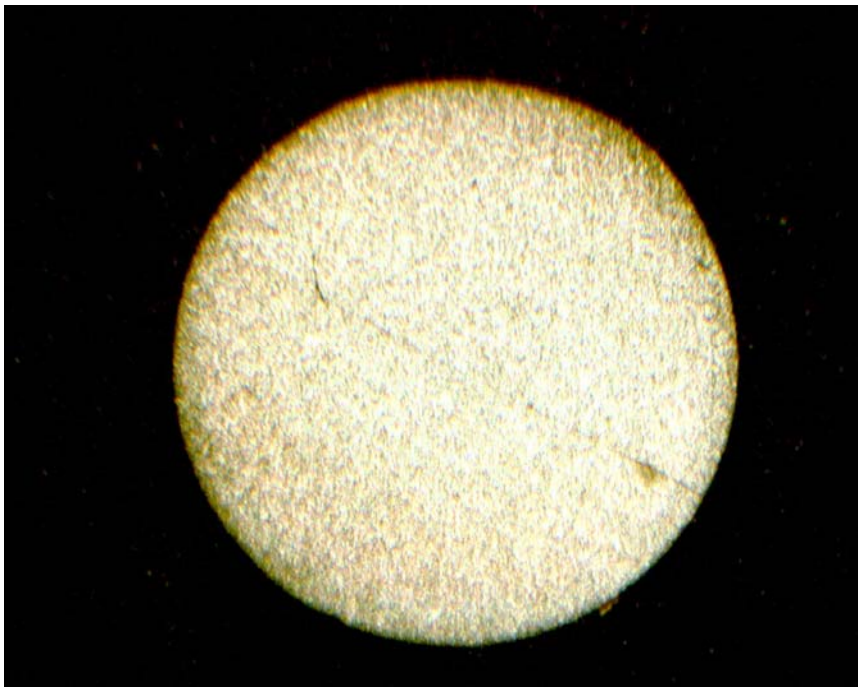

Figure 6.9: Transverse section of sample B' 22, taken 5 mm away from the section in Figure 6.8.

Figure 6.10: Transverse section of sample B' 22, taken 10 mm away from the section in Figure 6.8.

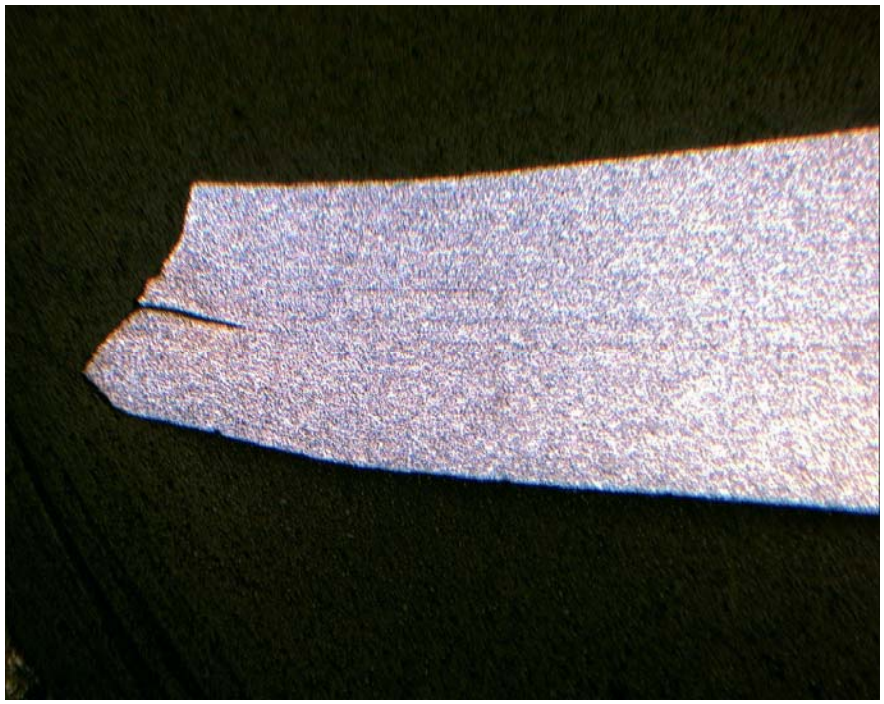

Figure 6.11: Metallograph of sample C'6 showing HIC cracking at a magnification of X5.4.

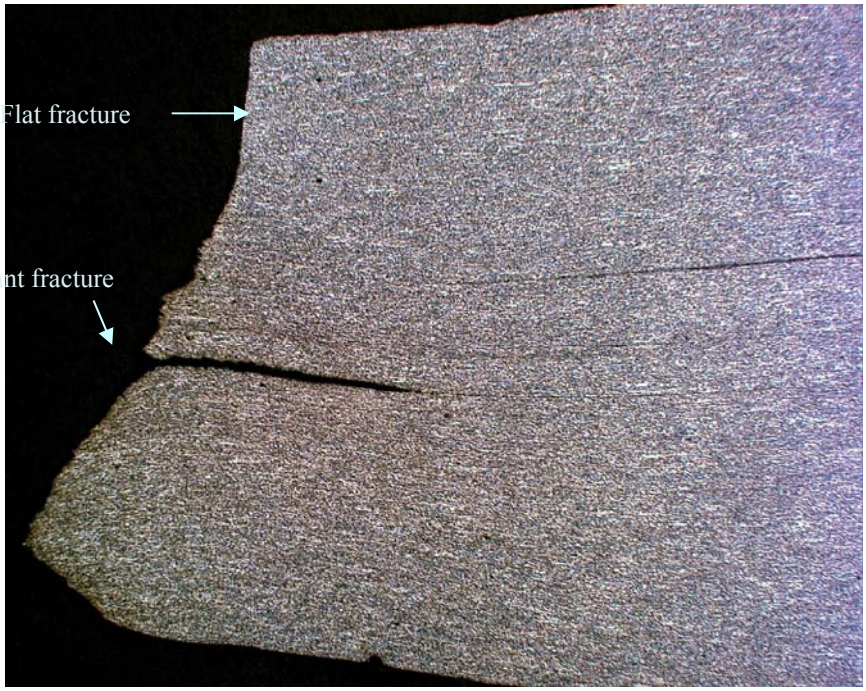

Figure 6.12: Metallograph of sample C'6 at X12.

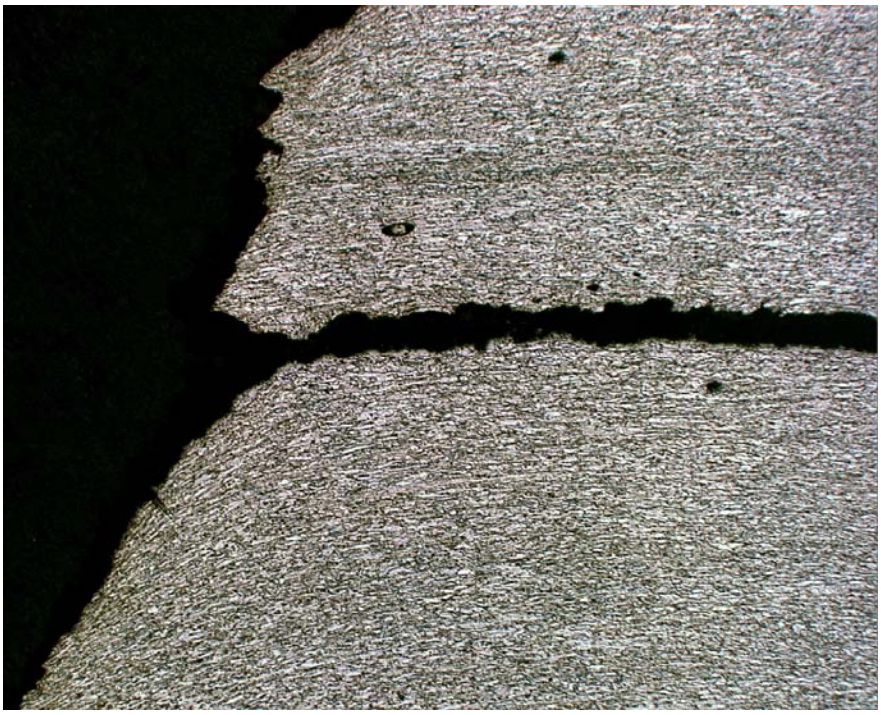

Figure 6.13: Micrograph of sample C'6 near the fracture surface at a magnification of X63, Nital etched.

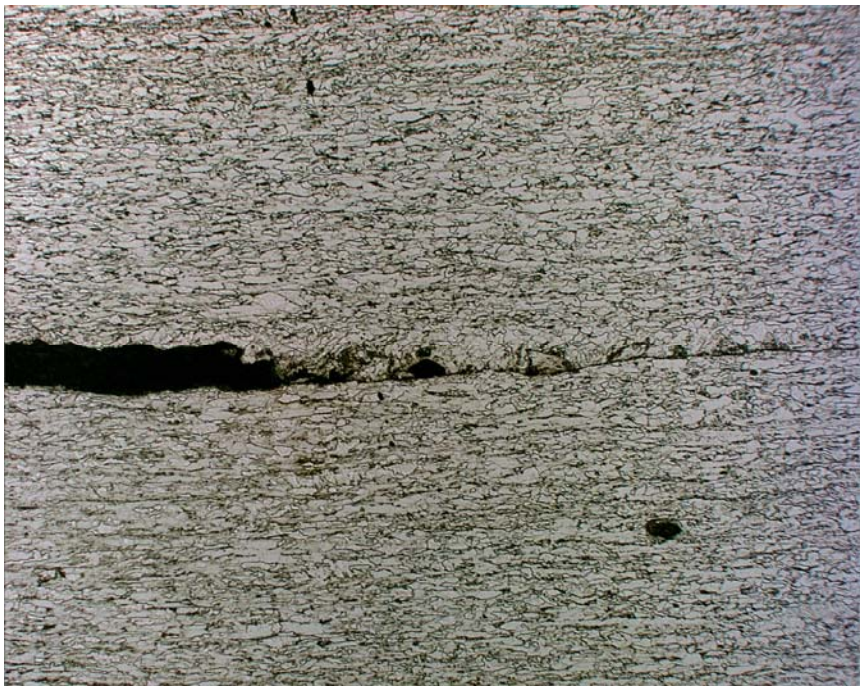

Figure 6.14: Micrograph of sample C'6 showing cracking along banding at a magnification of X125, nital etched.

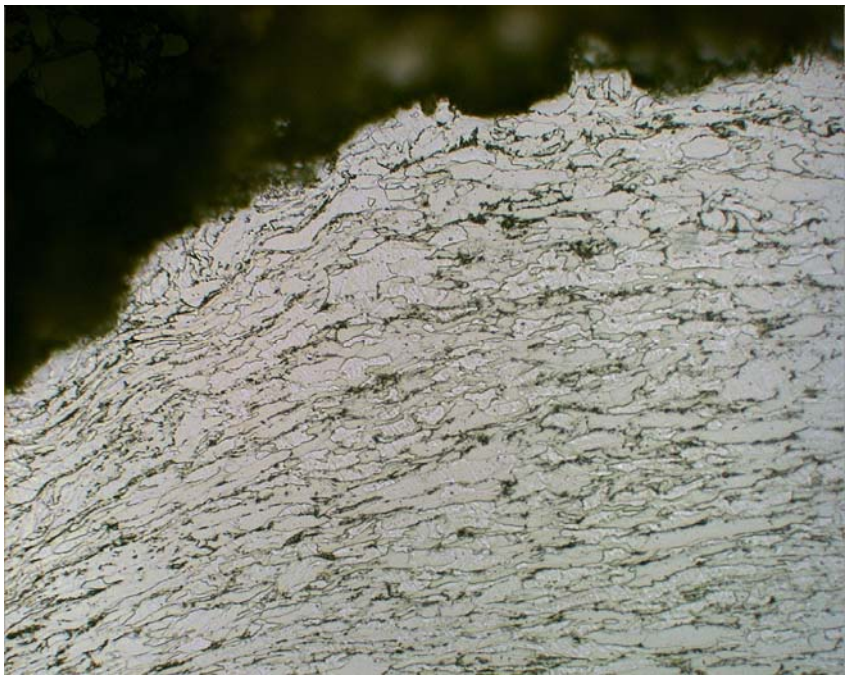

Figure 6.15: Micrograph of sample C'6 at a magnification of X320 showing deformation of the microstructure near the fracture.

Figure 6.16: Sample C'6 away from the fracture showing un-deformed microstructure with a crack initiating along banding, X320.

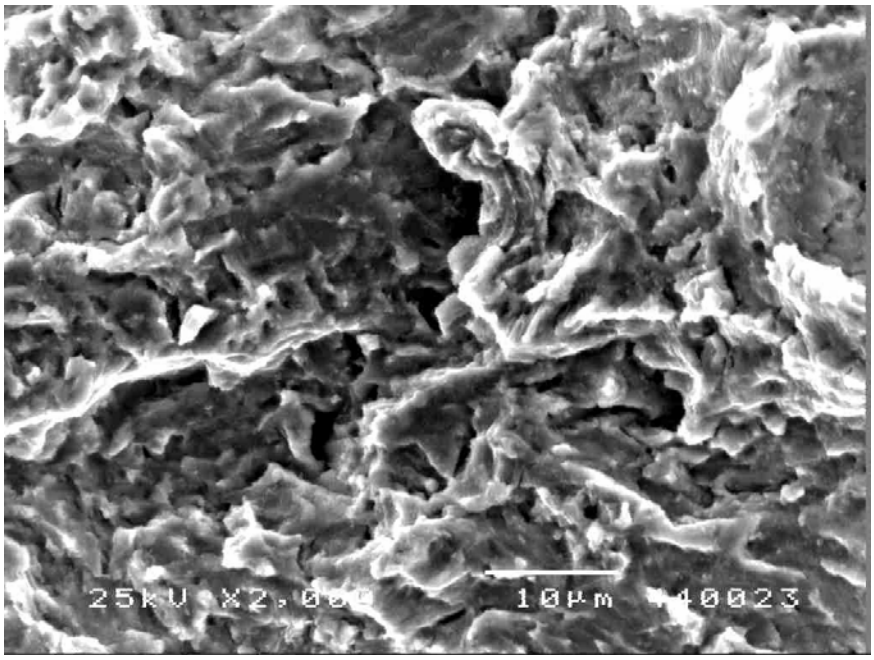

Figure 6.17: SEM photograph of the fracture face of sample C'6 taken at the flat surface showing brittle fracture, X2000.

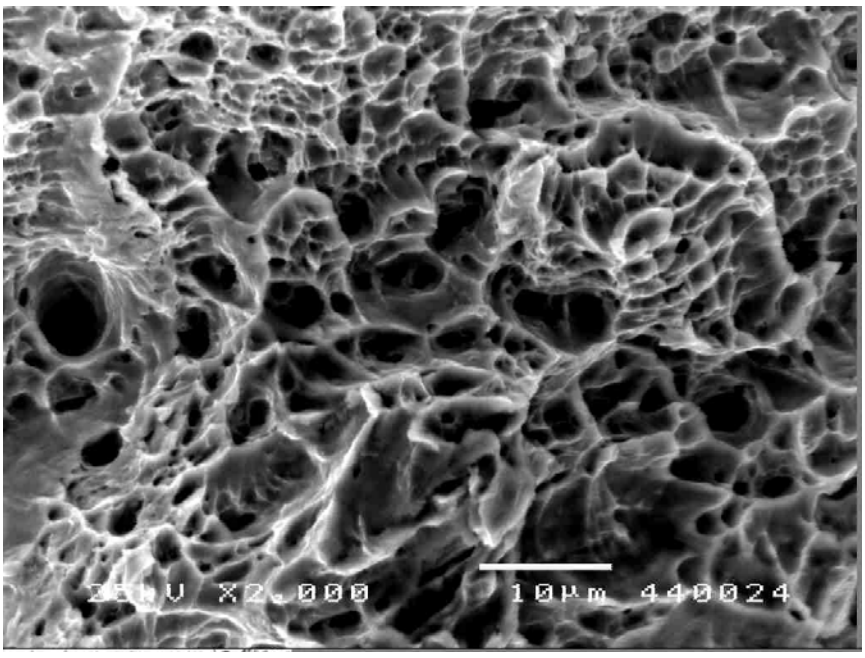

Figure 6.18: Fracture surface of sample C'6 taken at the slant area showing dimples which is indicate final tensile over load, X2000.

Figure 6.19: Micrograph showing the microstructure of sample C'2 with lamination at the center. Magnification 200X, nital etched.

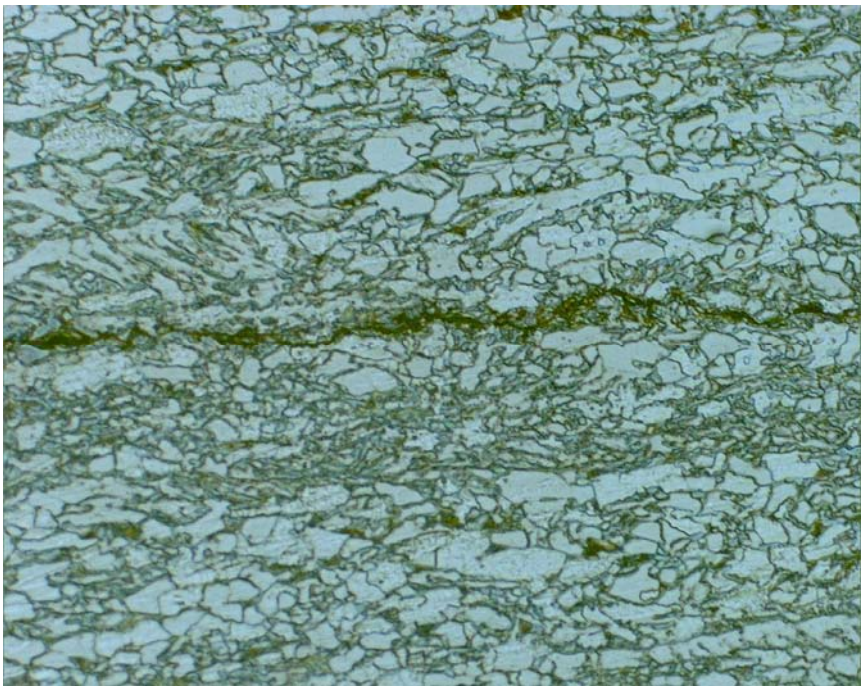

Figure 6.20: HIC cracking at the center of the microstructure of sample C'2 at a magnification of 500X, Nital etched.

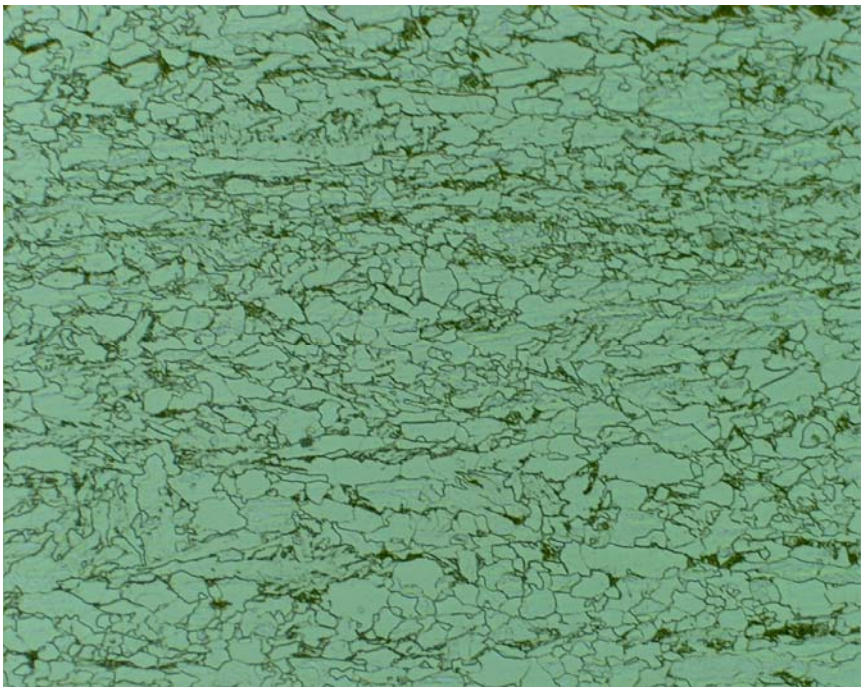

Figure 6.21: Micrograph showing the lamination at the center of sample C'2 microstructure. Magnification 500X, Nital etched.

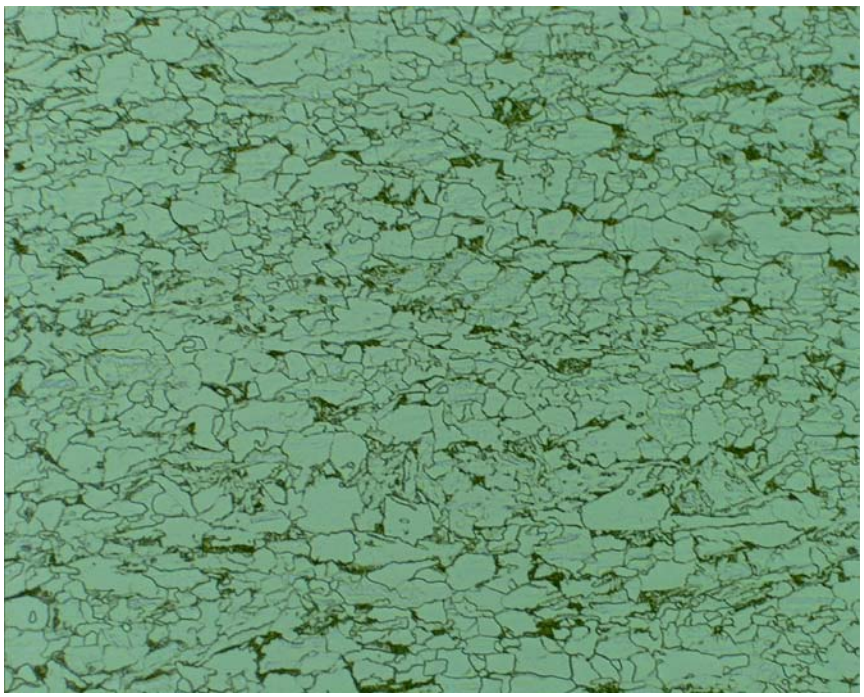

Figure 6.22: Micrograph showing the microstructure of sample C'2 away from lamination center. Magnification 500X, Nital etched.

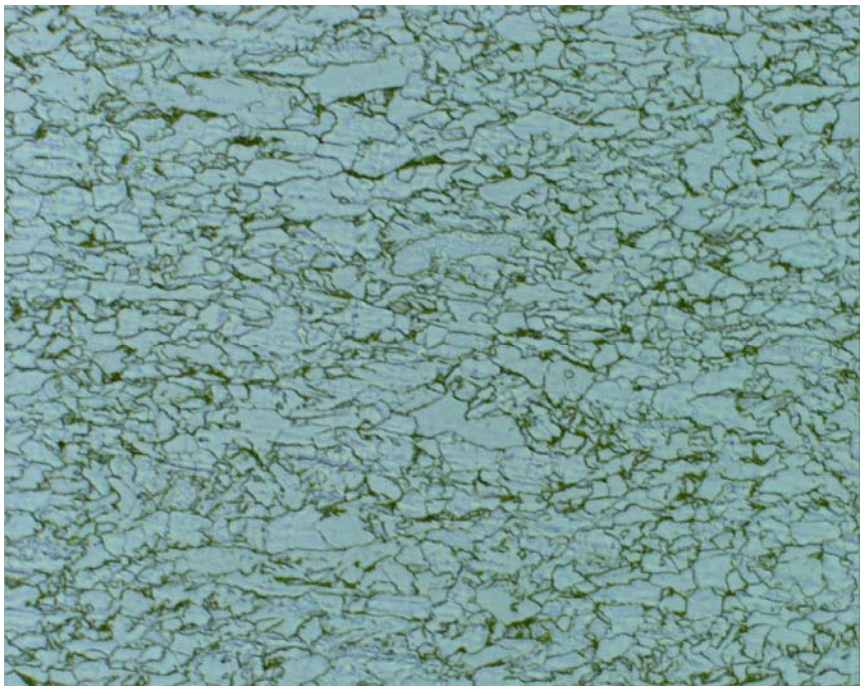

Figure 6.23: Microstructure of sample D'8 at a magnification of 500X, Nital etched.

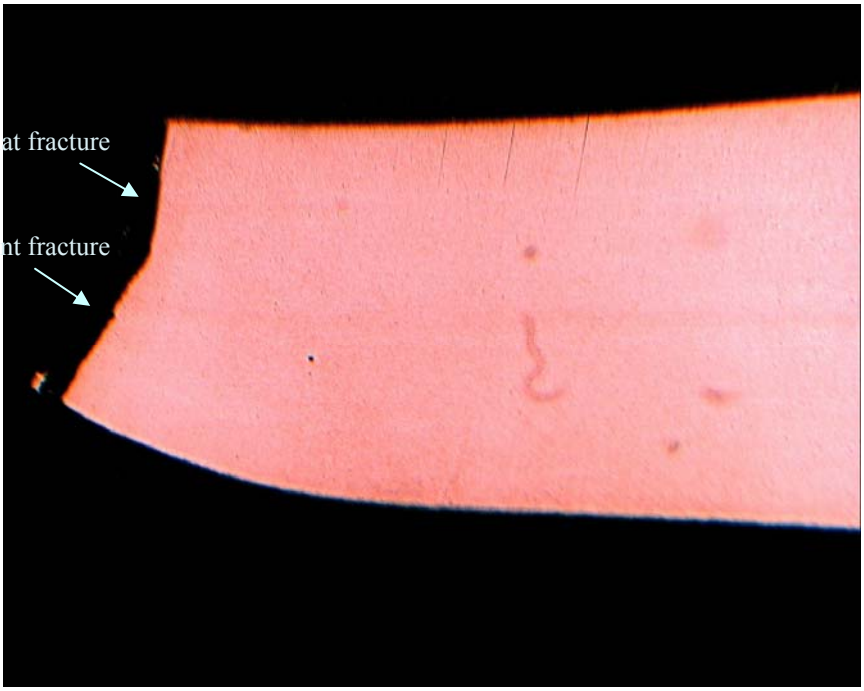

Figure 6.24: Metallograph of sample E'1 showing the flat area and slant section of the fracture face at a magnification of 8X, Nital etched.

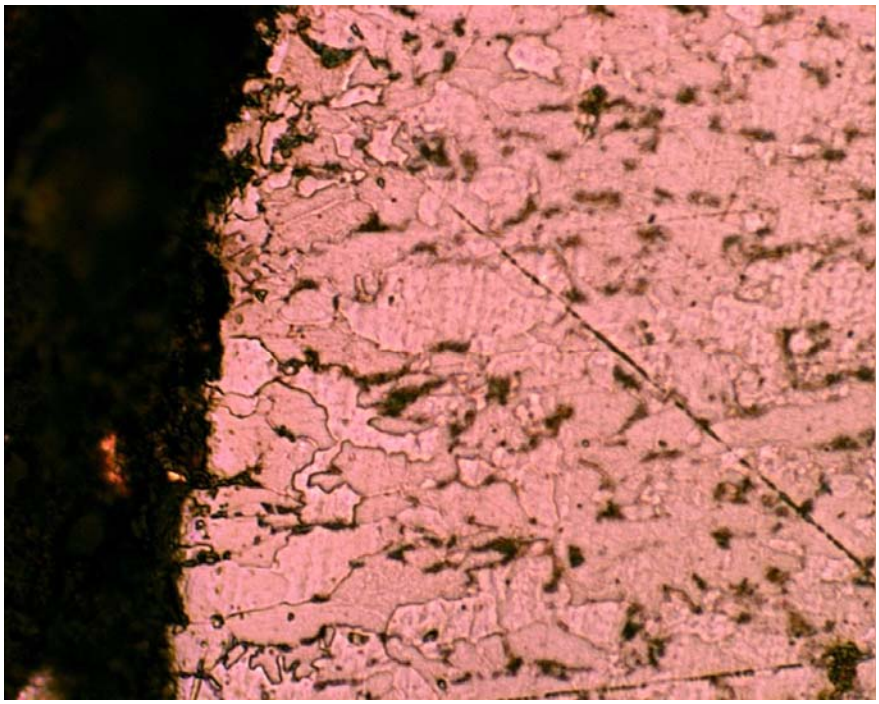

Figure 6.25: Micrograph of sample E'1 of the flat fracture area at a magnification of 1000X. The crack morphology is transgranular.

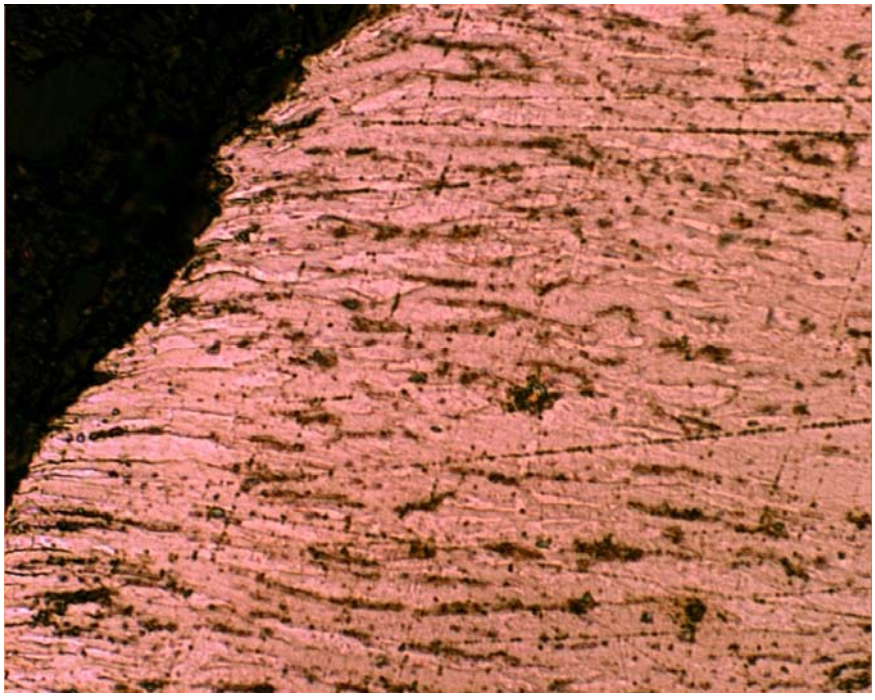

Figure 6.26: Micrograph showing the slant fracture area of Sample E'1, at 1000X, showing grain elongation.

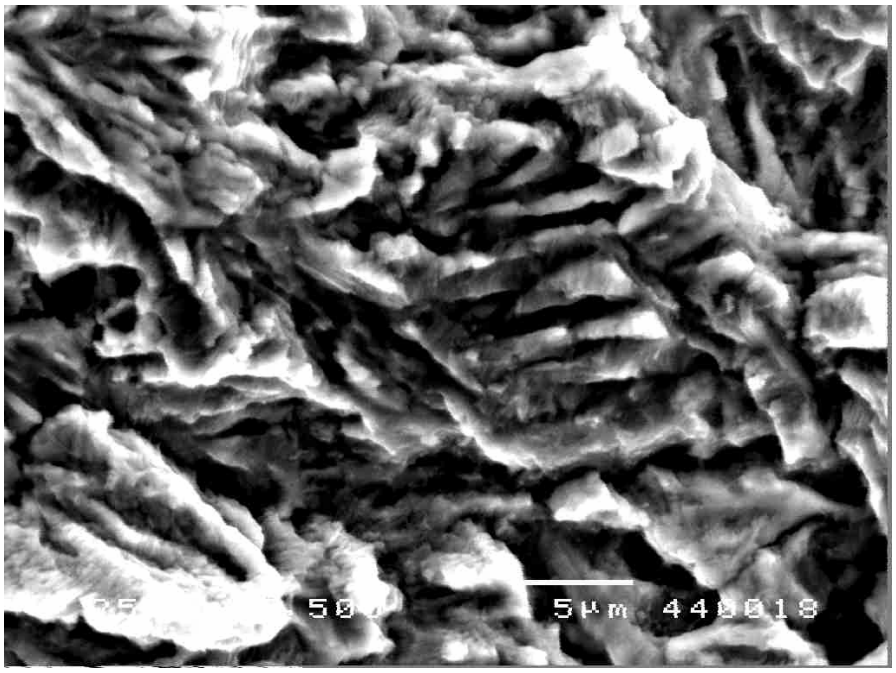

Figure 6.27: SEM photograph of the fracture face of sample C'1 near start of flat fracture showing brittle type of fracture.

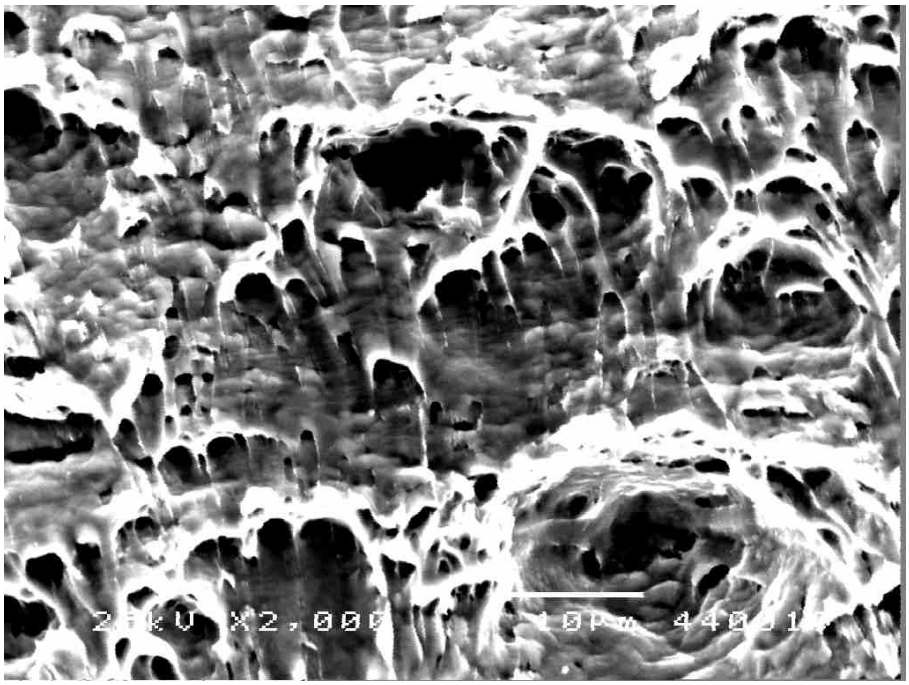

Figure 6.28: SEM photograph of the slant fracture of sample C'1, showing shear dimples due to final tensile overloading.

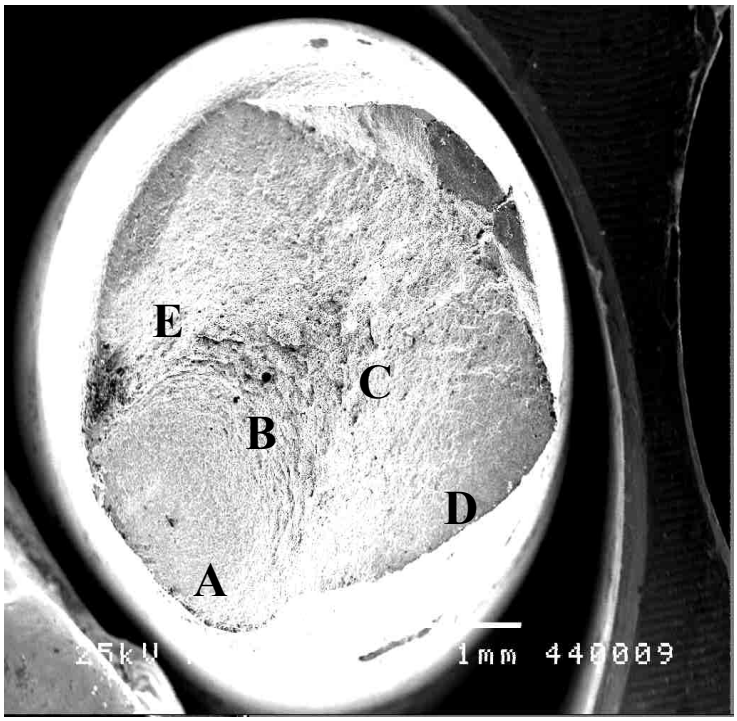

Figure 6.29: General SEM photograph of the fracture surface of sample A'21, exposed X-42 non-sour (L), at a magnification of 25X.

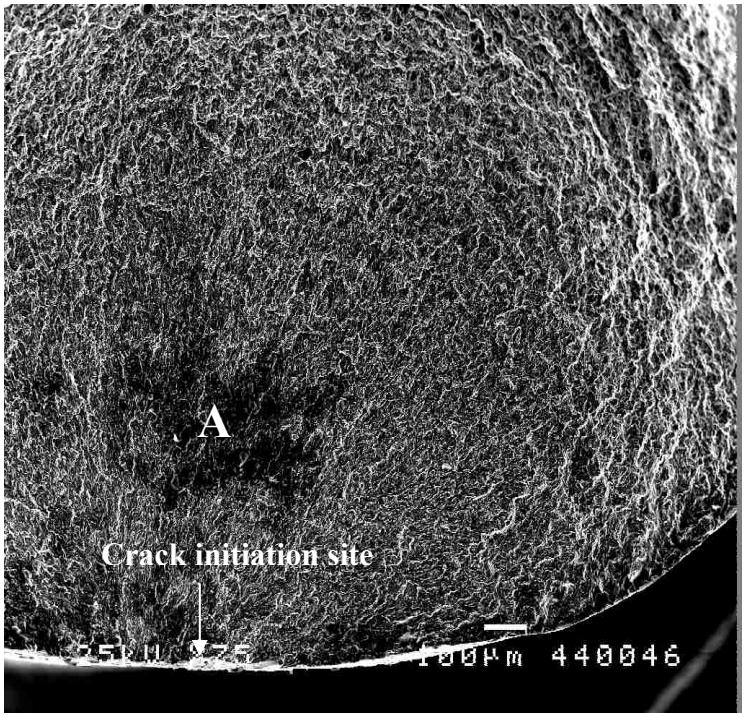

Figure 6.30: Fracture initiation site of area A in Figure 6.29 at 75X.

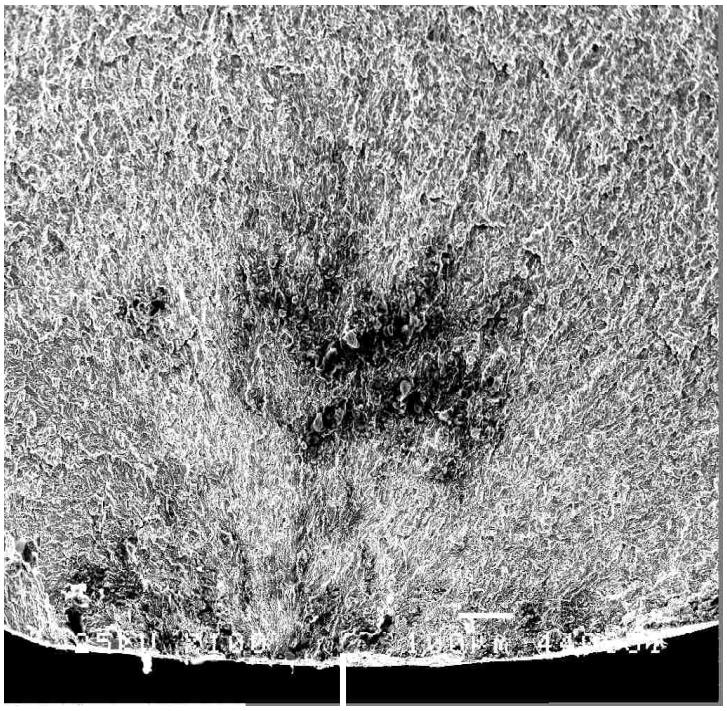

Figure 6.31: Fracture initiation site of area A in Figure 6.29 at 100X. Radial lines converge to the crack initiation site.

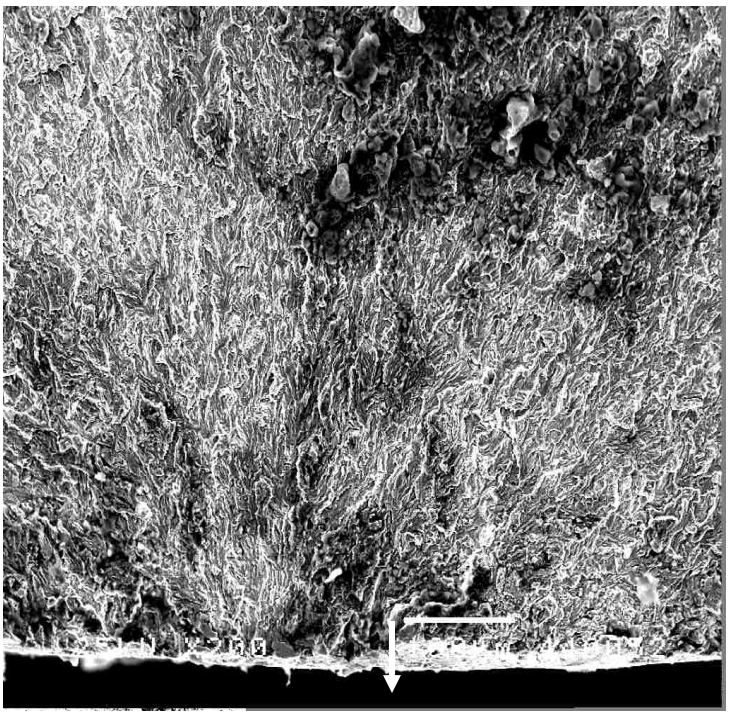

Figure 6.32: Fracture initiation site of area A in Figure 6.29 at 200X.

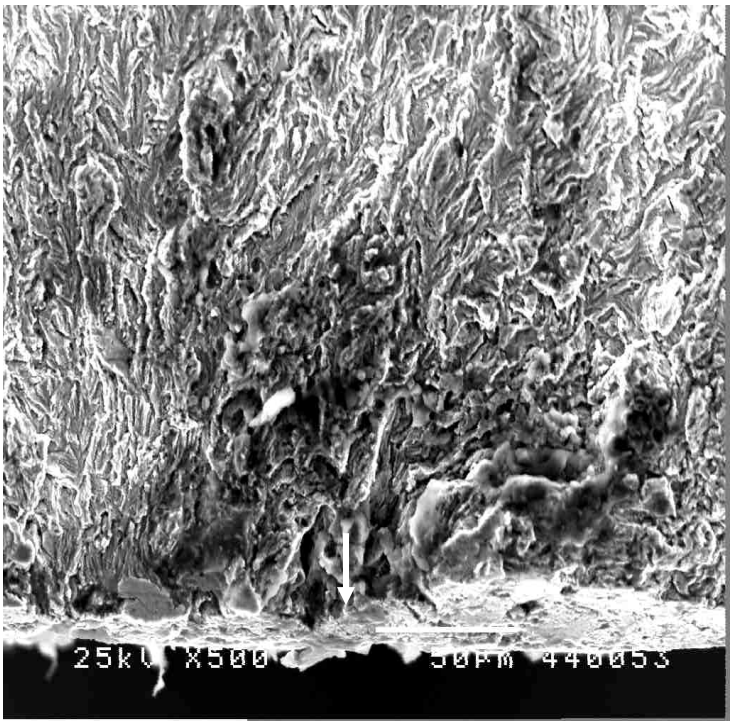

Figure 6.33: Fracture initiation site of area A in Figure 6.29 at 500X. The fracture started at a microscopic blister.

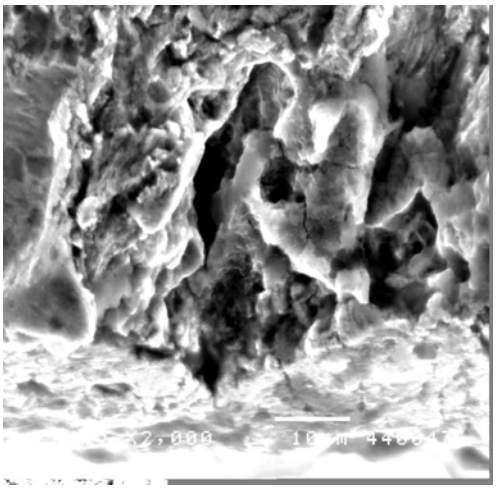

Figure 6.34: Microscopic blister at the initiation site of the fracture surface indicated in Figure 6.30, 2000X.

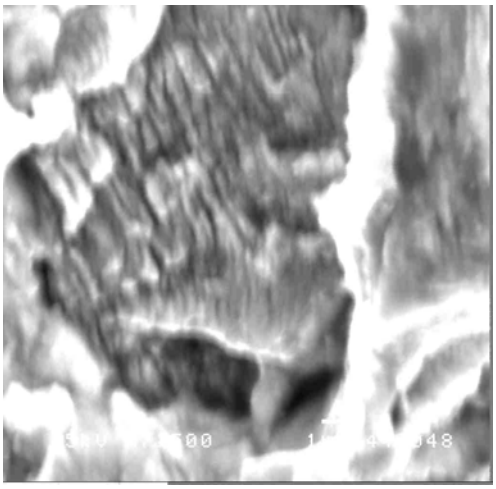

Figure 6.35: Fatigue striations at area A of Figure 6.29, 7500X.

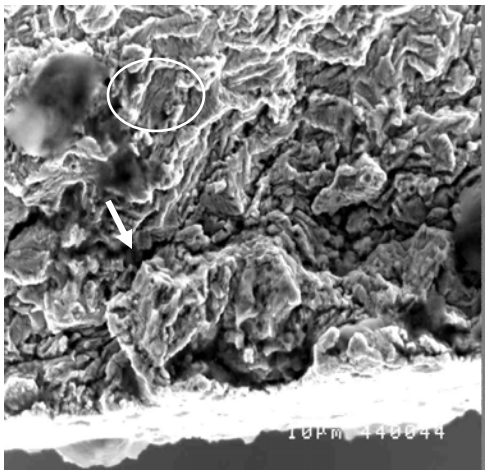

Figure 6.36: SEM photograph at the fracture initiation site of area A in Figure 6.30 showing a secondary crack, 1000X,

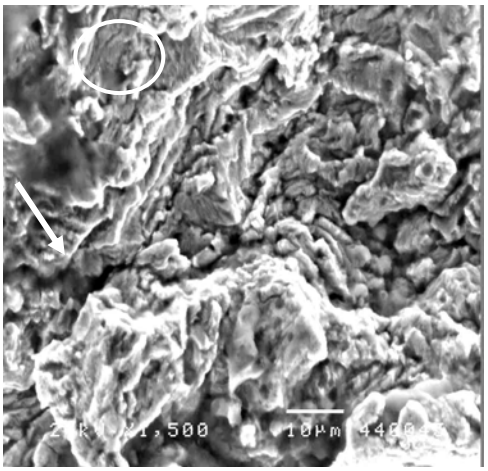

Figure 6.37: SEM photograph of the secondary crack indicated in Figure 6.36 at a higher magnification, 1500X. The arrow points to the secondary crack.

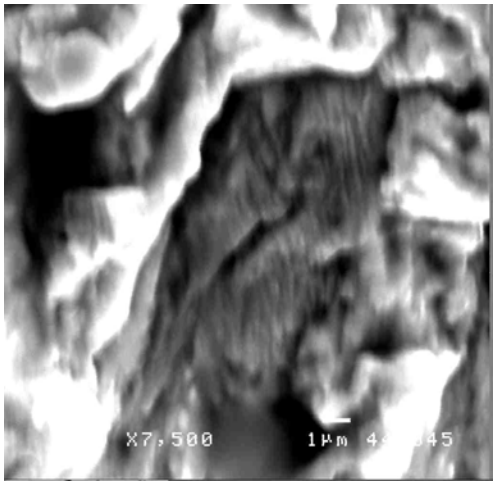

Figure 6.38: Fatigue striations were observed in the area encircled in Figure 6.36 near the secondary crack, 7500X.

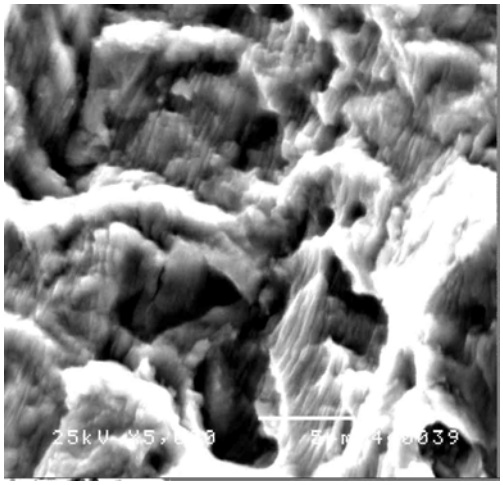

Figure 6.39: Fatigue striations at a magnification of 5000X.

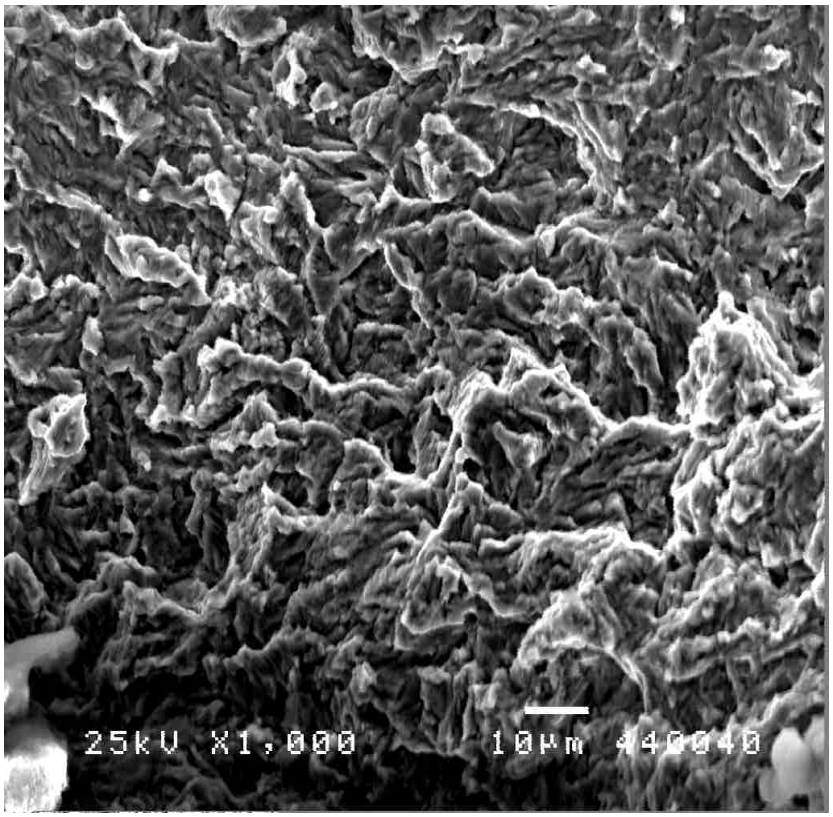

Figure 6.40: SEM photograph of area A in Figure 6.29 showing a brittle fracture with indications of quasi cleavage at 1000X.

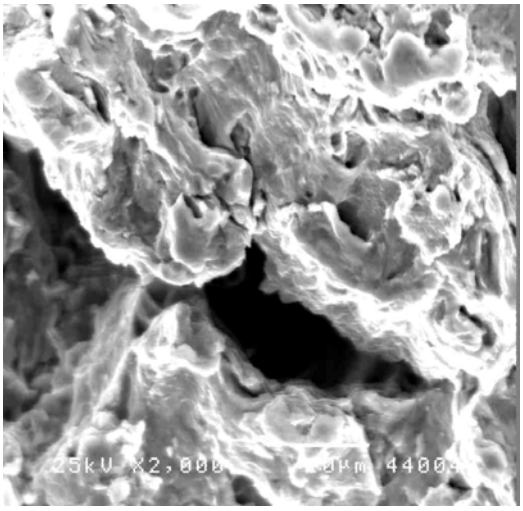

Figure 6.41: SEM photograph showing a blister between area B and C of Figure 6.29 at 2000X.

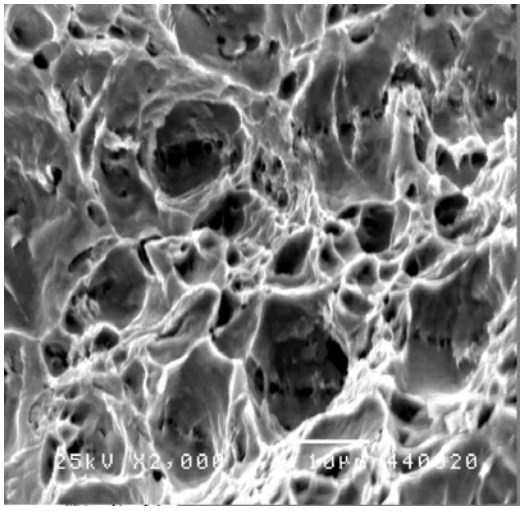

Figure 6.42: SEM photograph of area C Figure 6.29 showing a mix zone of brittle fracture and shear dimples at 2000X.

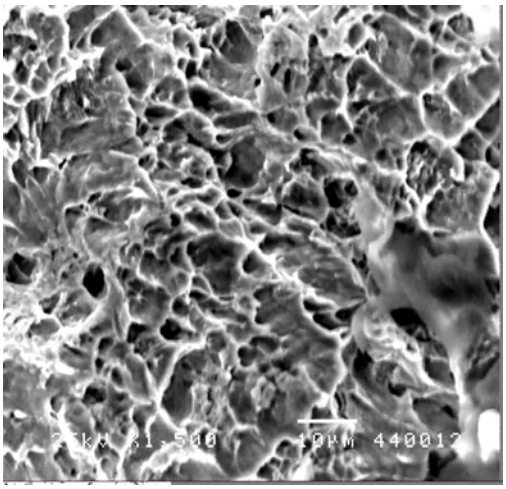

Figure 6.43: SEM photograph showing shear dimples in area D of Figure 6.29 at 1500X.

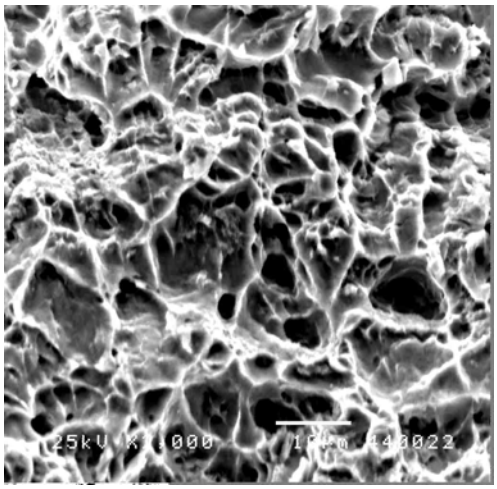

Figure 6.44: SEM photograph of area E in Figure 6.29 showing shear dimples at 2000X.

Figure 6.45: General SEM photograph of the fracture surface of sample A17, unexposed X-42 non-sour (L), at a magnification of 15X.

Figure 6.46: SEM photograph of the fracture initiation site of area A in figure 6.45 at 35X. The arrow points to the crack initiation site.

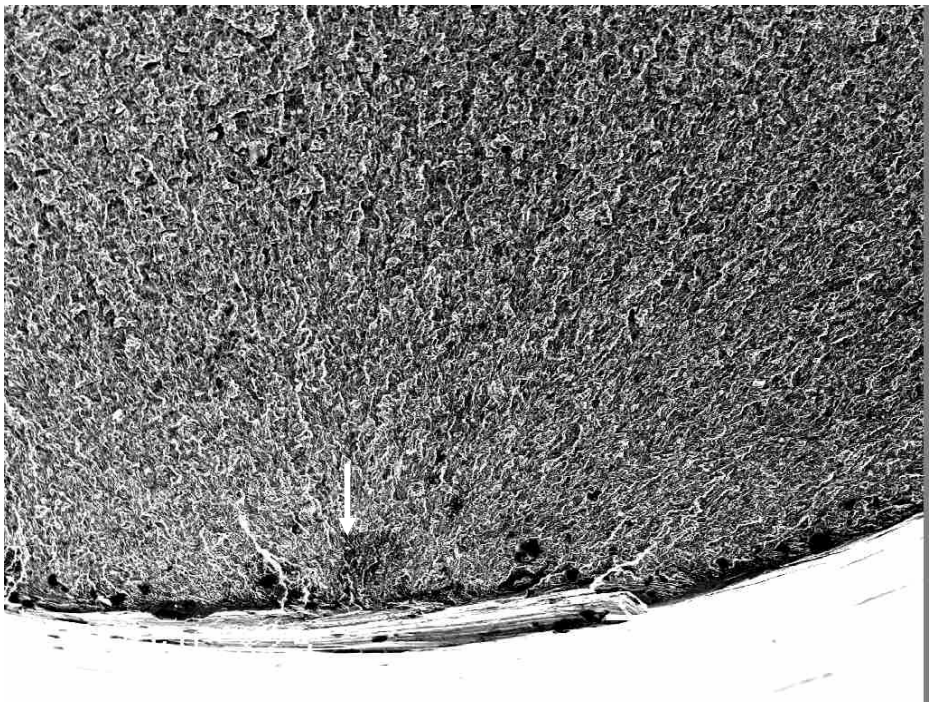

Figure 6.47: Fracture initiation site of area A in figure 6.45 at 75X. Radial lines converge to the crack origin.

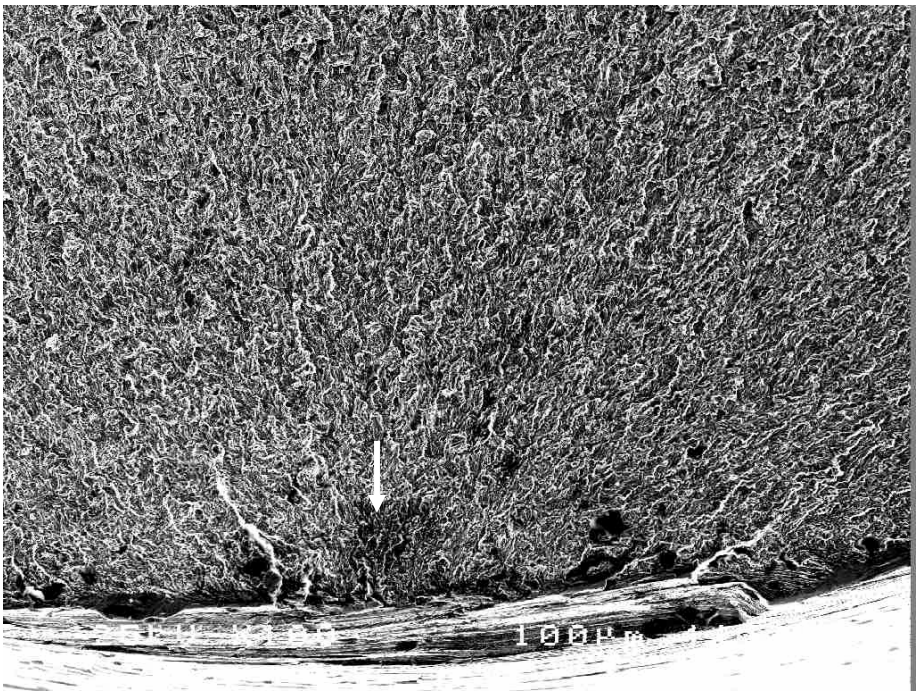

Figure 6.48: Fracture initiation site of area A in figure 6.45 at 100X. Radial lines converge to the crack origin.

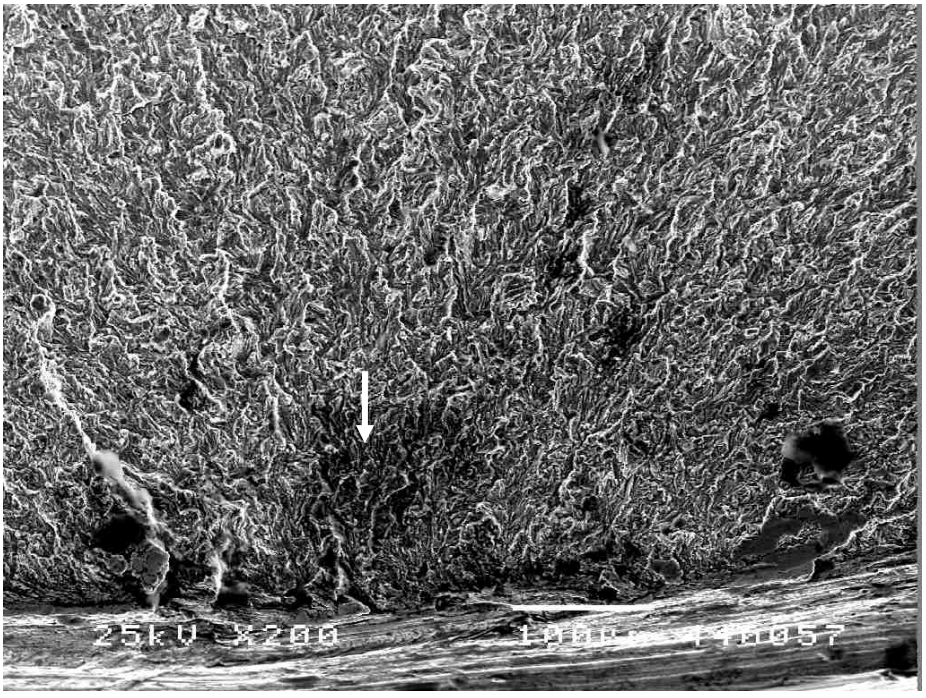

Figure 6.49: Fracture initiation site of area A in figure 6.45 at 200X.

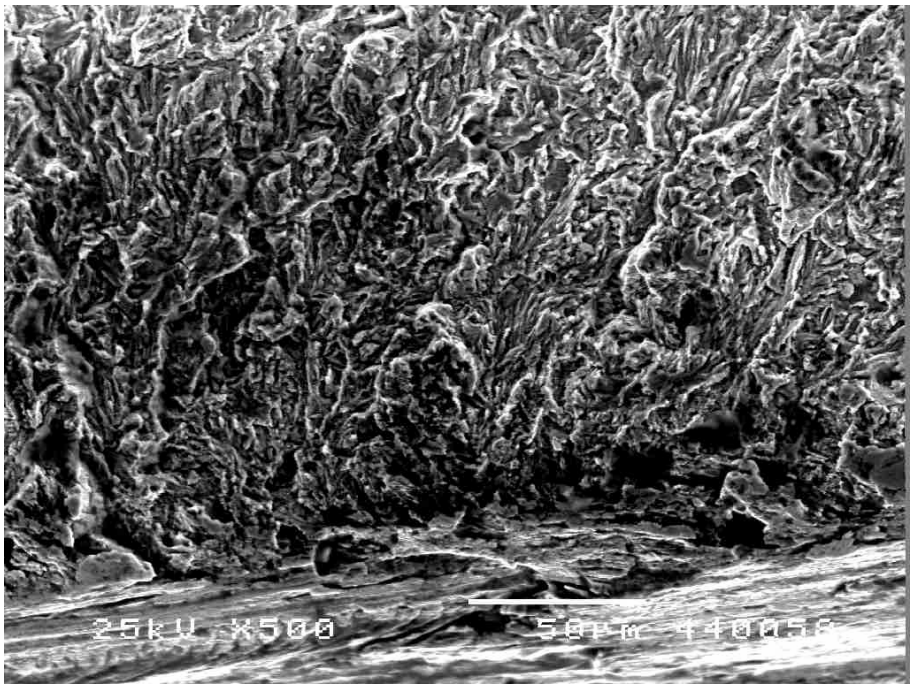

Figure 6.50: Fracture initiation site of area A in figure 6.45 at 500X.

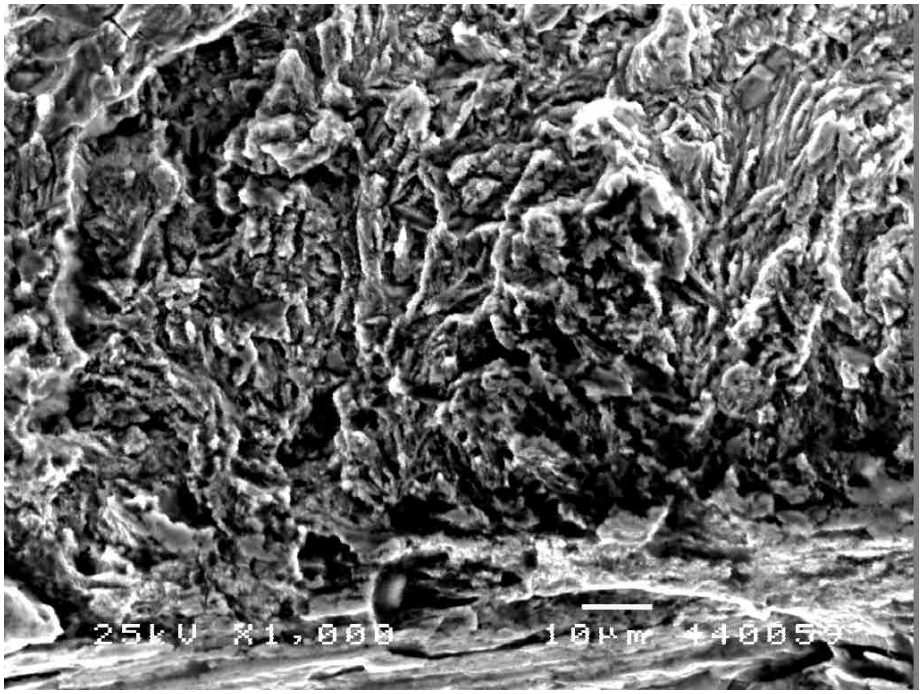

Figure 6.51: Fracture initiation site of area A in figure 6.45 showing a brittle fracture at 1000X.

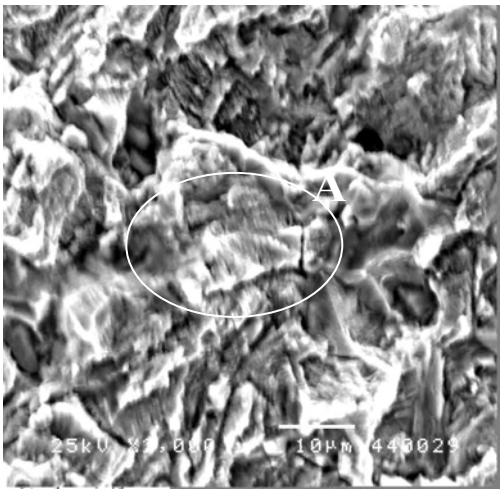

Figure 6.52: SEM photograph at area A in Figure 6.45, which shows a brittle fracture with indications of quasi cleavage at 2000X

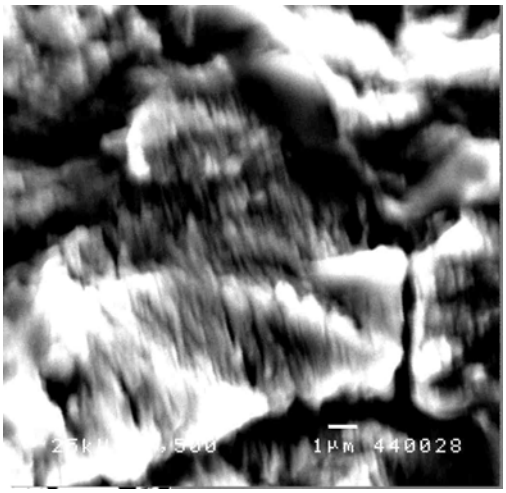

Figure 6.53: Zooming on area A of Figure 6.52 to show fatigue striations at 7500X.

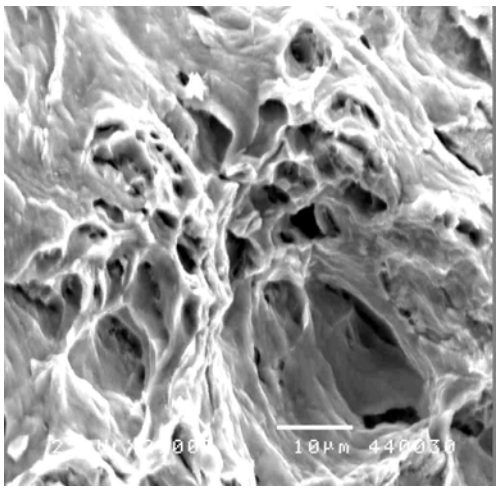

Figure 6.54: SEM photograph which shows the start of a mix zone of both a brittle fracture with shear dimples in area B of Figure 6.45 at 2000X

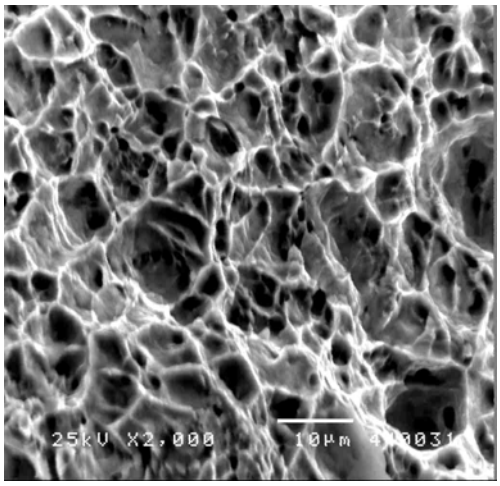

Figure 6.55: SEM photograph of area C in Figure 6.45 showing dimples due to overloading at a magnification of 2000X.

BIBLIOGRAPHY

1. C. Christensen and H. Arup, “Corrosion Monitoring in Wet Sour Gas By Use of Hydrogen Permeation Probes”, Corrosion, Paper Number 477, April 1989.

2. R. N. Iyer, I. Takeuchi, M. Zamanzadeh and H. Pickering, “Hydrogen Sulfide Effect on Hydrogen Entry into Iron – A Mechanistic Study”, Corrosion, June 1990.

3. J. M. Rigsbee, “The Role of Microstructure for Hydrogen-induced Blistering and Stepwise Cracking in a Plain Medium Carbon Steel”, Materials Science and Engineering, V74 n1, p 47-57, Sep. 1985.

4. A. Ikeda, T. Kaneko and F. Terasaki, “Influence of Environmental Conditions and Metallurgical Factors on HIC Initiation on Line Pipe Steel In the Wet H2S Environment”, Proceedings of Second JIM International Symposium (HYDROGEN IN METALS), P 609, Nov. 1979.

5. E. Miyoshi, T. Tanaka, F. Terasaki and A. Ikeda, “Hydrogen-Induced Cracking of Steels Under Wet Hydrogen Sulfide Environment”, Hydrogen Sulfide, 1976.

6. G. J. Biefer, “The Stepwise Cracking of Line-Pipe Steels in Sour Environments”, Materials Performance, June 1982.

7. R. D. Merrick, “An Overview of Hydrogen Damage to Steels at Low Temperatures”, Materials Selection & Design, February 1989.

8. H. Y. Liou, R. I. Shieh, F. I. Wei and S. C. Wang, “Roles of Microalloying Elements in Hydrogen Induced Cracking Resistant Property of HSLA Steels”, Corrosion, Vol 49, No 5, 1993.

9. R. K. Poepperling and I. G. Sussek, “Effect of Metallurgical and Testing Variables on Hydrogen-Induced Corrosion behaviour of Structural and Pipeline Steels, corrosion, 1995.

10. R. D. Merrick and M. L. Bullen, “Prevention of Cracking in Wet H_2S Environments”, Corrosion, Paper Number 269, April 1989.

11. Sumitomo Metal Industries Ltd, “Examination of Failed Gas Pipes”, June 1975.

12. S. M. Wihelm and D. Abayarathna, “Inhibition of Hydrogen Absorption by Steels in Wet Hydrogen Sulfide Refinery Environments”, Corrosion, Feb 1991.

13. M. Kimura, N. Totsuka, T. Kurisu, T. Hane and Y. Nakai, “Effect of Environmental Factors on Hydrogen Permeation in Line Pipe Steel”, Corrosion, 1988.

14. M. I. Luppo and J. O. Garcia, “The Influence of Microstructure on the Trapping and Diffusion of Hydrogen in A Low Carbon Steel”, Corrosion Scince, Vol 32, No 10, 1991.

15. R. R. Petrie and E. M. Moore Jr, “Determining the Suitability of Existing Pipelines and Producing Facilities for Wet Sour Service”, Materials Performance, June 1989.

16. P. F. Timmins, “Guidelines for Detecting Hydrogen Blisters and Similar Damage in Sour-Gas Service”, Oil & Gas Journal, Feb 1983.

17. J. F. Flavenot, “Prediction of the Fatigue Life of Mechanical Structures”, ASTM Special Technical Publication, n 1231, p 493 – 507, Dec 1994.

18. J. Solin and J. Hayrynen, “Simulation of Mechanical and Environmental Conditions in Fatigue Crack Growth Testing”, ASTM Special Technical Publication, n 1092, p 62-67, Nov 1990.

19. S. H. Ahn, F. V. Lawrence Jr and M. M. Metzger, “Corrosion Fatigue of an HSLA Steel”, Fatigue and Fracture of Engineering Materials & Structures, v 15, n 7, July 1992.

20. P. K. Mazumdar, “A Model For High Cycle Fatigue”, Engineering Fracture Mechanics, v 41, n 6, Apr 1992.

21. Y. N. Lenets, “Compression Fatigue Crack Growth Behavior of Metallic Alloys: Effect of Environment”, Engineering Fracture Mechanics, v 57, n 5, July 1997.

22. U. Gramberg, “Hydrogen Damage of Metallic Materials”, ASM, p 147 – 156, 1986.

23. E. R. Rios and A. Navarro, “Microstructural Fracture Mechanics in High-Cycle Fatigue”, Proceedings of High Cycle Fatigue of Structural Materials, p 157 – 166, 1997.

24. Y. C. Xiao, S. Li and Z. Gao, “A Continuum Damage Mechanics Model for High Cycle Fatigue”, International Journal of Fatigue, v 20, n 7, Aug 1998.

25. S. Wang, “Relationship Between the Fatigue Limit and the Mechanical Strength of Metals, Journal of Materials Processing Technology, V 100, n 1, p 42 – 46, 2000.

26. K. S. Rheem, “Effect of Residual Stress on Fatigue Crack Propagation”, American Society of Mechanical Engineers (Publication), v 304, p 73 – 79, 1995.

27. M. Gjonaj and M. Cukalla, “Mechanical Fatigue Behaviour of Chromium and Nickel Plain Carbon Steels”, Fixiko-Khimicheskaya Mekhanika Materialov, v 31, p 62 – 67, Feb 1995.

28. F. O. Riemelmoser and R. Pippan, Consideration of the Mechanical Behaviour of Small Fatigue Cracks, International Journal of Fracture, v 118, n 1-2, p 251 – 270, Dec 2002.

29. A. O. Soboyejo and W. O. Soboyejo, “Paris Law Extensions For Low (ΔK) and High (ΔK) Regimes and Applications in Reliability – Based Engineering Design Against Fatigue”, Proceedings of High Cycle Fatigue of Structural Materials, p 49 – 78, 1997.

30. B. E. Wilde, C. D. Kim and E. H. Phelps, “Some Observations on the Role of Inclusions in the Hydrogen Induced Blister Cracking of Linepipe Steels in Sulfide Environments”, National Association of Corrosion Engineers, vol. 36, No 11, November 1980.

31. H. Gao, X. Yang and E. R. De Los Rios, “Overload Effects in Environmental Hydrogen Induced Fracture”, Fatigue and Fracture of Engineering Materials and Structures, vol 19, no 5, pp. 629-623, 1996.

32. Y. Yoshino, “Metallurgical Influences on the Hydrogen Uptake by Steel in H_2S Environment”, Corrosion – NACE, November, 1982.

33. Bruno and Hill, “Stepwise Cracking of Pipeline Steels – A Review of the Work of Task Group T-1F-20”, Corrosion/80, Paper No. 6, NACE, March 1980.

34. T. Taira, Y. Kobayashi, K. Matsumoto and K. Tsukada, “Resistance of Line Pipe Steels to Wet Sour Gas”, Corrosion – NACE, vol 40, p 478-485, September 1984.

35. B. L. Jack, “Alternatives to HIC Resistant Steels in Sour Refinery Environments”, Corrosion – NACE, paper no 425, 1999.

36. R. H. Dauskardt, R. D. Pendse and R. O. Ritchie, “Effects of Pre-Existing Grain Boundary Microvoid Distributions on Fracture Toughness and Fatigue Crack Growth in Low Alloy Steel”, Acta Metallurgica, v 35, n 9, p 2227-2242, September 1987.

37. J. R. Vera, R. Case and A. Castro, “The relationship Between Hydrogen Permeation and Sulfide Stress Cracking Susceptibilty of OCTG Materials at Different Temperatures and PH Values”, Corrosion – NACE, 1997.
38. J. Heldt and H. Kaesche, “Effect of Absorbed Hydrogen on the Microstructure in the Vicinity of Near Threshold Fatigue Cracks in Low Alloy Steel”, ASTM Special Technical Publication, v 1296, p 338-351, April 1997.

VITA

- Rakan A. Al-Shammary

- Graduated from the University of Arizona in 1992, USA, with a BS degree in Materials Science and Engineering.

- Joined the Department of Mechanical Engineering at King Fahd University of Petroleum and Minerals (KFUPM), Dhahran, Saudi Arabia, as a part-time student.

- Working with Saudi Aramco as a materials engineer while doing the Master of Science (M.Sc.) program.

- Received the Master of Science (M.Sc.) degree in Mechanical Engineering from KFUPM, Saudi Arabia, in May 2005.